THESIS FOR THE DEGREE OF DOCTOR OF PHILOSOPHY

Waveguide Evanescent-Field Microscopy for Label-Free Monitoring of Biological Nanoparticles:

Fabrication, Characterization and Application

Mokhtar Mapar

Department of Physics

CHALMERS UNIVERSITY OF TECHNOLOGY

Göteborg, Sweden 2018

Waveguide Evanescent Field Microscopy for Label-Free Studies of Biological Nanoparticles: Fabrication, Characterization and Application

Mokhtar Mapar

ISBN: 978-91-7597-716-4

PhD dissertations at Chalmers University of Technology
New series No: 4397
ISSN 0346-718X

Department of Physics
Chalmers University of Technology
SE-412 96 Göteborg
Sweden
Telephone + 46 (0)31-772 1000

Cover illustration: The waveguide evanescent field microscopy device, capable of deliver images of biological nanoparticle in scattering and fluorescence.

Back cover: Bouldering on the Helmet! Photo by *Pontus Lindström*

Printed at Chalmers Reproservice
Göteborg, Sweden 2018

Waveguide Evanescent-Field Microscopy for Label-Free Monitoring of Biological Nanoparticles: Fabrication, Characterization and Application

Mokhtar Mapar
Department of Physics
Chalmers University of Technology

Abstract

The recent development of microscopy methods, biological assays and bioanalytical sensors has significantly advanced the understanding of biological systems. Surface-based bioanalytical sensors have in recent years gained increased interest thanks to improvements in sensitivity and simplicity to use. However, most of them, such as quartz crystal microbalance (QCM) and surface plasmon resonance (SPR), provide information based on ensemble averaging of biomolecular interactions. In contrast, with surface-sensitive microscopy methods, biological processes can be resolved down to the level of individual molecular interactions. Total internal reflection fluorescent microscopy is one commonly used surface-sensitive method, reaching sensitivities down to the level of single molecules, but it requires fluorescent labeling of at least one of the interaction partners and is often also hampered by photo bleaching processes.

In this thesis, we introduce a new wide-field surface-sensitive microscopy platform, based on a nanofabricated planar optical waveguide design that is capable of label-free evanescent-field microscopy of biological nanoparticles well below 100 nm in diameter. The waveguide generates an evanescent-field at the interface between the core of the waveguide and an aqueous solution, providing a thin sheet of illumination that offers imaging with low background disturbance. The device is presented in two designs, being compatible with either upright or inverted microscopes.

The work presented demonstrates how simultaneous monitoring of fluorescence and scattering signals can offer new information about the relation between scattering intensity, refractive index and lipid content of biological nanoparticles, such as exosomes. Further, the microfluidic design allowed not only for convenient liquid handling with dead volumes of a few microliter, it is also shown to aid label-free investigations of the interaction between proteins and individual lipid vesicles, with the latter serving as cell-membrane mimic. With the device also being compatible with formation of fluid supported lipid bilayers, preliminary results suggest that the design will open up a possibility to simultaneously determine the size, scattering intensity and fluorescence emission at the level of individual biological nanoparticles. With this realized, we foresee a broad applicability of the microscopy platform as multidimensional characterization tool for biological nanoparticles and beyond.

Keywords: Waveguide scattering microscopy, Waveguide fluorescence microscopy, surface-sensitive, Nanofabrication, Image processing, Label-free, Supported lipid bilayer, protein, Exosome

Appended publications

Paper I

Low-temperature fabrication and characterization of a symmetric hybrid organic-inorganic slab waveguide for evanescent light microscopy

Björn Agnarsson, Mokhtar Mapar, Mattias Sjöberg, Mohammadreza Alizadehheidari and Fredrik Höök*

Submitted

Paper II

Evanescent Light-Scattering Microscopy for Label-Free Interfacial Imaging: From Single Sub-100nm Vesicles to Live Cells

B. Agnarsson, A. Lundgren, A. Gunnarsson, M. Rabe, A. Kunze, M. Mapar, L.Simonsson, M. Bally, V. P. Zhdanov and F. Höök**

ACS Nano 9(12): 11849-11862.2

Paper III

Fabrication and Characterization of a Transparent Waveguide-Based Platform for Surface-Sensitive microscopy with microfluidic liquid handling

Mokhtar Mapar, Björn Agnarsson, Vladimir P. Zhdanov, Fredrik Höök*

In Manuscript

Paper IV

Effective refractive index and lipid content of extracellular vesicles revealed using optical waveguide scattering and fluorescence microscopy

*Déborah L. M. Rupert#, Mokhtar Mapar#, Ganesh Vilas Shelke, Karin Norling, Mathias Elmeskog, Jan O. Lötvall, Stephan Block, Marta Bally, Björn Agnarsson, Fredrik Höök**

Submitted **#**: Equal contribution

Paper V

Spatio-temporal kinetics of the formation of a lipid bilayer on silica via vesicle adsorption and rupture

*Mokhtar Mapar, Silver Jõemetsa, Hudson Pace, Vladimir Zhdanov, Björn Agnarsson and Fredrik Höök**

Submitted

Papers not included in the thesis

Paper VI

Plasmonic Nanopores in Metal-Insulator-Metal Films

A. B. Dahlin, M. Mapar, K. Xiong, F. Mazzotta, F. Höök, and T. Sannomiya*

Adv. Opt. Mater., vol. 2, no. 6, pp. 556–564, Jun. 2014

Paper VII

Extending charge separation lifetime and distance in patterned dye-sensitized SnO_2-TiO_2 µm-thin films

*V. Saavedra Becerril, E. Sundin, M. Mapar, and M. Abrahamsson**

Phys. Chem. Chem. Phys., vol. 19, no. 34, pp. 22684–22690, 2017

Contribution to the appended papers

Paper I: I was involved in the fabrication and experimental work involving the waveguide measurements. I was responsible for the image processing and participated in the analysis of the results. I contributed to the writing of the paper.

Paper II: I was involved in parts of the image processing and the data analysis.

Paper III: I was responsible for the development of the fabrication process, carried out the experiments, the image processing and the data analysis. I was extensively involved in the writing of the paper.

Paper IV: I was involved in designing the experiments, the image processing and the data analysis. I contributed to the writing of the final draft.

Paper V: I did the experimental work and developed the image processing and data analysis algorithms. I was extensively evolved in the writing process.

Table of Contents

Abbreviations

BNP	Biological nanoparticle
CTB	Cholera toxin B subunit
DRIE	Deep reactive ion etching
FNM	Flow nanometry
LSPR	Local Surface Plasmon Resonance
NA	Numerical aperture
NP	Nanoparticle
RIE	Reactive ion etching
SBR	Signal to background ratio
SNR	Signal to noise ratio
TIRF	Total internal reflection fluorescent microscopy
WGF	Waveguide Fluorescence
WGS	Waveguide Scattering

1 Introduction

Light has been a subject of fascination for humans form the beginning of human history. Light is considered sacred in several ancient religions; Ancient Egyptians' worshiped the sun[1] and Zoroastrians' regard fire as a symbol of purity.[2] They face a source of light to pray and believe the light of fire or sun to represent the divine light and wisdom. Still in many cultures light is used as a metaphor for truth or good. Early human interest to study light is therefore, not surprising.

Centuries of curiosity and research on light have led us to amazing discoveries. Understanding properties of light and its interaction with matter has brought about technologies that have, through optical communication systems, revolutionized our way of interacting, allowed us to harvest energy from the sun and to probe everything from the tiniest molecules to the far away planets. These discoveries and technologies are indeed owed to the diligence works of numerous scientist like Alhazen, Galileo Galilei, Lord Rayleigh, James Maxwell, Albert Einstein, and countless others who laid the foundations over the centuries for the discoveries of the past few decades.

The beauty of a blue sky can be mesmerizing to some but to those like Sir Isaac Newton it was the source of pondering. To study its peculiar nature, scientists in 19th century used alcohol and tobacco smokes to generating artificial skies,[3] but it wasn't until 1899 that Lord Rayleigh suggested that the light scattered from the atmospheric molecules is "suffice to give us a blue sky, not so very greatly darker than that actually enjoyed."[3] Nowadays some of the most popular and advanced nanoparticle size-determination techniques, such as dynamic light scattering (DLS)[4] and nanoparticle tracking analysis

(NTA),[5] characterize the suspensions of nanoscopic particles by analyzing the light scattered from these nanoparticles using the light-scattering and particle-diffusion theories first put forward by Gustav Mie[6] and Albert Einstein[7].

Optics, the science of light, has a long history and an important place in biological science. Soon after the invention of the first optical microscope in 1595,[8] it was used in studies of biological tissues and has since then been the cornerstone for many biological discoveries. Accordingly, a multitude of different configurations of optical microscopes have been developed to specifically address the needs in bioscience. The remarkable improvement in lateral resolution offered by some of these techniques brought yet another Nobel prize to the field of microscopy as recently as in 2014.[9–11]

Total internal reflection fluorescent (TIRF) microscopy is another important microscopy technique, developed for biological applications in the 1980s,[12] and has been extensively used to study single molecules[13] and various cellular phenomena,[14,15] to investigate interaction forces[16] and for obtaining sub-wavelength resolution.[17] Most TIRF microscopy setups employ high NA objectives to shine light at an angle larger than the critical angle for light to undergo total internal reflection at a glass-water interface. The total internal reflection of the light induces a non-radiative evanescent field at the water side that propagates along the surface and decays as it extends into the water. The result is a thin sheet of light illuminating only the very close vicinity of the interface. During or after immobilization of a sample of interest to the interface, one can continuously monitor changes in their fluorescence properties. This has enabled the use of TIRF in, for example, single particle and single molecule studies.[18–20]

By the turn of the 21th century yet another light-based invention, optical waveguides, revolutionized the information and telecommunication technology. However the use of optical waveguides has not been limited to the telecommunication field alone.[21–25] with waveguide concepts being frequently applied within the field of sensing and in particular, biosensing.[26–30] Most of these innovations take advantage of the evanescence-filed confined in the cladding of the waveguide to sense changes taking place in the vicinity of the light conducting layer.[21,26,28]

The present work is a summary of a few years of curiosity in a multidisciplinary field that involved the aforementioned optical technologies and concepts. We strived for developing a competitive label-free microscopy technique that could visualize, monitor, and characterize nanoparticles on a solid-water interface. To fulfill that goal we developed a proper nanofabrication procedure to make a special planar optical waveguide,[31] using a silicon oxide layer as a core and a water-refractive-index matching polymer as a cladding layer. To achieve a thin sheet of excitation light, similar to that of TIRF microscopy, [32–35] a sample-well was etched into the cladding to get access to the optical evanescence-field confined at the core-cladding interface. The nature of this illumination, and the low background provided by the fabrication quality, converted the device into a surface-sensitive microscopy platform that uses faint light scattered by

nanoparticles for sensing and imaging in either a label-free manner, or in combination with fluorescence imaging.

In this thesis, we demonstrate the compatibility of the waveguide evanescent-field microscopy concept with upright and inverted microscopes (**Papers I** and **III**) and present the fabrication procedure on two types of substrates, silicon and glass, without and with embedded microfluidic channels. Depending on the needs, experiments are conducted either by simple pipetting (**Paper I**) or using a more sophisticated and controlled laminar flow in micro-fluidic channels (**Paper III**). We also characterize the device in both fluorescent and scattering by assessing the image quality and the signal intensity of model scatterers and develop models for interpreting the intensity data.

We further demonstrate the capabilities of the platform to contribute insights of relevance in life science by performing microscopy on cell membrane model systems. We study the interactions of biomolecules with these model systems with the aim to quantify and relate the scattering intensities to relevant parameters characterizing the interaction (**Paper II** and **Paper III**). We also show that the combination of waveguide evanescent-field fluorescence and scattering microscopy can provide information about the refractive index of the biological nanoparticles, like extracellular vesicles (**Paper IV**); an information that can be valuable for future evaluation and characterization in this growing field of science.[36,37]

With the goal to benefit from the knowledge in our further endeavors with the waveguide, we examine the process of supported lipid bilayer (SLB) formation; a step required for many biological assays and experiments. Using TIRF microscopy we follow the growth of individual SLB patches, study their kinetics and speculate about the mechanism of bilayer formation (**Paper V**). The relevance of being able to from high quality SLBs on the waveguide surface is clear from the chapter of the thesis addressing additional results, where we present how the combination of the microfluidic capabilities of our device (**Paper III**) and our experience with bilayer formation (**Paper V**) come together in an experiment that is designed to determine the size of surface-bound nanoparticles.[38] Preliminary results using SLB tethered lipid vesicles indicate sufficient scattering intensity to enable label-free studies of $\sim 100\,\mathrm{nm}$ biological nanoparticles. By combing the size information for individual biological nanoparticles with their simultaneously acquired scattering and fluorescent intensities (**Paper IV**), other characteristic properties, such as the refractive index and molecular content, at the single particle level may not be out of reach.

2 Theoretical background

Thanks to the development of Information Technology, waveguide-based devices and sensors has been developed for primarily optical communication purposes. Depending on the particular application, these devices can come in different forms and configurations. The most common optical waveguide is an optical fiber, which has a circular cross section. In bioanalytical sensor applications, optical fibers are for example used for local illumination of sensor arrays[39]. When applied for microscopy applications, planar slab waveguides are preferred, since a large planar area becomes illuminated. A slab waveguide has a rectangular cross section, with finite dimension in one direction and (physically) infinite dimension in the other direction, which simplifies the theoretical description. In this chapter the physics of wave propagation in such a waveguide will be discussed.

2.1 Electromagnetic wave propagation

Light, as all other forms of electromagnetic radiations, can be described by two vector fields; electric field and magnetic field. The electric (**E**) and magnetic (**B**) fields are entangled fields and the relation between them is governed by the Maxwell equations:

$$\nabla \cdot \boldsymbol{D} = \rho \tag{2-1}$$

$$\nabla \cdot \boldsymbol{B} = 0 \tag{2-2}$$

$$\nabla \times \boldsymbol{E} = -\frac{\partial \boldsymbol{B}}{\partial t} \tag{2-3}$$

$$\nabla \times \boldsymbol{H} = \boldsymbol{J} + \frac{\partial \boldsymbol{D}}{\partial t} \tag{2-4}$$

Where ρ is the free charge density, **J** is electric current density. The electrical current density is related to the electrical field through the conductivity (σ) of the medium,

$$\boldsymbol{J} = \sigma \boldsymbol{E} \tag{2-5}$$

D and **H** are electric and magnetic displacement fields which are defined by:

$$\boldsymbol{D} = \varepsilon \boldsymbol{E} \tag{2-6}$$

$$\boldsymbol{H} = \frac{\boldsymbol{B}}{\mu} \tag{2-7}$$

where ε and μ are the permittivity and permeability of the medium which are related to those properties in vacuum by:

$$\varepsilon = \varepsilon_0 \, \varepsilon_r \tag{2-8}$$

$$\mu = \mu_0 \, \mu_r \tag{2-9}$$

ε_r and μ_r are called the relative permittivity and permeability of the medium.

For dielectrics and isolators, the absence of free charge entities in the material ($\rho = 0$) results in negligible conductivity, which in turn removes the electric current density from equation 2-4. For these materials the Eigen equation for wave propagation can be derived from Maxwell equations. Applying the curl ($\nabla \times$) operator to equation 2-3 results in,

$$\nabla \times \nabla \times \boldsymbol{E} = -\nabla \times \frac{\partial \boldsymbol{B}}{\partial t} \tag{2-10}$$

Using vector identity $\nabla \times \nabla \times \boldsymbol{E} = \nabla(\nabla \cdot \boldsymbol{E}) - (\nabla \cdot \nabla)\boldsymbol{E}$ and equation 2-1 on the left side and equation 2-4 on the right of the equation leads to Helmholtz equation.

$$\nabla^2 \boldsymbol{E} = \varepsilon \mu \frac{\partial^2 \boldsymbol{E}}{\partial t^2} \tag{2-11}$$

$$\nabla^2 \boldsymbol{E} - \frac{\varepsilon_r \mu_r}{c^2} \frac{\partial^2 \boldsymbol{E}}{\partial t^2} = 0 \tag{2-12}$$

Assuming a time harmonic monochromatic wave, where $\boldsymbol{E}(r,t) = \boldsymbol{E}(r)E(t)$ and $E(t) = e^{-i\omega t}$ one can further simplify the equation to

$$\nabla^2 \boldsymbol{E} + \varepsilon_r \mu_r \frac{\omega^2}{c^2} \boldsymbol{E} = 0 \tag{2-13}$$

The solution to this equation can be expressed in the form of a propagating plane wave:

$$\boldsymbol{E}(\boldsymbol{r}, t) = \boldsymbol{E}_0 e^{\pm i\boldsymbol{k}\cdot\boldsymbol{r} - i\omega t} \tag{2-14}$$

where ***k*** is the wave vector. The direction of the wave vector defines the direction of propagation and its magnitude, known as wavenumber, represents the spatial frequency of the wave, specifying how fast the wave front evolves in space along the wave vector. The wavenumber is defined by:

$$k = \sqrt{\varepsilon_r \mu_r} \frac{\omega}{c} \tag{2-15}$$

For most optical medium the relative permeability, μ_r, is close to unity and thus the wave number can be simplified to

$$k = n\, k_0 \tag{2-16}$$

where $n = \sqrt{\varepsilon_r}$ is the refractive index of the medium along the polarization vector, and $k_0 = \frac{\omega}{c}$ is the wavenumber in vacuum.

Similarly one can derive a similar formula for magnetic field displacement, H,

$$\nabla^2 \boldsymbol{H} = \varepsilon\mu \frac{\partial^2 \boldsymbol{H}}{\partial t^2} \tag{2-17}$$

$$\nabla^2 \boldsymbol{H} + \varepsilon_r \mu_r \frac{\omega^2}{c^2} \boldsymbol{H} = 0 \tag{2-18}$$

$$\boldsymbol{H}(\boldsymbol{r}, t) = \boldsymbol{H}_0\, e^{-i(\boldsymbol{k}\cdot\boldsymbol{r} - \omega t)} \tag{2-19}$$

2.2 Planar waveguide

A planar dielectric waveguide is a two dimensional guiding system that consists of three layers of material stacked on top of each other (Figure 2.1). The middle layer that is called core has a higher refractive index at the operating optical wavelength than the cladding layers surrounding it. If the cladding layers have the same refractive index ($n_2 = n_3$), the planar wave guide is called symmetric, otherwise, if not, asymmetric.

The propagation of light inside a waveguide is commonly described either with the help of Maxwell's equations or using geometrical ray optics. Here we start with describing the light behavior in the slab waveguide using ray optics. It helps the reader to develop an intuitive understanding of how the light propagates in the waveguide and how different modes are formed. However, to provide a better understanding of light

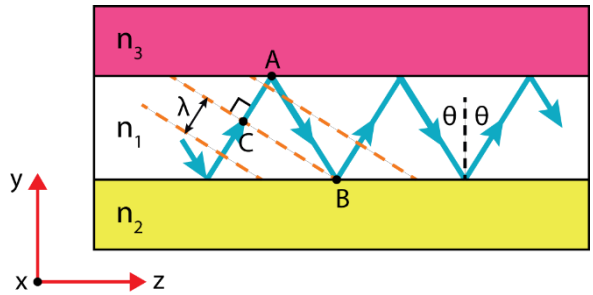

Figure 2.1. Side wide view of an asymmetric slab waveguide with a ray of light propagating through it. The oblique dashed lines represent the wave front around point C.

propagates through the waveguide the picture is complemented with the electromagnetic approach.

2.2.1 Ray Optics approach

Assume a beam of light in form of plane wave being focused to the core on the end-facet of a slab waveguide. If the angle of incident to the core-cladding interface is large enough, the light will undergo a total internal reflection and can potentially propagate through the waveguide in a zigzag fashion (Figure 2.1). In reality the excitation illumination is typically much wider than core, and therefore one can consider a plane-wave ray of light propagating through the waveguide. The ray is reflected at point A from the upper cladding and consequently at point B at the lower cladding. Although the angle of reflection is unchanged upon total internal reflection, a phase shift, $\varphi(\theta)$, is induced in the reflected light as the reflection coefficient turns into a complex value that depends on the angel of reflection, polarization of light and the refractive index of cladding and core. The constant phase plane of the reflected ray at B now overlaps with that of the first ray at point C. As these two rays share their phase planes if out of phase, they will interfere destructively and the wave will decay as it propagates forward. Therefore, for successful guiding, the parallel rays of light from consecutive reflections must be in phase. Mathematically this can be expressed as:

$$k_1(CA + AB) + 2\varphi(\theta) = 2m\pi \tag{2-20}$$

Where $k_1 = k_0 n_1 = \frac{2\pi n_1}{\lambda}$ is the wavenuber of the light propagating through the core, and *m* has an integer value. The length of the CA and AB paths can be expressed by

$$CA = cos(2\theta)\, AB\,, AB = \frac{d}{cos(\theta)} \tag{2-21}$$

$$CA + AB = (cos(2\theta) + 1)\frac{d}{cos(\theta)} = (2\,cos^2(\theta))\frac{d}{cos(\theta)} = 2d\ cos(\theta) \qquad (2\text{-}22)$$

Plugging this into eq. 2-20 results in:

$$k_1(2d\,cos(\theta)) + 2\varphi(\theta) = 2m\pi \qquad (2\text{-}23)$$

Equation 2-23 places a constrain on the incident angle of the guided rays. For each m there will be one allowed incident angle of θ_m corresponding to a unique propagation mode and its corresponding $\varphi(\theta_m)$ or φ_m for which the light can propagate through the waveguide as long as $\theta_m > \theta_c$ where θ_c is the critical angle for total internal reflection. Each θ_m corresponds to a single *propagation mode* θ_m, and θ_0, corresponding to the largest angle of incident, is generally referred to as the ground or fundamental mode of the waveguide. The phase shift φ_m can be understood as the penetration of the zig-zag ray (for a certain depth δ) into the cladding layers before being reflected.

The propagation constant along the waveguide for each mode can be resolved by projecting the wavevector along the guiding direction,

$$\beta_m = k_1\,sin(\theta_m) = k_0 n_{eff} \qquad (2\text{-}24)$$

Considering the total internal reflection condition, $\theta_c < \theta_m < 90$, one can identify the β_m limits compared to the wavenumber in core and cladding,

$$k_0 n_1\,sin(\theta_c) < k_0 n_1\,sin(\theta_m) < k_0 n_1\,sin(90) \qquad (2\text{-}25)$$

$$k_0 n_2 < \beta_m < k_0 n_1 \qquad (2\text{-}26)$$

$\varphi(\theta_m)$ can further be calculated using appropriate boundary conditions,[40,41] and hence, for a given *m* and a set of parameters n_1, n_2, and *d*, a discrete set of reflection angles θ_m can be obtained using equation 2-23 , each corresponding to a unique mode.

2.2.2 Electromagnetics approach

Now we complement the ray optics with an electromagnetic analysis to give the reader a better view of light propagation in a planar waveguide.

The light that travels in the waveguide in TE mode, having its electric field vector perpendicular to the plan of propagation, is still governed by Maxwell's equations, and thus equation 2-13 holds. The light travels along the waveguide in z direction with a wavenumber of β_m, and one can separate the z dependence of the light in the form of a complex exponential coefficient. As the waveguide is semi-infinite in the x direction, the solution to the electric field is not a function of x. Therefore,

$$\boldsymbol{E}_x = \boldsymbol{E}_x(y,z) = \boldsymbol{E}_x(y)e^{i\beta_m z} \qquad (2\text{-}27)$$

By substituting 2-27 in equation 2-13 we have

$$\nabla_y^2 \boldsymbol{E_x} - \beta_m^2 \, \boldsymbol{E_x} + k^2 \, \boldsymbol{E_x} = \boldsymbol{0} \tag{2-28}$$

$$\frac{\partial^2}{\partial y^2} \boldsymbol{E_x} + (k^2 - \beta_m^2) \boldsymbol{E_x} = \boldsymbol{0} \tag{2-29}$$

where k is the wavenumber for free propagation of light in the medium, which depends on the refractive index. This in turn means that the $(k^2 - \beta_m^2)$ coefficient adopts different values for the core and the cladding. The latter expression is positive for the core and negative for the cladding in the guiding mode according to equation 2-26, and results in an evanescent field in the cladding and a sinusoidal wave profile in the core along the y axis. The wave equations in the upper cladding, core and lower cladding will be as followed

$$\boldsymbol{E_x} = A \, e^{-\sqrt{(\beta_m^2 - k_{clad}^2)}\, y} e^{i\beta_m z} \tag{2-30}$$

$$\boldsymbol{E_x} = (B \, cos(\sqrt{(k_{core}^2 - \beta_m^2)}\, y) + C \, sin(\sqrt{(k_{core}^2 - \beta_m^2)}\, y)\,) e^{i\beta_m z} \tag{2-31}$$

$$\boldsymbol{E_x} = D \, e^{\sqrt{(\beta_m^2 - k_{clad}^2)}\, y} e^{i\beta_m z} \tag{2-32}$$

$$D \, e^{\sqrt{(\beta_m^2 - k_{clad}^2)}\, y} e^{i\beta_m z}$$

At higher modes, as β_m^2 decrease due to smaller angle of incident, the $(k_{core}^2 - \beta_m^2)$ and $(\beta_m^2 - k_{clad}^2)$ respectively increase and decrease, respectively. This results in smaller decay length in the cladding and more oscillations in the core. According to Equations 2-30 and 2-32, the electromagnetic wave created in the cladding, propagates in the *z* direction with an intensity that decays with distance from the core layer. This decaying behavior can be characterized by a decay length, *d*, known as penetration depth, defined by the distance at which the intensity of the electric field has dropped to $1/e$ of the value at the interface,

$$d = \frac{1}{\sqrt{(\beta_m^2 - k_{clad}^2)}} = \frac{\lambda_0}{2\pi} \frac{1}{\sqrt{n_{eff}^2 - n_{cladding}^2}} \tag{2-33}$$

This will produce a sheet of light in close vicinity of the core layer in the cladding only.

In microscopy application and especially in fluorescence microscopy we deal with light intensity rather than the intensity of the electric field. Since the intensity of the light is defined by the time average magnitude of the Poynting vector,

$$I = \langle \boldsymbol{S} \rangle = \langle \boldsymbol{E} \times \boldsymbol{H} \rangle = \frac{\varepsilon c}{2} |E|^2 \tag{2-34}$$

Then light intensity in the cladding can be represented as

$$I = I_0 \, e^{-\frac{y}{\delta}} \tag{2-35}$$

Where δ is the penetration depth for the light intensity,

$$\delta = \frac{d}{2} = \frac{\lambda_0}{4\pi} \frac{1}{\sqrt{n_{eff}^2 - n_{cladding}^2}} \tag{2-36}$$

Measuring the penetration depth of waveguides is not a trivial task. A few methods can be found in literatures to measure the penetration depths of similar system, [42–44] which show rather good agreement between theory and experiment. Here we rely on the theoretical prediction of the penetration.

2.3 Scattering

The label-free attribute of our waveguide microscopy device is owed to the scattered light by object that are a few tens of nanometers. As the objects get larger, they scatter more which make them easier to observer, however, the complexity of the physics describing the scattering also increase with the intensity of the scattered light.

The following section will give a brief overview of some of the most essential concepts and models used to describe light scattering of nanoparticles. It starts with the dipole scattering, describing the scattering of a small molecule to build the foundation for the Rayleigh approximation well suited for small dielectric object, such as sub 100 nm polystyrene beads (**Paper III**). However, since many biological nanoparticles, like extracellular vesicles, can be larger than 100 nm, a more accurate approximation namely Rayleigh-Gans-Debye (RGD), is applicable. In **Paper III** and **IV** RGD based models are used to describe the scattering from surface adsorbed particles; which allows us to estimate the refractive index of exosomes and the surface concentration of bound protein-layers to a lipid vesicles. Although not much used in this work, and more as natural progression of the discussion connected to the models used, the chapter finishes with a short description of the rigorous *Mie solution*, which gives the most accurate description of the scattering of spheres of arbitrary size.

2.3.1 Dipole approximation

Figure 2.2A illustrates a dipole locate at origin of the coordinate system, with charges $\pm q$ separated by a distance d along *z* axis, harmonically oscillating at a frequency $\omega =$

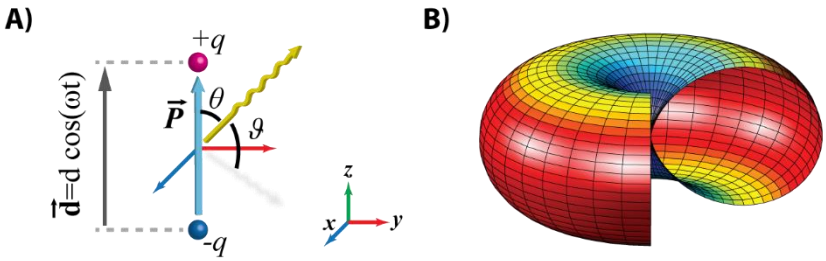

Figure 2.2. A) A dipole consisting of two opposite charges $\pm q$ separated by a distance d along z axis, harmonically oscillating at a frequency ω symmetrically around the origin. B) Dipole radiation pattern in scape for a dipole described in figure (A). One quarter of the radiation patter has been cut away to show the radiation cross-section. The intensity of the radiation is both described with the rainbow color and the distance from the dipole assumingly positioned in the center of the radiation pattern.

c/λ, where $\lambda = \frac{\lambda_0}{\sqrt{\varepsilon_m}}$ and $c = \frac{c_0}{\sqrt{\varepsilon_m}}$ are the wavelength and speed of light in the surrounding medium that has a permittivity $\varepsilon = \varepsilon_m \varepsilon_0$. The dipole moment of such a dipole is defined as

$$\vec{\boldsymbol{p}} = q\vec{\boldsymbol{d}} = q_0 d\, cos(\omega t)\, \hat{\boldsymbol{z}} = p_0\, cos(\omega t)\, \hat{\boldsymbol{z}} \tag{2-37}$$

where $p_0 = |\vec{\boldsymbol{p}}| = q_0 d$ is magnitude of dipole momentum oscillation. The radiated electric field by this oscillating dipole, at a wavelength much larger than the charge separation, and at a distance much longer than the wavelength, cab be estimated to[45]

$$\vec{\boldsymbol{E}} = -\frac{\pi p_0}{r\varepsilon\lambda^2} sin\,\theta\, cos(\omega t - kr)\, \widehat{\boldsymbol{\theta}} \qquad (r \gg \lambda \gg d) \tag{2-38}$$

For an electromagnetic wave, Poynting vector, $\vec{\mathbf{S}}$, defines the direction and amplitude of the energy flux in a field, and its time average is what we measure as intensity,

$$\vec{\boldsymbol{S}} = \vec{\boldsymbol{E}} \times \vec{\boldsymbol{H}} \quad and \quad \langle \vec{S} \rangle = \frac{\varepsilon c}{2} \left|\vec{\boldsymbol{E}}\right|^2 \tag{2-39}$$

and the radiated energy away from our dipole

$$\vec{\boldsymbol{I}}_{\boldsymbol{s}} = \frac{\pi^2 p_0^2 c}{2\varepsilon\lambda^4} \left(\frac{sin\,\theta}{r}\right)^2 \hat{\boldsymbol{r}} \tag{2-40}$$

For an polarizable atom with spherical symmetry in an electric field, the field will causes a charge separation and induces a dipole moment that is proportional to the magnitude of and aligned with the field,

$$\vec{\boldsymbol{p}} = \alpha\vec{\boldsymbol{E}} = \alpha E_0 \widehat{\boldsymbol{E}} \tag{2-41}$$

This proportionality constant, α, is knowns as polarizability, and allows us to express the intensity of radiated light by the induced dipole based on the incident light,[46]

$$p_0^2 = \alpha^2 {E_0}^2 \quad and \quad I_0 = \frac{\varepsilon c}{2}\left|\vec{\boldsymbol{E}}\right|^2 \tag{2-42}$$

$$\vec{\boldsymbol{I}}_{\boldsymbol{s}} = \frac{\pi^2\alpha^2\left|\vec{\boldsymbol{E}}\right|^2 c}{2\varepsilon\lambda^4}\left(\frac{sin\,\theta}{r}\right)^2 \hat{\boldsymbol{r}} = \frac{\pi^2\alpha^2}{\varepsilon^2\lambda^4}\left(\frac{sin\,\theta}{r}\right)^2 I_i\,\hat{\boldsymbol{r}} \tag{2-43}$$

This phenomenon that has resulted in the redistribution of the energy that has acted on the polarizable atom, is called scattering.

When the scattered light is collected by a sensing element, the recorded intensity is proportional to the intensity of the scattered light which is directed toward the sensing element in specific spatial angular limits, i.e. solid angle. Therefore it is useful to introduce a *differential scattering cross-section* based on the solid angle,[47]

$$I_s = \frac{\partial\sigma_s}{\partial\Omega}\frac{1}{r^2}I_i \quad where \quad \frac{\partial\sigma_s}{\partial\Omega} = \frac{\pi^2\alpha^2}{\varepsilon^2\lambda^4}sin^2\,\theta \tag{2-44}$$

Figure 2.2B presents the angular dependency of the dipole radiation in the space, which is known as the radiation pattern. In such illustrations the direction and length of the vector connecting the origin, where the dipole is located, to any point on the surface represents the direction and relative magnitude of radiation from the dipole. The total scattered light intensity, P, is calculated by integrating the scattered light intensity over all solid angles, i.e. on the surface of a sphere enclosing the dipole,

$$P = \frac{8\pi^3\alpha^2}{3\varepsilon^2\lambda^4}I_i = \frac{k^4\alpha^2}{6\pi\varepsilon^2}I_i = \sigma_s I_i \tag{2-45}$$

where σ_s is referred to as scattering cross-section. For a material with a measured relative permittivity of ε_s and volume V, consisting of n polarizable molecules in a background medium with permittivity of $\varepsilon = \varepsilon_0\varepsilon_m$, the polarizability of each unite volume $dv = V/n$, consisting of one polarizable molecule in the volume dv of the medium can be calculated using *Clausius-Mossotti* equation[48]

$$\alpha = 3dv\,\varepsilon\frac{\varepsilon_s - \varepsilon_m}{\varepsilon_s + 2\varepsilon_m} \tag{2-46}$$

2.3.2 Rayleigh scattering

In the Rayleigh regime, the particle with longest dimension a, is assumed to be very small compared to the wavelength, $a \ll \lambda$, so that the phase of the incident wave does not change significantly over the particle size scale, $ka \ll 1$, where $k = \frac{2\pi}{\lambda}$ is the propagation constant, also known as the phase factor, and the product, $\mathrm{x} = \mathrm{ka}$*, is*

referred to as size factor. Under this condition, the particle experiences a uniform field inside that is changing with time, which means the induced dipoles in the particle are in phase. In this case, the particle can be modeled with a diploe with a polarizability proportional to its volume, V,[49]

$$\alpha = 3V\varepsilon\frac{\varepsilon_s - \varepsilon_m}{\varepsilon_s + 2\varepsilon_m} \tag{2-47}$$

where ε_s *and* ε_m *are the relative permittivity of the medium and scatterer and* $\varepsilon = \varepsilon_m\varepsilon_0$ is the permittivity of the medium. Following the dipole approximation, the differential scattering cross-section of a sphere with diameter a, assuming the material is polarized along the filed, can be expressed as

$$\frac{\partial\sigma_s}{\partial\Omega} = \frac{\pi^2}{\lambda^4}9V^2\left(\frac{\varepsilon_s - \varepsilon_m}{\varepsilon_s + 2\varepsilon_m}\right)^2 sin^2\,\theta = \frac{16\pi^4}{\lambda^4}a^6\left(\frac{\varepsilon_s - \varepsilon_m}{\varepsilon_s + 2\varepsilon_m}\right)^2 sin^2\,\theta \tag{2-48}$$

$$\frac{\partial\sigma_s}{\partial\Omega} = k^4a^6\left(\frac{\varepsilon_s - \varepsilon_m}{\varepsilon_s + 2\varepsilon_m}\right)^2 sin^2\,\theta \tag{2-49}$$

and the scattering cross section of such a particle is:

$$\sigma_s = \frac{8\pi}{3}k^4a^6\left(\frac{\varepsilon_s - \varepsilon_m}{\varepsilon_s + 2\varepsilon_m}\right)^2 \tag{2-50}$$

For some application it is more convenient to evaluate the scattering based on the scattered angle relative to the direction of incident light in the plane of incidence, $\vartheta = \theta - \frac{\pi}{2}$, rather than the angle relative to the dipole vector. In that case,

$$\frac{\partial\sigma_s}{\partial\Omega} = k^4a^6\left(\frac{\varepsilon_s - \varepsilon_m}{\varepsilon_s + 2\varepsilon_m}\right)^2 cos^2\,\vartheta \tag{2-51}$$

2.3.3 Rayleigh-Gans-Debye approximation

Rayleigh-Gans-Debye (RGD) approximation[50] can be considered as an extension to Rayleigh scattering, which is valid for optically soft particles, i.e. particles with refractive index close to the medium. In contrast to Rayleigh scattering where the whole particle is represented as a single dipole, every infinitely small volume element, dv, of an arbitrary shaped scatterer is instead considered to acts as a dipole. Similar to Rayleigh scattering, these independently oscillating dipoles experience the incident field with similar phase and intensity as it is in the environment as if the particle was not there, and their emitted light is not disturbed at the boundary of the particle to medium. But what makes RGD approximation significantly more accurate than Rayleigh approximation for large scatters, is that it account for the relative phase retardation that occur due to the particles size in the scattering process. For large scatterers due to the spatial arrangement of the volume elements, the corresponding induced dipoles not

only oscillate with different phase relative to each other, but also their radiation experience different phase retardations on their path to the observer. This results in interference patterns in the scattered light that can be predicted using RGD approximation but does not exist in Rayleigh approximation.[51]

For a scattering with relative refractive index of $m = n_s/n_m$ and a size factor of $\mathrm{x} = \mathrm{ka}$, where a is the largest dimension of the scatterer and k *is the propagation constant in the medium*, the earlier mentioned conditions for the RGD approximation can summarized as

- The incident field should not be disturbed much by the particle, $|m-1| \ll 1$,
- The phase difference in the particle relative to the medium should be negligible, $x|m-1| \ll 1$.

Following the Rayleigh notation in the previous section, under these assumptions, for a plane wave polarized along z axis, propagating along x axis, the magnitude of the induced dipole moment for an arbitrary volume element, dv, with polarizability of α_v is

$$p_0 = \alpha_v E_0 e^{j\delta_i} = 3dv\, \varepsilon \frac{\varepsilon_s - \varepsilon_m}{\varepsilon_s + 2\varepsilon_m} E_0 e^{j\delta_i} \tag{2-52}$$

where δ_i is the phase retardation of the incident electric field due to the spatial position of the element relative to the reference point, say origin. Further, the emitted electric field by the induced dipole, $d\vec{\mathbf{E}}$, experiences an additional phase retardation, δ_e, on its path to the observer, relative to an in-phase radiation from the origin,

$$d\vec{\boldsymbol{E}} = -\frac{\pi p_0}{r\varepsilon\lambda^2} e^{j\delta_e} \sin\theta \cos(\omega t - kr)\, \hat{\boldsymbol{\theta}} \tag{2-53}$$

By substituting the dipole moment from equation 2-52 in equation 2-53, the electric field of the induced dipole can be expressed as

$$d\vec{\boldsymbol{E}} = -\frac{\pi}{r\lambda^2} 3 \frac{\varepsilon_s - \varepsilon_m}{\varepsilon_s + 2\varepsilon_m} \sin\theta\, e^{j\delta} dv E_0 \cos(\omega t - kr)\, \hat{\boldsymbol{\theta}} \tag{2-54}$$

where $\delta = \delta_i + \delta_e$ is the total retardation relative to the origin. The scattered electric field at a specific point in space can be calculated by integrating the effect of all volume elements,

$$\vec{\boldsymbol{E}} = -\frac{3\pi}{r\lambda^2} \frac{\varepsilon_s - \varepsilon_m}{\varepsilon_s + 2\varepsilon_m} \sin\theta\, E_0 \cos(\omega t - kr) \iiint_V e^{j\delta} dv\, \hat{\boldsymbol{\theta}} \tag{2-55}$$

$$\vec{\boldsymbol{E}} = -\frac{\pi\alpha}{r\varepsilon\lambda^2} \sin\theta\, E_0 \cos(\omega t - kr)\, P(\theta, \varphi)\hat{\boldsymbol{\theta}} \tag{2-56}$$

And the scattering light intensity and the differential scattering cross section are,

$$\vec{\boldsymbol{I}} = \frac{\pi^2\alpha^2}{r^2\varepsilon^2\lambda^4} sin\,\theta\,|P(\theta,\varphi)|^2 I_i \hat{\boldsymbol{r}} \tag{2-57}$$

$$\frac{\partial\sigma_s}{\partial\Omega} = \frac{\pi^2\alpha^2}{\varepsilon^2\lambda^4} sin^2\,\theta\,|P(\theta,\varphi)|^2 \tag{2-58}$$

where $\alpha = V\alpha_v$ is the polarizability of the whole particle and

$$P(\theta,\varphi) = \frac{1}{V}\iiint_V e^{j\delta}dv \tag{2-59}$$

is the shape factor, governing the angular dependency of the relative intensity of scattered light in the space. The shape factor for a sphere located in the origin is,[52]

$$P(\theta,\varphi) = G(u) = \frac{3}{u^3}(sin\,u - u\,cos\,u) = \left(\frac{9\pi}{2u^3}\right)^{\frac{1}{2}} J_{\frac{3}{2}}(u) \qquad ,u = 2x\,sin\left(\frac{\vartheta}{2}\right) \tag{2-60}$$

where $\vartheta = \frac{\pi}{2} - \theta$ is the scattering angle relative to the incident direction, rather than the dipole moment, and $J_{\frac{3}{2}}(u)$ is the three-half order Bessel function.

Similarly, for a core-shell spherical particle with core and shell radius of r_c and r_s, and corresponding relative refractive index of m_c and m_s, the form factor can be express,[52]

$$P(\theta,\varphi) = \frac{1}{(V_s - V_c)}\left(V_s G(u) - \frac{m_c - m_s}{m_s - 1} V_c G(v)\right) \tag{2-61}$$

where $u = 2kr_s \sin\left(\frac{\vartheta}{2}\right)$, $v = 2kr_c \sin\left(\frac{\vartheta}{2}\right)$, and V_s and V_c are the volume of spheres with radius corresponding to that of the shell and the core. For a hollow shell, this can be simplified to,[53]

$$P(\theta,\varphi) = \frac{3}{u^3 - v^3}\big(sin\,u - sin\,v - (u\,cos\,u - v\,cos\,v)\big) \tag{2-62}$$

In such cases, when calculating the differential scattering cross-section of the particle one needs to use polarizability of the whole particle. For core-shell structures with radial symmetry this can be

$$\alpha = \iiint_V \alpha'(r,\theta,\varphi)dv = \int_0^{r_s} 4\pi r^2 \alpha'(r)dr \tag{2-63}$$

where α', is the polarizability distribution function per unit volume.

2.3.4 Mie regime

For a spherical particle, the exact scattering of electromagnetic can be analytically solved. This approach, known as Mie solution[6], provides the exact analytical expression for the scattering of plane wave by a spherical object with a uniform polarizability, unlike the Rayleigh and Rayleigh-Gans-Debye theories that enforce restrictions on size and/or optical contrast of the scatterer, relative to the incident wavelength and the surrounding medium. This is not achieved without a cost; the Mie solution needs to be evaluated numerically.

The mathematical derivation of Mie scattering is rather cumbersome but an enjoyable presentation of it can be found in reference 54. In short, the problem is approached in spherical coordinates by deriving the general solution of freely propagating wave in the this coordinate system and expressing an incident polarized plane wave with amplitude E_0 in term of infinite series of vector spherical harmonics. The fields inside and scattered by an arbitrary sphere centered at the origin are then derived based on the boundary conditions and orthogonality of the vector harmonics, for the harmonics dictated by the incident field, based on the fact that the field in the origin is finite and the scattered far-field waves are traveling away from the origin. The solution for the scattering cross-section of a spherical object by a x-polarized plane wave traveling along z axis comes in the form of[54]

$$\sigma_s = \frac{2\pi}{k^2}\sum_{n=1}^{\infty}(2n+1)(|a_n|^2 + |b_n|^2) \tag{2-64}$$

where the Mie coefficients a_n and b_n are

$$a_n = \frac{m\psi_n(mx)\psi_n'(x) - \psi_n(x)\psi_n'(mx)}{m\psi_n(mx)\xi_n'(x) - \xi_n(x)\psi_n'(mx)} \tag{2-65}$$

$$b_n = \frac{\psi_n(mx)\psi_n'(x) - m\psi_n(x)\psi_n'(mx)}{\psi_n(mx)\xi_n'(x) - m\xi_n(x)\psi_n'(mx)} \tag{2-66}$$

Here $m = \frac{n_s}{n_m}$ is the relative refractive index of the scatterer to the medium, $x = ka = \frac{2\pi n_m}{\lambda_0}a$ is the size factor, and ψ_n and ξ_n are Riccati-Bessel functions,

$$\psi_n(y) = yj_n(y) \tag{2-67}$$

$$\xi_n(y) = yh_n^{(1)}(y) \tag{2-68}$$

where j_n and $h_n^{(1)}$ are the spherical Bessel functions of the first and third kind, where the latter is also known as the Hankel function of the first kind.

The angular dependence of the scattering, however, should be sought in the scattered electric field expressed as

$$E_s = \sum_{n=1}^{\infty} E_n\left(ia_n \boldsymbol{N}_{e1n} - ib_n \boldsymbol{M}_{o1n}\right) \tag{2-69}$$

where

$$E_n = i^n \frac{(2n+1)}{n(n+1)} E_0 \tag{2-70}$$

$\mathbf{N}_{o1n}$ and $\mathbf{M}_{e1n}$ are the valid vector spherical harmonics for the scattered electric field and are expressed as:

$$\boldsymbol{M}_{o1n} = cos\,\varphi\,\pi_n(cos\,\theta) h_n^{(1)}(kr)\hat{\boldsymbol{e}}_{\boldsymbol{\theta}} - sin\,\varphi\,\tau_n(cos\,\theta) h_n^{(1)}(kr)\hat{\boldsymbol{e}}_{\boldsymbol{\varphi}} \tag{2-71}$$

$$\begin{aligned} \boldsymbol{N}_{e1n} = {} & cos\,\varphi\, n(n+1)\, sin\,\theta\,\pi_n(cos\,\theta)\frac{h_n^{(1)}(kr)}{kr}\hat{\boldsymbol{e}}_{\boldsymbol{r}} \\ & + cos\,\varphi\,\tau_n(cos\,\theta)\frac{\left[r h_n^{(1)}(kr)\right]'}{r}\hat{\boldsymbol{e}}_{\boldsymbol{\theta}} \\ & - sin\,\varphi\,\pi_n(cos\,\theta)\frac{\left[r h_n^{(1)}(kr)\right]'}{r}\hat{\boldsymbol{e}}_{\boldsymbol{\varphi}} \end{aligned} \tag{2-72}$$

$\pi_n(\cos\theta)$ and $\tau_n(\cos\theta)$ are the angle dependent functions based on first order Legendre function of first kind, P_n^1,

$$\pi_n(cos\,\theta) = \frac{P_n^1}{sin\,\theta} \quad and \quad \tau_n(cos\,\theta) = \frac{dP_n^1}{d\theta} \tag{2-73}$$

These functions are the main reasons for the scattering lobes and 3 dimensional scattering profile and can be computed by an upward recurrence:

$$\pi_n(cos\,\theta) = \frac{2n-1}{n-1}\, cos\,\theta\,\pi_{n-1} - \frac{n}{n-1}\,\pi_{n-2} \tag{2-74}$$

$$\tau_n(cos\,\theta) = n\ cos\,\theta\,\pi_n - (n+1)\pi_{n-1} \tag{2-75}$$

where the first two initial terms are $\pi_0 = 0$ and $\pi_1 = 1$.

The scattering from a spherical core-shell structure has been solved using a similar approach, as detailed in 55.

2.4 Effective medium theories

When dealing with a complex electromagnetic medium consisting of a mixture of different materials, it can be convenient to express the average effect of these materials in the apparent permittivity of a homogenized effective medium. Such simplification can be especially useful when calculating the polarizability of particles, or in the case of molecular adsorption of a molecule to the surface of a scatterer (**Paper III**) which can be interpreted as a change in the composition of the immediate layer of the medium around the scatterer and thus a change in the permittivity of that layer. Here some of the most common homogenization theories that are be useful when working with small scatterers of the type explored in this thesis are presented.

The unit cell of a random inclusion in a dielectric medium can be considered as concentric spheres, much smaller than the wavelength, where the inner one indicates the inclusion and the outer one being the host, embedded in a surrounding medium, with respective relative permittivity of ε_i, ε_h and ε_m. It was shown by Maxwell Garnett that effective permittivity of this system, ε_{eff}, follow[56,57]

$$\frac{\varepsilon_{eff}-\varepsilon_m}{\varepsilon_{eff}+2\varepsilon_m}=f\frac{\varepsilon_i-\varepsilon_m}{\varepsilon_i+2\varepsilon_m}+(1-f)\frac{\varepsilon_h-\varepsilon_m}{\varepsilon_h+2\varepsilon_m} \tag{2-76}$$

where f is the volumetric ratio of inclusions to the host. When the surrounding medium has the same refractive index as the host material, this equation reduces to

$$\frac{\varepsilon_{eff}-\varepsilon_h}{\varepsilon_{eff}+2\varepsilon_h}=f\frac{\varepsilon_i-\varepsilon_h}{\varepsilon_i+2\varepsilon_h} \tag{2-77}$$

In a more general form, valid for N different inclusions, equation 2-77 can be expressed as,

$$\frac{\varepsilon_{eff}-\varepsilon_h}{\varepsilon_{eff}+2\varepsilon_h}=\sum_{i=1}^{N}f_i\frac{\varepsilon_i-\varepsilon_h}{\varepsilon_i+2\varepsilon_h}\quad where\ f_h=1-\sum_{i=1}^{N}f_i \tag{2-78}$$

Note that the assumed unit cell leading to equation 2-76, can also be valid for a small spherical core-shells particle with core and shell permittivity of $\varepsilon_c=\varepsilon_i$ and $\varepsilon_s=\varepsilon_h$ in a surrounding medium ε_m which is the route of resemblance of effective permittivity of such particle[58] with Maxwell Garnett mixing formula. For such particle, with core volume to total volume fraction of f, the effective permittivity can be derived as[58]

$$\varepsilon_{eff}=\frac{(\varepsilon_s-\varepsilon_m)(\varepsilon_c+2\varepsilon_s)+f(\varepsilon_c-\varepsilon_s)(2\varepsilon_s+\varepsilon_m)}{(\varepsilon_s+2\varepsilon_m)(\varepsilon_c+2\varepsilon_s)+f(\varepsilon_c-\varepsilon_s)(2\varepsilon_s-2\varepsilon_m)} \tag{2-79}$$

The effective permittivity of a lipid vesicle as a core-shell particle can approximated using equation 2-79 (see **Paper III**).

The Maxwell Garnet formula, as is evident in the equation 2-78, is not symmetric relative to host and inclusion, which means the calculated effective medium depends on which material is considered as host and which for inclusions. Therefore Maxwell Garnett approximation is usually best suited when the volume faction of the host is much larger than the fraction of the inclusions. When the fractions of the host is comparable with any of the inclusion materials, Bruggeman effective medium theory may provide a better estimation of effective permittivity; as it does not depend on which material is considered the host. The Bruggeman estimate can be derived from equation 2-76 if we assume the Maxwell Garnett unit cell (an spherical core with multiple shells in general case) is immersed in a surrounding medium with permittivity ε_B, equating the effective permittivity of the compound material, ε_{eff},

$$\frac{\varepsilon_{eff} - \varepsilon_B}{\varepsilon_{eff} + 2\varepsilon_B} = \sum_{i=1}^{N} f_i \frac{\varepsilon_i - \varepsilon_B}{\varepsilon_i + 2\varepsilon_B} = 0 \qquad (2\text{-}80)$$

In such conditions the sphere turns invisible to light and does not scatter.[48] According to Bruggeman effective medium theory, a permittivity ε_B that can satisfy the equation 2-80 is the effective permittivity of the compound medium. In contrast to the Maxwell Garnett mixing formula, here, all different materials enter the equation symmetrically relative to the effective permittivity which makes the result independent of which one is the assumed as the host material. However, a complication of this approach is that for a N-component medium the Bruggeman equation results in an N^{th} order polynomial equation with N possible solutions, which only one of them represents the effective permittivity of the medium[59,60].

It should be emphasized that both of these theories provide an estimate of the effective permittivity medium considering the impurities are in form of subwavelength spheres and the incident electric field inside them is not disturbed.[57] There are extension to both Maxell Garnett and Bruggeman theories that include the size of the inclusion into account, or considers spheroidal inclusions.[61–63]

2.5 Fluorescence microscopy

The waveguide evanescent microscopy platform developed in this work offers fluorescence imaging capabilities with a sub-diffraction axial resolution. Through **Paper I-VI**, we have benefitted from that capability and use fluorescence imaging as a reference to compare the scattering microscopy with, or extract more information about the entity under study. Moreover in **Paper V**, we have used TIRF microscopy to study kinetics of supported lipid bilayer formation on glass. Therefore, in this chapter we briefly review some of the important concepts regarding fluorescence as a phenomena, mainly based on reference 64 and 65, and introduce the working principle of TIRF microscopy.

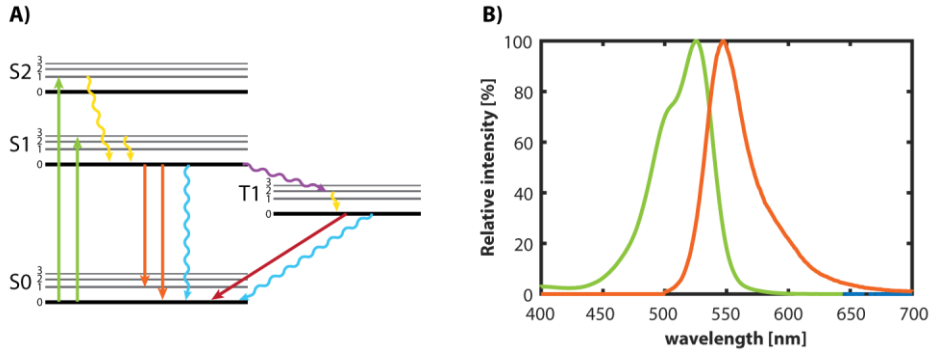

Figure 2.3. A) A Jablonski diagram illustrating the ground state, S0, the first two excited singlet states, S1 and S2, and the first triplet sate, T1 and the first 3 vibrational level for each state. The common transitions between these states are presented as straight and curly arrows for radiative and nonradiative processes respectively. Green: excitation, yellow: internal conversion or vibrational relaxation, orange: emission, cyan: nonradiative relaxation, purple: intersystem crossing, red: phosphorescence. B) Absorption (green) and emission (orange) spectra for Rhodamine 6G.

2.5.1 Fluorescence

Fluorescence microscopy is a central technique in many scientific fields. Most commonly, it makes use of special types of molecules that can emit light at wavelengths higher than that of the illuminating light. These molecules are commonly called fluorophores and can be used as labels when attached to an entity of interest, or as probes, sensitive to changes in their environment. By proper labeling of molecular components of interest, images that represent the spatial distribution and number of that particular molecule can be generated, after eliminating the illuminating light by proper optical components.

The phenomenon that include adsorption of light by a molecule and leads to a change in wavelength of the emitted light is called photoluminescence.[64] This process is usually illustrated using a so called Jablonski diagram (Fig. 2.3A); a diagram showing the energy levels of the fluorophore at different excited states. Usually the molecule is found at its lowest vibrational energy level in the electronic ground state, S0. Upon absorption of a photon, the molecule is excited to a higher energy states, usually to the first singlet state, S1. The absorption process occurs within on the order of 10^{-15} seconds, during which the nuclei is not affected, and therefore the vibrational states do not change. Depending on the photon energy, the molecule usually ends up at slightly different vibrational energy states in S1, within which it decays to the lowest energy level of the state S1(0) through vibrational relaxation at a time scale of 10^{-12} seconds, by dissipating

its energy in heat. Subsequent relaxation of the molecule to the ground state, S0, can then occur through either radiative or nonradiative mechanisms.

The radiative mechanisms, fluorescence or phosphorescence, include generation of a photon with a lower energy than that of the exciting photon. If during the excitation process, the electron spin is conserved, the radiative relaxation happens within on the order of 10^{-8} seconds and is called fluorescence. However if the electron spin is altered (intersystem crossing), the relaxation to the ground state is forbidden according to Pauli exclusion principle, and the excited state is maintained for a longer time, usually in the order of 10^{-3} to tens of seconds, and hence, the radiative relaxation occurs long after the excitation. This process is called phosphorescence and the long-lived excited state in is called triplet state. The phosphorescence is not a likely process for the dyes selected for in fluorescence microscopy.

For an isolated nonradioactive relaxation mechanisms that do not involve other molecules and conserve the molecular integrity, the energy of excited molecule is dissipated through vibrations into heat. The rates of radiative and non-radiative mechanisms differ for different fluorophores and defines the quantum yield of fluorescence process[64]

$$Q = \frac{k_f}{k_f + k_{nr}} \tag{2-81}$$

where k_f is the rate of the fluorescent relaxation (the reciprocal to fluorescence life time) and k_{nr} is the rate of all non-radiative relaxation pathways combined. Further, a fluorophore in any of its excited states can transfer its energy to the other molecules, either though collisions or dipole-dipole energy transfer which can result in quenching or fluorescence resonance energy transfer (FRET). These are both categorized as non-radiative relaxation process which lower the quantum yields of the fluorophore of interest. In addition, if a fluorophore is subjected to intense light illumination, it goes through many absorption and emission cycles. This increases the probability of the molecule to exist in a highly reactive excited state, making it more likely to become oxidized or undergo other chemical changes that turn it into non-fluorescent (photobleached) entity.

These different relaxation rates are obviously key characteristics of a fluorescent dye that influence many of its properties. A fluorophore with higher relative radiative to non-radiative rate, has a higher quantum yield (Eq. 2-81). The overall relaxation rate to the ground state also governs how often the molecule is available for excitation and how many times it can go through an emission cycle, which in turn influences its brightness. On the other hand, as the overall relaxation rate of a dye decreases, the reactive excited dye spend longer time interacting with its environment, making it more prone to quenching and photobleaching. This in turn affects the quantum yield, brightness and photostability of the dye. It is for the same reason that fluorophores usually selected for

fluorescence microscopy have negligible phosphorescence; not only their emission will stretch out in time over the measurement window, but they will also be faint and prone to quenching and photobleaching.

Figure 2.3B shows the absorption and emission spectra for a typical fluorophore, Rhodamine 6G, used in this work in **Papers II**, **III** and **V**. As a result of coupling of the closely spaced vibrational energy levels within each state, the absorption and emission spectra are smooth curves that cover a broad range of wavelengths (energies). The difference between the absorption and the emission peaks is referred to as Stokes shift, which implies how well the fluorescence emission can be separated from the excitation light.

The absorption and emission processes can also be described with dipole moments, which are usually referred to as absorption and emission transition dipole moments (TDM). The absorption of a fluorescent dye is at its maximum if its absorption-dipole moment is parallel to the polarized light and vanishes if the two vectors are perpendicular to each other. On the other hand, the emission of an excited fluorophore occurs through its emission-transition dipole and is polarized along its orientation. The absorption- and emission-dipole moments of a molecule can with respect to each other, and the polarization of the emitted and excitation light can be therefore different. This is called intrinsic anisotropy, and is the measure of how much the polarization of emitted light is changed relative to the excitation light. In general, the optical anisotropy of a dye is defined as[64]

$$r = \frac{I_{\parallel} - I_{\perp}}{I_{\parallel} + 2I_{\perp}} \tag{2-82}$$

where $I_{\parallel}$ and $I_{\perp}$ are the intensity of parallel and perpendicular component of the emitted light, relative to the polarization of the source and plane of incidence. The optical anisotropy is another property of a fluorescent dye that can be influenced by the emission rate. At room temperature, the suspended dye molecules experience rotational diffusivity that to a first approximation depends on the viscosity of the medium and volume of the dye. During the time it takes for the molecule to relax to the ground state, due to rotational diffusivity and fluctuation of the dye and the complex it might be attached to, the molecule orientation changes which results in a less polarized emission and a lower anisotropy. This can also be observed in polymers.[66] Due to molecular anisotropy and the stochastic nature of the emission with respect to the incident light, the dyes attached to fluorescently labeled lipids, proteins and nanoparticles will typically fluoresce at different phase, point in time and polarization with respect to each other. This, in turn, leads to an incoherent emission process, and consequently, the fluorescence intensity corresponds to sum of the average intensity emitted by each fluorophore. Consequently, the emitted light intensity is proportional to the illumination light intensity integrated over the fluorescently labeled entity. This is in contrast to the scattering intensity (see the section on scattering and **Papers II** and

III), which to a first approximation is proportional to the second power of the integration of the electric field over the illuminated object.

2.5.2 Total Internal Reflection Fluorescence microscopy

There is a long history behind the development of fluorescence microscopy,[67,68] with the central driving force being to improve the quality of the imaging by pushing the optical resolution, limit of detection and to maximize the information content of the images. Nowadays several fluorescent microscopy techniques are available that offer sub-diffraction limit axial resolution, such as confocal microscopy[69,70], total internal reflection fluorescent microscopy (TIRF)[12,71], as well as sub-diffraction limit axial and lateral resolution concepts, such as for example stimulated emission depletion microscopy (STED),[72,73] stochastic optical reconstruction microscopy (STORM)[74] and photoactivated localization microscopy (PALM).[11]

A fluorescence imaging technique that share many similarities to the waveguide evanescence microscopy developed in this thesis is total internal reflection fluorescence (TIRF) microscopy. Introduced and developed mainly by Axelrod D. during the 1980s,[12,71] TIRF microscopy offers subwavelength axial resolution in the imaging with a contrast that can be used for single molecule imaging.[13,75–77] The novelty of TIRF microscopy lies in its illumination scheme, which has made it compatible with other microscopy methods such as confocal,[78] STED,[79] and STORM.[74] The TIRF illumination mechanism achieves its high image contrast and sub-diffraction axial resolution by confining the exposure within a thin sheet of light, with adjustable thickness from sub 100 nm to about 1 um.[44] This is done by illuminating the sample at an angle, θ_i, that can sustain total internal reflection (TIR) condition between the microscopy substrate, that is usually glass, and the medium.

$$\theta_i > \theta_c = arcsin(n_m/n_s) \tag{2-83}$$

where θ_c is the critical angle and n_m and n_s are the respective refractive of medium and substrate. The conditions here is very similar to the guiding conditions of a waveguide, where the mode angle should be larger than the critical angle (see page 9), and the solution to this electromagnetic problem at the medium side of the interface will be similar to equation 2-30, where $\beta_m = k_0 n_s \sin(\theta_i)$ and $k_{clad} = k_0 n_m$. According to equation 2-36, in this case the penetration depth of the light intensity in the medium can be written as

$$\delta = \frac{\lambda_0}{4\pi} \frac{1}{\sqrt{n_s^2 \, sin^2(\theta_i) - n_m^2}} \tag{2-84}$$

This will result in a thin sheet of light in the medium, bound to the substrate-medium interface, with an exponentially decaying intensity perpendicular to the interface,

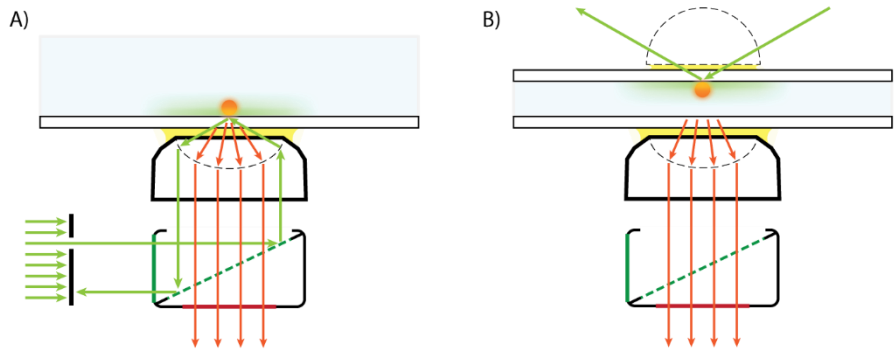

Figure 2.4. Common TIRF illumination strategies: A) Objective-based, B) Prism-based.

$$I = I_0 \, e^{-\frac{z}{\delta}} \tag{2-85}$$

where z is the distance from the interface in the medium, and I_0 is the light intensity at the interface. For most biological assays where the experiments are performed in aqueous solution on microscopy glass slides, the penetration depth for a certain illumination wavelength, λ_0, can be adjusted by changing the incident angle.

Two main implementation of TRIF microscopy are illustrated in figure 2.4. In objective-based solutions (Fig 2.4A), the illuminating light is usually shaped in crescent and send through a high NA oil immersion objective so that it generates a parallel beam of light illuminating the interface only at the TIR condition. In this case the angle of incidence and thus the penetration depth is set by adjusting where the light enters the objective relative to its axis. Another main category of TIRF implementations is prism-based (Fig 2.4B), where collimated light, usually laser, approaching the interface at TIRF angle using a prism. In this case and the fluorescent light is usually collected on the opposite side, through oil or water immersion objective. Although this implementation might seem easier, but oil impression objective can result in optical aberration especially in multicolor imaging. More sophisticated examples of TIRF implementations can be found in reference 14.

3 Cell membrane model systems

The origin of life and the appearance of early primitive cells is hypothesized to be concurrent with the incorporation of RNA in spontaneously formed membrane-bound compartments made of amphiphilic molecules about 4 billion years ago.[80–82] Although the exact pathway of the emergence of live cells is unknown, the cell membrane certainly had a critical role as an initial ingredient. Today the cell membrane, consisting of more than 100 different types of lipids and various proteins, is commonly described by a *fluid mosaic* model, with the integral proteins assumed to be dissolved in a 2D viscous lipid bilayer solvent, where the polar and ionic parts of the proteins are protruding from the membrane and their nonpolar parts are mostly protected in the hydrophobic part of the membrane.[83] The cell membrane, in its very intrinsic function, defines the boundary of the cell, and differentiates the cell interior form its environment. It protects the genetic information of the cell and is responsible for all interactions of the cell with its environment, including signal transduction and selective transport of larger compounds in and out of the cell.

The importance of studies related to cell membranes and proteins becomes evident when considering that 60% of drugs on the market are targeting membrane proteins while these proteins make up not more than about 22% of all proteins in the body.[84] Moreover, particles engulfed in cell membrane mimics have been appreciated as possible drug delivery vehicles[85,86] However, the native cell membrane is a very complex medium where characterization of its individual components usually relies on highly sophisticate isolation protocols, which may both denature the relevant components and/or result in very low extraction levels. For this reason, studies of biophysical

processes using simplified cell-membrane mimics, such as supported lipid bilayers (SLBs) have been increasingly used in biophysical studies of cell membranes with and without incorporated proteins. However, it is crucial to well-characterize these cell membrane mimic to make sure they accurately represent the native cell membrane in the selected application and do not influence the function of biological entity under investigation. Therefore, large emphasis has been placed on identifying and characterizing underlying mechanisms that determine how they are formed as well as their nature under different conditions.[87–94]

In this work, cell membrane models were used either to study their fundamental properties or to use some of their well-known properties to study biomolecular interactions and address biologically relevant questions. While conventional TIRF microscopy, with the capacity to resolve individual fluorescently labeled lipid vesicles, was used to investigate the kinetics of SLB formation, the novel evanescent-light scattering microscopy platform developed in this thesis was used to assist in the label-free studies involving such model systems. More specifically, in **Paper V** we investigate the kinetics of the SLB formation process occurring through a vesicle adsorption and rupture mechanism that is often the method of choice for SLB formation on silica-based surfaces. In **Paper III** we demonstrate SLB formation on a silica-like surface using evanescent-wave scattering and lay the ground for interpreting the scattering signals from lipid vesicles when used in various biological essays. In **Paper II** we demonstrate how waveguide evanescent-light microscopy can operate both in labeled and label-free modes in studies employing vesicles as a cell membrane mimic to study enzymes and antibodies interacting with the membrane. In **Paper IV** we combine the fluorescent and scattering signals obtained from the waveguide microscopy platform, to investigate exosomes, a type of lipid vesicle a naturally produced by many cells with high clinical and pharmaceutical relevance,[95] isolated form a human mast cell line. Finally, as demonstrated in the additional result section of the thesis, the combination of lipid bilayer as a 2D fluid and evanescent-light scattering microscopy platform with embedded microfluidic capabilities, in conjunction with findings of **Paper III**, may offer a significant contribution to the characterization of the biological nanoparticles.

Due to frequent appearance of different lipid based entities in this work, this chapter is dedicated to a brief introduction of the common lipid-based model systems.

3.1 Lipids

Lipid molecules, which together with membrane proteins are the main component of the cell membrane, are hydrocarbon based amphiphilic molecules consisting of a hydrophilic (ionic or zwitterionic, i.e. net charge depends on pH) head group and a hydrophobic tail region that may consist of one or more nonpolar fatty acid chains.[83] Figure 3.1A shows an example of a lipid from the phosphatidylcholine (PC) family that

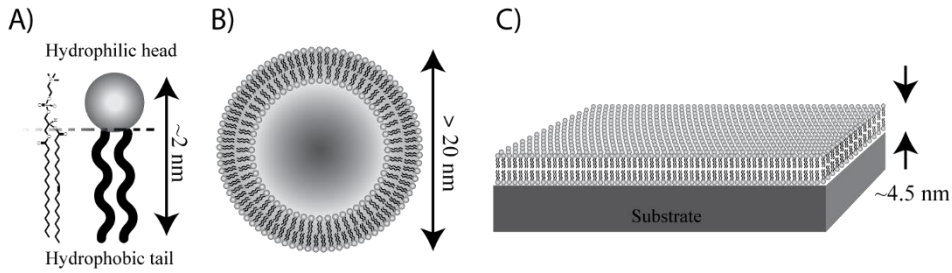

Figure 3.1. Phospholipids and their common self-assemblies: A) POPC phospholipid (1-palmitoyl-2-oleoyl-sn-glycero-3-phosphocholine) chemical structure and the common schematic representative of double tail lipids. B) Cross-sectional view of a unilamellar lipid vesicle as a spheroidal Lipids self-assembly. C) Lipids self-assembled into a Supported lipid bilayer (SLB). [Figure A, is adopted from reference [101] with permission from Olov Wahlsten]

constitute more than 50% of eukaryotic membranes.[96] PC lipids have a zwitterionic head group, electrostatically natural at physiological pH. Depending on their polarity, and size of head group and volume of occupancy by their tails, lipids tend to self-assemble in specific structures in aqueous solutions. Many of these self-assembled structures can be used as model systems of natural cell membranes and are thus valuable in studies of either basic biophysical properties of lipid membrane such as phase separation[97] and raft formation,[98] or a phenomena as complex as exocytosis[99] or intercellular communication.[100]

3.2 Model systems

The cell membrane is a complex structure consisting of hundreds of different types of lipids, proteins and other entities. Studying the cell membrane in this form is extremely challenging since currently available instruments do not offer the spatial resolution needed to discern all the different entities responsible for different interaction. Therefore, simplified model systems are used to mimic the cell membrane and study different aspects by specifically controlling the molecular composition of the model membrane. Here we focus on two of the main model systems, lipid vesicles and supported lipid bilayers (SLB).

3.2.1 Liposomes / Vesicles

Many lipids self-assemble into lipid vesicle structures in aqueous solution. The lipids are in this case assembled in a double layer (bilayer), with the hydrophobic tails sandwiched in between the hydrophilic head groups to minimize the free energy of the system. The bilayer is then wrapped in the form of a spheroidal object (Figure3.1B). With the membrane separating an inner form an outer compartment, it serves as a good model

system for cells,[102] cell compartments,[103,104] extracellular vesicles and exosomes,[105] to mention a few.

One of the very first protocols for preparation of lipid vesicle and the proof of their existence was presented by Bangham et al. in 1964.[106] In their approach, the lipid mixture is dissolved in organic solvent and dried under vacuum to form a thin film on the walls of a rotary evaporator flask. After rehydration and gentle hand-shaking, the lipid film collapses from the walls forming multilamellar lipid vesicles. Depending on preferred vesicle size and preparation volume, sonication,[107] extrusion[108] and high pressure homogenization[109] are, nowadays, the most popular methods for unilamellar lipid vesicle preparation. The lipid vesicles have been used in studies of artificial[110] and native cell membrane properties[111,112] as well as drug carriers.[113,114]

3.2.2 Supported lipid bilayer

On certain hydrophilic supports, lipid molecules can self-assemble into a thin sheet consisting of two layers of lipids (lipid bilayer) with the hydrophilic heads in contact either with surface or the aqueous environment, with their hydrophobic parts sandwiched between the heads (Figure 3.1C). The first SLB model systems were prepared by transfer of lipids form air-water interface using Langmuir-Blodgett technique[115] while later implementations were facilitated by either vesicle adsorption and rupture[116] or direct lipid deposition using solvent-assisted techniques[117,118] among others.[119,120] Nowadays one of the most popular SLB formation protocols is vesicle adsorption and rupture on silica-based surfaces that owes its proliferation to its simplicity and reproducibility. The well-defined 2D nature of SLBs has made them compatible with many surface based analytical methods.[121] This has opened up for their successful use in studies of membrane proteins,[122,123] membrane phase separation,[94] membrane-virions[124] and -nanoparticles[125] interactions and drug-screening.[126,127]

4 Fabrication and processing

Nanotechnology emerged from microelectronic processing techniques and has spread into almost all fields of science[128–131]. In fact, by contributing entirely new possibilities, nanotechnology has become one of the major forces that brings different scientific fields and researcher closer together. It has already contributed to development of many new sensor technologies[132–136] and improved efficiency[137] and yield with respect to energy consumption, storage capacity etc.[138] Life-science is one of the disciplines that has benefited significantly from advances in nanotechnology, manifested in the development of for example nanoplasmonics sensors[139–141], microfluidics[131,142], lab on a chip methods[143,144], to mention a few.

The work presented in this thesis owes a considerable amount of it success to the nanofabrication tools, techniques and research that was available. However, in this chapter, instead of expanding on the physics of each fabrication technique, the rationality of the chip-design and some of the challenges faced will be discussed as I walk you through each step of the fabrication process. Since the fabrication of the waveguide with microfluidic capabilities is more comprehensive, the protocols and procedure introduced here are based on **Paper III**.

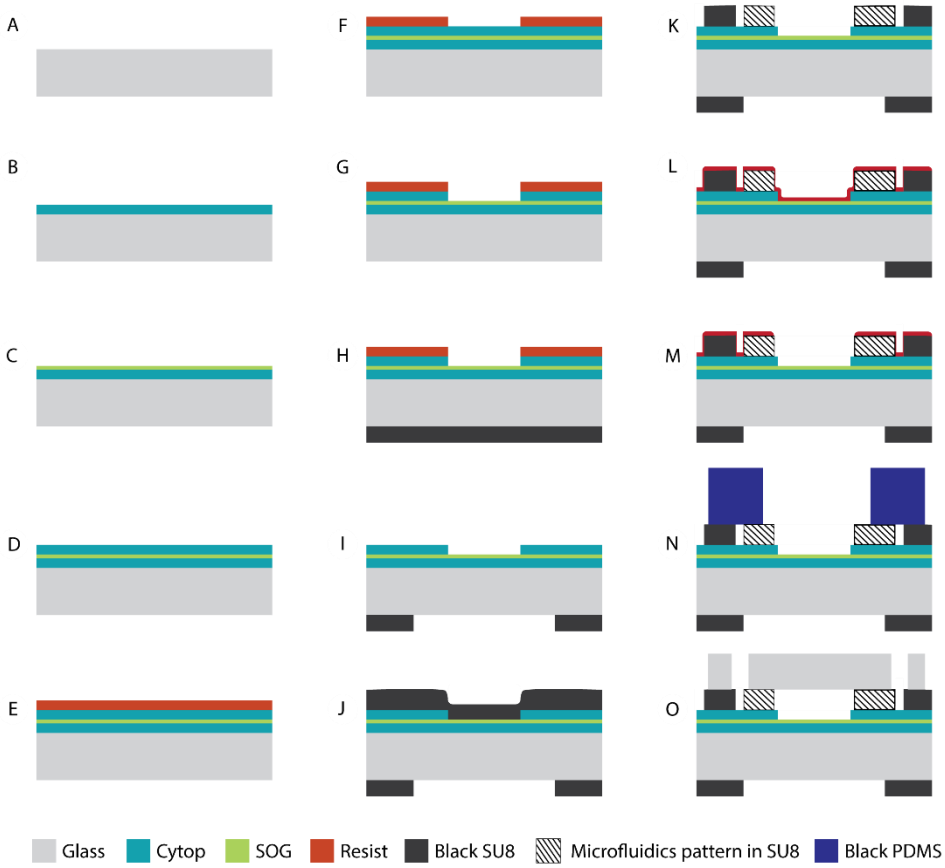

Figure 4.1.Typical processing flow of a waveguide device on glass with microfluidics ready for bilayer formation. A).Substrate preparation for Cytop coating. B) Cytop processing and activation. C) Spin on glass coating and activation. D) Cytop processing and activation E) Coating and exposure of the resist with the microfluidic patterns. F) Developing the resist. G) Reactive ion etching of the cladding to pattering the microfluidics in Cytop. H) Photolithography of black SU8 on the back side of the substrate with windows for microscopy. I) Developing the black SU8 layer. It will result in removing the photoresist on top of the substrate as well. J) Photolithography of black SU8 on top of the waveguide with Microfluidic pattern slightly bigger than the ones in Cytop. K) Developing the SU8 layer. L) Coating the waveguide with a protective layer and dicing. M) Patterning a fresh protective layer to protect the SU8, followed by oxygen plasma activation of the measurement area. N) The protective layer is removed. In case of well configuration a punched slab of black PDMS is placed on top of the measurement area. O) The protective layer is removed. If microfluidics needed, a glass substrate with hole for inlet and outlet are thermally bonded to the SU8 layer.

4.1 Choice of the material

Water constitutes most of the mass of living creatures and most, if not all chemical reaction and transport processes in our body take place in aqueous environment. As a result, for biological studies to be relevant, they must be performed in aqueous media. Further, in microscopy, there is often a need for transparent materials, and many protocols have accordingly been adopted to interface biological entities to glass substrates. Therefore, silicon oxide, which is the main constituent of glass, was chosen as the dielectric core layer of the waveguide chip. To generate a symmetric wave propagation, a highly transparent fluoropolymer called Cytop with a refractive index close to water was used for the cladding. The choice of Cytop as a chemically inert hydrophobic material has been a key defining factor for the majority of the steps in the fabrication process.

4.2 Substrate preparation

The common role of substrates is to act as solid support and provide stability to the device that is fabricated on top of it. Depending on the device and its application other properties of the substrate can be important, like its electrical properties, roughness, surface tension, adhesion, etc. Here the main criteria relates to good adhesion of the materials used during fabrication and high surface flatness, but the optical properties of the substrate, such as the amount of auto-fluorescence generated, may also be important. The choice of opaque or transparent substrates determines how the waveguide can be used in combination with different microscope setups. A transparent substrate makes the device compatible with inverted microscopes by allowing the detected light to be acquired through the substrate. This, in turn, enables for high numerical aperture, oil-immersion objectives to be applied, thereby increasing the sensitivity and image resolution that can be obtained. Since most microscope objectives are corrected for glass substrates, and considering the low roughness, availability and low cost of commercially available substrates, glass was the obvious choice of substrate material. Nevertheless, the fragile nature of the 170 μm glass substrate needed to offer compatibility with oil immersion high NA objectives makes handling and dicing of the substrate extremely challenging.

4.3 Lower claddings

For the fabrication an A-type Cytop™, CTX-809A (Asahi Glass Co.) was used. Cytop, which is a fluorine based polymer is very hydrophobic, and the fluorine chains result in very low adhesion to contacting substrates. When using glass substrates, γ-Aminopropyl-

triethoxy silane[a] (APTES) treatment can be used to promoter the adhesion of Cytop to the substrate. The APTES treatment was done by spin coating a freshly prepared 0.2 v% solution of APTES in 95% ethanol (Figure 4.1A). This was followed by a few minutes of baking to remove residual water and ethanol from the surface and also promote the binding of silane to the surface.[145] Cytop was spin coated on the silanized substrate to achieve about 4 um thick layer (Figure 4.1B). The curing of Cytop was done in a temperature controlled furnace under nitrogen with a glass beaker on top to reduce the solvent evaporation rate during baking and to improve surface flatness.[146]

4.4 Core layer

A challenge similar to that of adhering Cytop to the substrate exists when it comes to the deposition of the core layer; poor adhesion to Cytop. To overcome this challenge a thin layer of Aluminum was deposited on the Cytop surface. After Aluminum deposition, Cytop monomers on the surface is believed to be oriented and their hydrophilic COOH end group faces the surface.[146–148] The Aluminum was removed prior to core layer deposition.

Silicon oxide was chosen as the material for the core layer of the waveguide because of its compatibility with many biological assays and protocols. Since Cytop has a low glass transition temperature of 108^{o}C, one needs to devise a deposition technique that is compatible with fairly low temperature. Spin on glass (SOG) is a class of products that provided with that possibility. Although most SOG products require temperatures above 400 C for baking stage during curing, a longer baking time at lower temperature turned out be adequate in our case (Figure 4.1C).

4.5 Upper cladding

The procedure for the second cladding layer is very similar to that of the lower layer. To promote the Cytop adhesion, the core SOG layer was functionalized with APTES in the same way as the glass substrate. The Cytop layer was subsequently spun on the core layer with similar parameters as used for the lower layer. The baking for this layer was done at lower temperature to avoid the glass temperature for the lower cladding.

4.6 Opening of the measurement area

To make measurements in an aqueous sample possible, it must come in contact with the evanescent field that propagates at the interface of the core layer. The opening in

[a] $H_2NC_3H_6Si(OC_2H_5)_3$

the upper cladding was made by reactive ion etching (RIE) through a photoresist pattern, which defines the shape of the measurement area. The adhesion of the photoresist to the Cytop could be promoted in two ways; Aluminum deposition, or APTES treatment. The former procedure was explained above. The latter method was carried out by mild oxygen plasma treatment of the Cytop using a showerhead plasma chamber operated at 25W for 30 seconds. Afterwards, the sample was immediately immersed in a 2% aqueous APTES solution and kept for 10-20 minutes. This procedure improved the subsequent adsorption of APTES to Cytop and results in a rather good adhesion to the photoresist. The photoresists (Figure 4.1E) qualified for this step should be compatible with processing at temperatures as low as 90^{o}C and their corresponding developer should not affect the microscopy surface quality.

After photolithography (Figure 4.1F), Cytop was etched (Figure 4.1G) using an ICP/RIE tool (Oxford Plasmalab System 100) equipped with a laser interferometer for live monitoring of the etching process. The over exposure of the core layer to the oxygen plasma in the chamber was suspected to deteriorate the quality of the microscopy surface.

4.7 Back layer

When coupling light into the waveguide structure by placing an optical fiber next to the waveguide facet, some of the light that is supposed to be coupled in the waveguide core, leaks into the supporting glass substrate. The light coupled in the glass substrate can travel in the substrate and enter the at the collection angle of the oil immersion objective during microscopy and result in an increased background. To obviate this adverse effect a thin light-absorbing layer was patterned on the back side of the substrate. For that purpose GMC1060 (Gersteltec), that is a SU-8 resist with black dye, was mixed with SU-8 3005 and SU-8 3035 (MicroChem Corp.) in proper portions to get similar viscosity to that of GMC1060. The mixture was spin coated to a thickness of 30 μm on the back side of the glass substrate (Figure 4.1H). The layer went through soft baking at 65^{o}C and 90^{o}C for 10 and 25 minutes, respectively, and exposed for 15 minutes to pattern an opening for objective to see through. The substrate then goes through a similar baking step and followed by development (Figure 4.1I).

4.8 Microfluidics

A benefit of being able to use an inverted microscope is that it allows for easier access for possible microfluidics, which in turn makes experiments under controlled liquid flow possible. Moreover, it can improve handling and general stability of the experiment during the liquid exchange by eliminating manual pipetting. In a closed system like a microchannel, evaporation is not an issue during long experiments and the risk of

contamination from the environment will be reduced as well. However, the added-values of microfluidics come at the cost of more processing steps!

Microfluidics in SU8 has been chosen as the processing approach to make controlled micro-channels on the waveguide. In order to reduce the stray light, i.e. to shield the measurement window from environmental disturbances and loosely guided light in the usually transparent microfluidic layer, the black-dye-containing SU8 formulation used for the back layer was selected. The product builds up a very high stress and has very bad adhesion to substrate. Moreover, the black dye absorbs light even in UV range which result in decaying exposure dose through the film thickness while defining the channels by photolithography. To mitigate some of these problems, a customized mixture of GMC 1060 and SU8 3035 (MicroChem) was prepared and used. The mixture proved to have a lower stress in the film and a better adhesion and bonding properties in practice.

Since the new mixture combines properties of both products, strictly following the processing guidelines of either of the product may not be a good choice. Therefore further optimization of the processing conditions is needed. A 25 μm layer of the customized SU8 was span and processed on the top cladding (Figure 4.1J). The APTES functionalization left on the Cytop from the etching step (see step 4.6) promotes a uniform and well adhered film in the coating step. In order to achieve a better uniformity in the film, the resist was allowed to relax for at least 10 minutes after spinning. Note that the position of the microfluidic channels that are defined during the exposure step has to be aligned with the measurement windows previously etched in the Cytop (Figure 4.1K).

4.9 Dicing

The dicing of the wafer does not only serve to separate the substrate into individual waveguide devices, it also defines the quality of the extremely important facet of the waveguide and thus the efficiency of the in-coupling of light into the device. The quality of the facet is thus one of the crucial parameters in waveguide fabrication; a good facet ensures a good and efficient coupling of light in the waveguide while a facet with smeared or detached layers with lots of debris and cracks resulting from bad dicing causes little or no possibility of light in-coupling. Several parameters can affect the dicing quality including the substrate material, adhesion of waveguide layers to each other and the waveguide to the underlying substrate, blade type and properties like grit size, concentration, and matrix material, feed rate and spindle speed, etc.

Two blade series from Disco, R07 and P1A851, with synthetic diamonds and grit size of 800 served the purpose. However, the dressing step that refreshes the blade surface and exposed sharp new diamonds is essential to the quality of the cut. We did the

dressing using GC3000PB50 dressing board from Disco. Photoresist on glass has been used as a model system to evaluate the effect of different dicing parameters on the chipping of the waveguide. A spindle speed of 30 Krpm with a 0.5 mm/sec feed rate was concluded to minimize the cracks and chipping for both blades.

To protect the measurement area of the waveguide and the Black SU8 layer from contamination, a photoresist layer was spun on the wafer (Figure 4.1L). Further investigation of dicing quality showed that the thicker the resist layer, the less chipping occurs on the waveguide facet. Due to the curvature of the blade and the 180-200 µm thick substrate, the depth of dicing affects how close the fiber can get to the chip's facet, which in turn affects the coupling efficiency and the amount of stray light generated. On the other hand, if the substrate is diced through, because of rather poor adhesion of glass to the dicing tape, one risks damaging the blade. Here around 50 µm of substrate was left after dicing as a compromise between the two effects. The photoresist was removed with proper resist developer or remover after dicing.

4.10 Activating the measurement window

Even though the surface of the spin on glass core layer in the measurement window is flat (root mean squared surface roughness < 1 nm as measured with atomic force microscopy-**Paper I**) and homogenous, its properties with regards to surface functionalization and compatibility with biological entities might have been compromised in the processing steps. Spontaneous formation of supported lipid bilayers is known to be critically dependent on the quality of the silicon oxide layer. Successfull formation of an SLB can thus be considerred as a sign that the surface properties of the core layer has been preserved. Oxygen plasma cleaning is commonly applied as treatment prior to forming supported lipid bilayers on glass and silicon oxide layers. Having spin on glass, which mainly consist of silica, oxygen plasma treatment turns out to be a reproducible method for surface activation. An oxygen plasma treatment would thus be feasible as a last step before carrying out an experiment using the waveguide. However, since now being enclosed in microfluidic channels, a different protocol must be adapted.

To find an alternative activation procedure that could be applied within a closed channel, several chemical cleaning procedures such as SDS, Hellmanex alternation, cleaning with 2M sulfuric acid, treatment with 7x[149] (P Biomedicals), and Liquinox[150] (Alconox) were tested. However, none of them showed any sign of a substrate resulting in reproducible and spontaneous bilayer formation. To circumvent this problem, the activation and cleaning was instead done before enclosing the microfluidic channels with glass-SU8 bonding. Since SU8 bonding performance degrades drastically upon exposure to oxygen plasma, another photolithography step was performed to protect the SU8 while exposing the measurement area (Figure 4.1M). The oxygen plasma

cleaning was performed in a Harrick plasma chamber, PDC-002, at 30W for 40 minutes. The resist was then removed with a proper resist developer or mr-Dev 600 solvent based developer. Supported lipid bilayers could still be formed spontaneously on the waveguides weeks after the oxygen plasma treatment and bonding!

4.11 Bonding

The last processing step that has to be carried out in a cleanroom environment is bonding to seal the patterned channels on the chip. In this process a piece of glass with drilled holes for inlet and outlet is pressed on the SU8 layer at an elevated temperature. The quality and reproducibility of bonding depends on the pressure, temperature, the quality of SU8, surface cleanness. Proper care has to be taken to make sure that SU8 bonding performance is not degraded during the fabrication process by using low temperature processing and proper protection. The bonding was performed using a tool mainly developed for nanoimprint processing (CNI v1, NILT) that could provide us with the elevated temperature and pressure needed. The tool applies the pressure through a nitrogen filled balloon that presses the sample to its ceramic chuck. To achieve a good bonding, the glass-waveguide assembly had to go through a few temperature and pressure ramps and hold steps, with a slow cool down after bonding (Figure 4.1O).

After forming the microfluidic channels, given a good surface quality for bilayer formation, it turns out cleaning the channels with 2-10% 7X at 80^{o}C can sustain the surface quality and allow reusing of the device.

5 Image processing

The fabricated waveguide device, whether it is made on silicon or glass or equipped with microfluidics or not, provides a convenient way to confine the light illumination to the surface and renders low background in microscopy imaging. To evaluate experimental results, whether performed using an upright or an inverted microscope, or in fluorescence or scattering mode, one needs to analyze the acquired images, and carefully monitor changes in each frame and/or step of the experiment. The information one searches for can be hidden in the appearance or disappearance of entities on the surface, changes in the intensity of the signal or correlations of signals measured in different microscopy channels, etc. To extract as much information from the microscopy images as possible, some image processing algorithms and codes were developed in a MATLAB environment. Although the development of these algorithms does not necessarily have a scientific value in their own right, they define to which extent reliable information can be extracted and thus influence the data interpretation. As image analysis was an integrated part in all papers of this thesis, the aim of this chapter is to describe the image-processing algorithm developed for analyzing scattering and fluorescence microscopy data, and how they were applied. When we describing the algorithm in the following, the terms particle/object/entity are interchangeably used to refer to the features in an image representing an object on the microscopy surface.

5.1 Image preparation

The optical elements in the collection path of a microscope, like objectives, lenses, filters and mirrors have slightly different properties at different wavelength, known as chromatic aberrations. Therefore when using multiple imaging modes, e.g. scattering and fluorescence, or different filter cubes, or beam splitters, image alignments should be done to compensate not only for the lateral mechanical movement of the image but also for slightly different optical magnifications or other distortions. Therefore, Before starting with the image analysis, the recorded stack of microscopy images were aligned either using a Template Matching plugin[151] in ImageJ or, when needed, using more sophisticated image processing functions in MATLAB.

5.2 Image processing algorithm

Independent of the microscopy method used for image acquisition, all images were analyzed with the same algorithm, although implemented slightly differently from case to case. After loading an image, based on the pixel intensity distribution of the image, a global background intensity is estimated for the image. This is used as a reference intensity level for the particle detection. The intensity profile of the image is then compared to numerous intensity thresholds defined relative to the image background intensity. Isolated intensity peaks that both protrude from the background intensity have a minimum number of adjacent pixels will be consider for further analysis.

If the image suffer from uneven illumination the local background may vary from one region to another. To make sure the pixel identification was above a minimum signal-to-background ratio, the intensity profile of each identified peak was compared to its surrounding pixels. After passing the local threshold test, if a peak consist of a minimum number of connected pixels, it will be considered as a “potential” particle, if not, the peak is discarded.

Occasionally, especially in scattering mode, due to intra- or inter-particle light interference fringes appear around very bright particle or between closely neighboring particles. The code was designed to either include these fringes in the intensity evaluation of the “parent” particle, or to remove them from the list of “potential” particles. This was achieve by a lateral expansion of the corresponding pixel sets recognized as “potential” particles and further intensity evaluation of the resulting connected pixels. This process usually does not influence the detection of parent particles or isolated particles with no fringes, however adjacent particles with drastically different intensities can be affected. As a compromise, a faint particle located a few pixels from a much brighter particle might be excluded from the data set.

At this stage the “potential” particles that are in contact with the image borders are neglected and the remaining are considered as “detected” particles. To ensure that the

area assigned to a particle includes all representative pixels, regions in the image assigned to a detected particle were expanded with a few pixels, while making sure there was no overlap with other identified areas.

Before reporting the intensity of a detected particle, the dark-count, I_{D}, of the camera, which corresponds to the average pixel intensity when camera is completely in dark, is subtracted from all the frame, thus defining the intensity value of each pixel. The local background intensity, I_{B}, for each detected particle is calculated based on the average intensity of pixels in its vicinity that were not part of any other detected particle. The total intensity of a detected particle, I_t, is then calculated as the integrated intensity of pixels assigned to the particle after local background subtraction

$$I_t = \sum_{\substack{i=pixels\ assigned \\ to\ the\ particle}} (I_i - I_B) \tag{5-1}$$

The signal to background ratio for each particle can now be calculated.

$$SBR = \frac{I_t}{I_B} \tag{5-2}$$

A unique index is then assigned to each detected particle allowing it to be tracked between different frames and in different microscopy imaging modes. Tracking particles between two consecutive frames is based on a global particle assignment approach with priority for particles with the least displacement between subsequent frames. Particles in the new frame that are not assigned to any particles in the previous frame are distinguished as newly arrived particle.

Different implementation of this algorithm has been used to interpret data presented in all appended papers; in **Paper I** when using fluorescent beads to compare the performance of waveguide fluorescence and scattering with epi-fluorescence microcopy, in **Paper II** when analyzing the scattering and fluorescence intensities of adsorbed vesicles, in **Paper III** for characterizing the waveguide and interpreting cholera toxin binding to lipid vesicles, in **Paper IV** when analyzing the waveguide scattering and florescence intensities from surface adsorbed exosomes, in **Paper V** to track the vesicles adsorbed to and ruptured on the glass substrate imaged using TIRF microscopy, and in the **additional results chapter** when using combined waveguide scattering and fluorescence microscopy to tracking tethered lipid vesicles on a supported lipid bilayer when moved using a laminar flow.

6 Summary of results

Together with the **Additional Results** in **Chapter 7**, the majority of work carried out to develop the waveguide scattering and fluorescence microscopy setup that is the heart of this thesis is summarized in the appended papers. This includes fabrication and characterization of the waveguide device and demonstrations of its capacity to offer new insights in certain biologically relevant applications.

In **Paper I**, we present the fabrication procedure developed to make a functioning waveguide on silicon substrates and characterize its optical properties in some detail. In **Paper II**, we demonstrate the applicability of the waveguide device and its potentials for label-free biomolecular sensing and microscopy. In **Paper III**, we introduce a new waveguide design compatible with inverted microscopes and with built in microfluidic channels, and perform additional optical characterization to deduce models to estimate the collected scattering light. In **Paper IV**, the device made on silicon is used to evaluate exosomes isolated from a human mast cell line. Finally, in **Paper V** TIRF microscopy was used to evaluate the bilayer formation process, with the intention to better understand and control the process when used in various applications using the waveguide. In particular, the combined knowledge from **Paper III** and **Paper V** forms a base for the results presented on 2D flow nanometry in **Chapter 7**. In all papers, different image processing codes were developed based on the earlier described algorithms and used to evaluate the performance of the devices and to process the experimental data. The following sections provide a brief prologue to the work detailed in these papers.

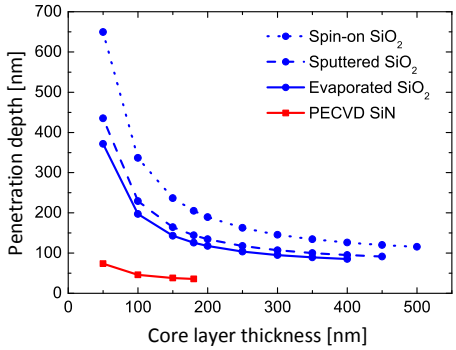

Figure 6.1: Calculated penetration depth of optical waveguides with Cytop cladding, for different core layers at 532nm TE excitation.

6.1 Paper I

The first paper lays the foundation for the majority of the work presented in the thesis. This paper is mainly focused on the fabrication and characterization of the waveguide platform developed on an opaque silicon substrate, thus being compatible with upright microscopes. The waveguide platform provides an alternative tool for surface-sensitive evanescent-field sensing[28,141,152–154] and microscopy.[12,33] Having the platform compatible with label-free nanoparticle microscopy requires a high quality waveguide illumination with low background. This can be achieved using a cladding material with a refractive index close to water. Fluorinated polymers are one of the very few materials which satisfy that criteria, but impose in turn serious challenges with respect to the fabrication process. In this paper we introduce a low temperature fabrication scheme that overcomes those challenges. This way we were able to fabricate working waveguides with four different core materials (Spin on SiO_2, sputtered SiO_2, evaporated SiO_2 and SiN). Based on the dispersion relation of these material the penetration depth was calculated at an illumination wavelength of 532nm (Fig. 6.1), demonstrating a wide tenability window, ranging from below 100 nm to above 1 μm.

To benchmark the device towards alternative microscopy systems, the performance of SOG-core waveguides in scattering (WGS) and fluorescence (WGF) was assessed relative to epi-fluorescence microscopy by imaging surface-bound fluorescent latex beads (Fig. 6.2A). For each microscopy mode, the signal-to-noise (SNR) and signal-to-background (SBR) values were calculated and compared in the presence of different concentrations of suspended beads in the bulk solution. The results, summarized in figure 6.2, show superior performance of waveguide relative to epi mode, especially in scattering mode and at high bulk concentrations. This indicates the potential of waveguide evanescent-field microscopy especially in complex biological medium.

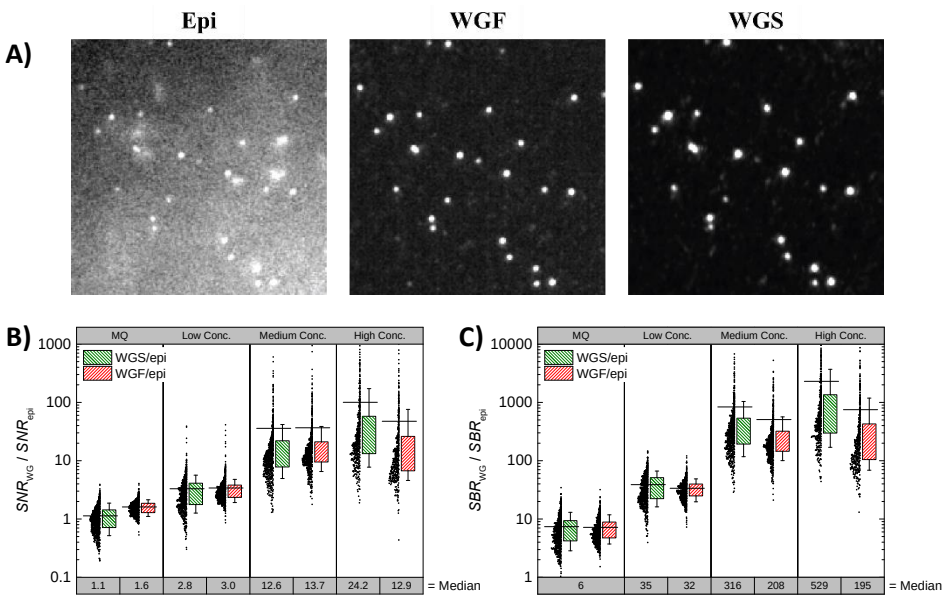

Figure 6.2. A) Microscopy images of 100nm fluorescent polystyrene beads on the waveguide surface using epi-fluorescence, waveguide fluorescence and waveguide scattering microscopy. B) Signal to noise (SNR) and B) signal to background (SBR) assessment of the surface adsorbed beads in waveguide fluorescence (WGF) and scattering (WGS) modes relative to epi-fluorescence microscopy at different concentration of beads in the solution.

6.2 Paper II

The waveguide platform on silicon (described in **Paper I**) was here used to demonstrate its wide applicability in various biological applications. We first demonstrate detection of fluorescently labeled lipid vesicles, with modal diameters of ⌀150 nm, in both waveguide fluorescence and scattering. Based on the size distribution of the vesicles and the number of vesicles that were detected in fluorescence but not in scattering mode, we conclude that vesicles down to 80nm can be detected. Restricted to experiments in stagnant liquids, we demonstrate binding of mouse antibiotin-IgG2a to surface immobilized ⌀200 nm lipid vesicles containing biotinylated lipids, and compare changes in scattering signal with biotin-free fluorescently labeled vesicles of similar size. As expected the scattering signal of biotin-free fluorescent vesicles does not change; however, a clear binding curve can be detected for the rest of the vesicles with a signal-to-noise that was estimated to correspond to around 30 antibodies.

Since single proteins are usually too small to result in detectable scattering signals upon binding to a vesicle, the single-molecule detection capability in scattering mode was

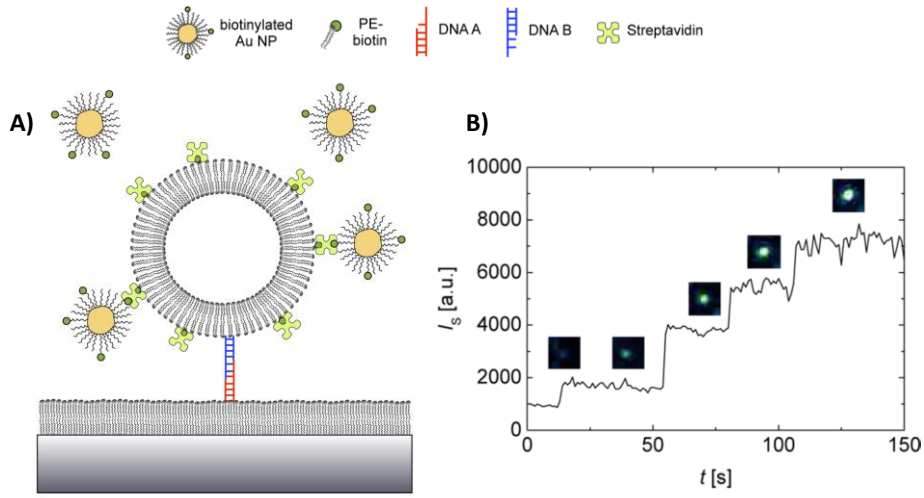

Figure 6.3. Binding of Au nanoparticles to single vesicles. (a) Schematic representation of the model system for studying single molecule binding events using gold NPs as labels. Streptavidin-functionalized vesicles were immobilized to a biotin-free supported lipid bilayer via a DNA linker. (b) Scattering intensity from a single vesicle as a function of time upon binding of 18 nm in diameter biotin-functionalized gold NPs to the vesicle. Upon addition of gold NPs, specific binding of individual NPs to the vesicles was observed, while no binding was observed to the supported lipid bilayer. The inset images are approximately 2x2 μm^2 wide and show the increasing scattering intensity from the single vesicle at different times during the process.

verified using gold nanoparticles with a diameter of ⌀18 nm. Such gold nanoparticles, functionalized using thiol chemistry with PEG5K/PEG5K-biotin, were exposed to surface-immobilized ⌀100 nm vesicles containing 1% biotinylated lipids previously incubated with streptavidin on the surface (figure 6.3A). Upon binding of biotin-modified gold nanoparticle to streptavidin coated vesicles, step-wise increases in the scattering intensity of the immobilized vesicle could be observed (figure 6.3B), each possibly originating from binding to a single streptavidin protein.

Another advantage of using waveguide scattering microscopy is in cases where fluorescent labeling can affect the phenomena under study. One such example is the enzymatic activity of phospholipase A2 (PLA2), which is commonly studied by tracking how PLA2-induced lipid digestion leads to changes in fluorescence intensity of lipid vesicles containing a small fraction of head labeled lipids (Fig. 6.4A).[20,155] We investigated the possibility of probing this system by comparing the digestion signal of individual fluorescently labeled vesicles in both fluorescence and scattering mode. Figure 6.4B shows the digestion signal recorded for a ⌀100 nm vesicle immobilized via NeutrAvidin on a PLLgPEG/PllgPEG-Biotin functionalized waveguide core. Upon exposure to PLA2 at 25nM, both the scattering and fluorescence signal decreases; however, the rate of changes is not equal in the fluorescence and scattering channels.

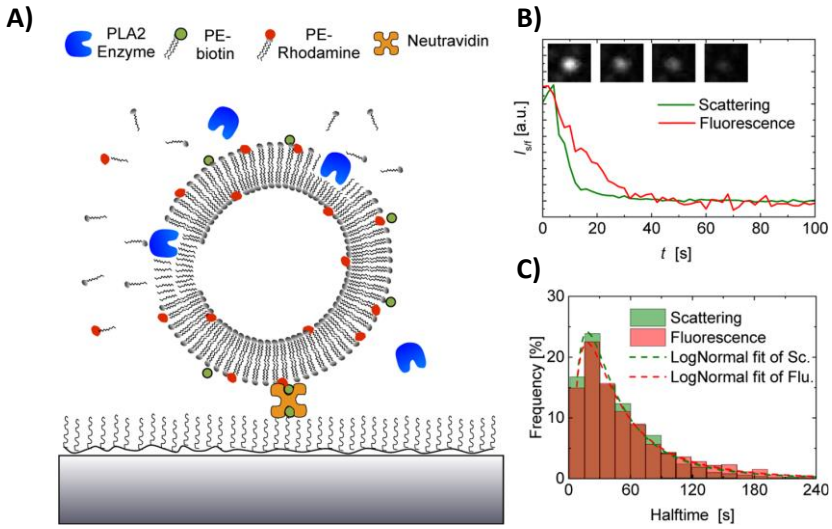

Figure 6.4. Monitoring enzyme activity of individual vesicles in scattering and fluorescence. (a) Schematic representation of the model system used to monitor the digestion of a single 100 nm immobilized vesicles by the enzyme PLA2 as a function of time. (b) Scattering (green curve) and fluorescence (red curve) intensity of a selected vesicle upon PLA2 digestion. The micrograph insets (2x2 μm^2 wide) show the corresponding appearance of the fading vesicle as observed in scattering mode at different times during the acquisition. (c) Distribution of halftimes for the measured vesicles extracted from scattering intensities (green bars) and fluorescence intensities (red bars).

As the scattering scales with 2nd power of the lipid leaflet volume and fluorescence in this case scales with surface area, the digestion time constant in scattering is indeed expected to be roughly half of that observed in fluorescence. Taking that in to account, the measured time constants in fluorescence and scattering mode agree very well (Fig. 6.4C), suggesting that such processes can indeed be performed without labeling but also that the fluorescent labels on the lipids does not influence the enzymatic activity of PLA2.

Finally, by studying human-derived platelet and demonstrating the time evolution of cell adhesion to the glass-like core layer of our waveguide in scattering, we show using waveguide scattering microscopy that one can resolve the interaction of live cells with the surface, with results similar to other microscopy methods.[156]

6.3 Paper III

Paper III can be considered as an extension of the work presented in **Paper I** and **Paper II**. Here the fabrication process presented in **Paper I** was adapted and optimized for glass substrates. This not only allows the waveguide platform to be used on inverted microscopes in combination with high numerical aperture (NA) objectives, but also

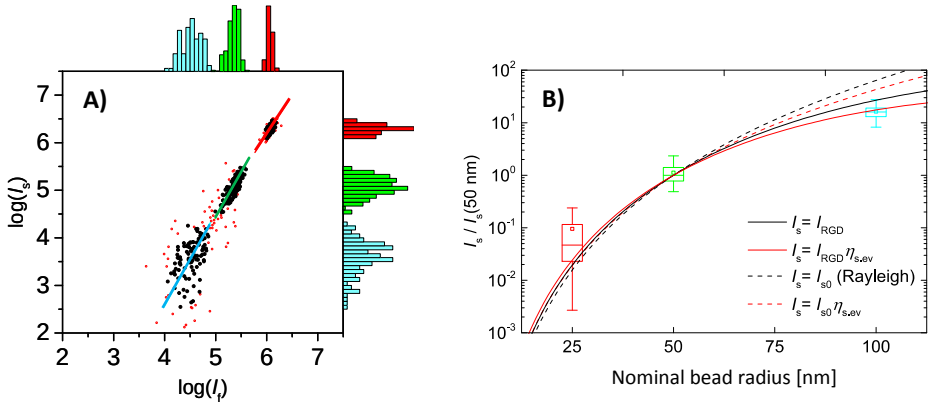

Figure 6.5. A) log-log representation of scattering intensity versus fluorescence intensity obtained with waveguide illumination of three different populations of fluorescent polystyrene beads (nominal diameter of: 51 nm, 100 nm and 200 nm) adsorbed to the surface. The red hollow data points represent the least likely 8% of the bivariate lognormal distribution of each cluster (corresponding to Mahal distance of larger than 3), which were excluded from analysis. The blue, green and red lines are linear fits through the selected data points (black solid circles) of the three observed clusters, with slopes of 1.98, 1.87 and 1.70. The intensity distributions are projected on each of the axis. B) The scattering intensities normalized to the mode intensity of the beads 100 nm beads, as function of beads nominal radius. For comparison, the scattering intensities according to Rayleigh-Gans-Debye (solid lines) and Rayleigh (dotted lines) theories are plotted in, both with (red color) and without (black color) the evanescent illumination correction.

allows for more convenient handing of liquids in open configuration and incorporation of microfluidic channels directly on the waveguide without disturbing the microscopy path. This is expected to expand the applicability of the waveguide device while improving the liquid handling. Although may seem as a straightforward task, significant efforts had to be invested into fabrication details in order to reach a performance, matching that obtained on opaque silicon substrates.

The impact of numerical aperture (NA) on the quality of the WGF and WGS imaging of 100 nm beads displayed an increasing trend for the signal-to-background ratio (SBR) up to NA = 1. However optical anomalies that caused the drop in SBR, already appear at slightly lower NA values, and hence, NA of 0.85-0.9 was concluded the best choice for the current configuration.

Figure 6.5A shows the scattering versus the fluorescence signal from 3 bead sizes after correction for the efficiency of dye incorporation in the nanospheres. We also used adsorbed polystyrene beads to investigate how well the measured scattering and fluorescent signals could be estimated with common scattering theories taking the effect of evanescent illumination into account. An accurate consideration of the evanescent illumination should include the effect of different dipole moments in the

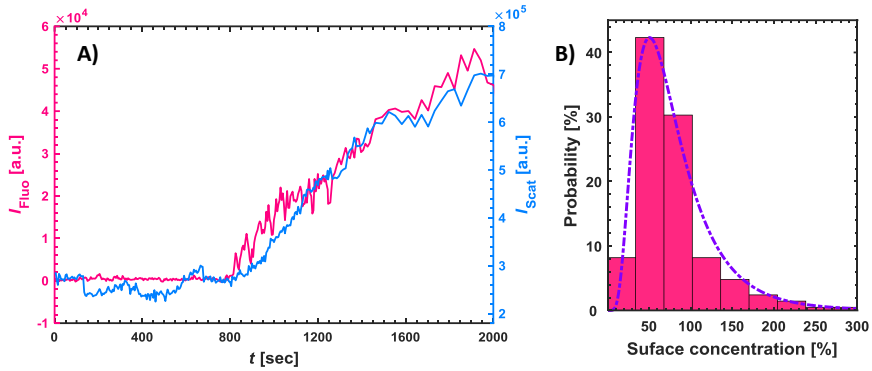

Figure 6.6. A) Cholera Toxin B (CTB) binding to a POPC vesicle containing 4 mol% GM1 recorded simultaneously in fluorescence (red) and scattering (blue). B) Histogram and fitted lognormal distribution of the increase in the vesicles leaflet thickness due to binding of CTB estimated from the changes in scattering intensity of the vesicles during binding process.

shape factor of Rayleigh-Gans-Debye (RGD) or the calculation of Mie solution. We approximated this effect only as a change in the strength of dipole moment, or the intensity of an equivalent illuminating plane wave, which resulted in a good agreement with the acquired data for the beads (6.5B). This thus provides a basis from which to interpret the scattering signal using simplified models, which is important when investigating complicated dynamic changes in scattering signals.

We also extended the findings for beads as a model system, to biologically relevant experiments similar to one presented in **Paper II**, namely specific protein binding to surface-immobilized lipid vesicles. Since the size and refractive index of the adsorbed protein is comparable to that of the membrane leaflet of the vesicle, the polarizability of the vesicle before and after adsorption changes dramatically, inducing a significant change in the scattering signal (Fig. 6.6A). Our estimation, based on the RGD scattering model, shows that under the conditions of our experiment, the protein covers in most cases around 50% of the vesicles surface (Fig. 6.6B). More accurate estimations of the adsorbed layer should be possible to achieve by considering the influence of adsorbed layer in the shape factor, or using computer simulation.

In comparison with **Paper II**, several improvements were achieved, in addition to the added value obtained by incorporating microfluidic channels. First, the scattering model more accurately predicts the recoded signals. Second, the applicability of the WGS to significantly smaller biological particles was accomplished, demonstrated using vesicles with diameters of ~75 nm rather than 150 nm. Thirds, clearly detectable signals upon binding of an almost ten time lighter protein (12 kDa vs 160 kDa) was accomplished, pointing towards a higher detection sensitivity. We also present a more advanced model to estimation the scattering signal in the protein adsorption studies.

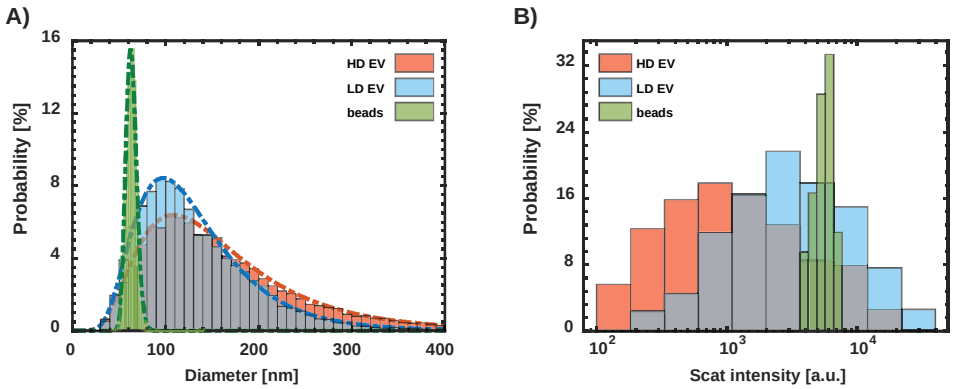

Figure 6.7. a) Normalized size distributions of unlabeled LD and HD EV samples (measured with NTA operated in light scattering mode) and polystyrene beads (measured with AFM). b) Scattering intensity distributions of unlabeled LD and HD EV samples, and the calibration beads in semi-log scale.

6.4 Paper IV

Extracellular vesicles (EVs) are membrane vesicles secreted into the extracellular environment by many types of cells.[157] Their recently discovered roles in cellular function and communication[158–163] have made them interesting candidates for diagnostic[164–166] and therapeutic applications.[167–170] However, efficient use of their different functions requires further advancement in characterization methods.[36,171] In particular, their large diversity makes single nanoparticle analytic tools especially relevant, as it may aid classification of EV samples into different functional sub-populations.

Size, density and refractive index are among the relevant properties that can aid the classification of EVs.[36,37] The microscopy platform developed in this work can in principle provide information about some of these properties, especially when combined with complementary techniques. In **Paper IV**, we use the waveguide evanescent-field microscopy device to investigate EVs isolated from a human mast cell line, and separated into two subpopulations based on their buoyant density: low density (LD) and high density (HD) EVs. Both LD and HD populations demonstrated rather similar size distribution when evaluated by nanoparticle tracking analysis (NTA), with modal diameter/standard deviation of 97 nm/64 nm and 109 nm/93 nm respectively (Fig 6.7A). Since the high-density population also had a slightly higher modal size, one intuitively expects them to scatter more than the LD population. However our results demonstrated that the peak of the scattering intensity is ~3 times lower for the HD than the LD sample (Fig 6.7B).

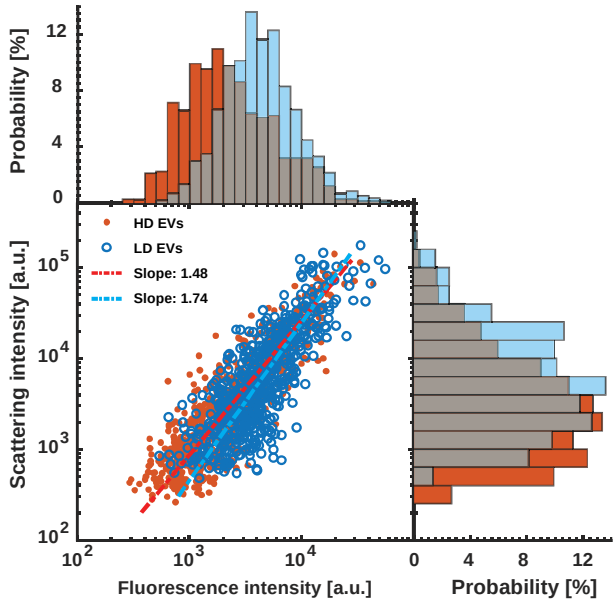

Figure 6.8. Correlation between the scattering and fluorescence intensity distributions of PKH26-labeled EV populations. Main: log-log plot of I_{scatt} vs. I_{fluo} for EVs individually visualized both in scattering and fluorescence. (top: fluorescence intensity distribution, right: scattering intensity distribution.)

To scrutinize this peculiar observation, we made use of the possibility of the waveguide platform to provide simultaneous information about the scattering and fluorescence intensity at the single EV level. By labeling EVs with a self-inserting fluorescent membrane dye, PKH26, and measuring the scattering and fluorescence intensity of individual EVs, we searched for a possible explanation to the low scattering intensity of the HD population in differences in the lipid content. Also, when scattering is plotted against fluorescence in a logarithmic representation (Fig. 6.8), one can deduce other relevant information about the EVs. Since the scattering intensity increases with size of the scatterer, the strong correlation between scattering and fluorescence intensities for each population indicates that the fluorescence labeling, which is expected to scale with the lipid membrane content, scales with to size of the EV. Further, despite the slightly larger hydrodynamic size of the HD sample, it had lower fluorescence intensity than the LD sample. As the fluorescence intensity of a membrane dye is expected to be proportional to lipid content of the membrane, this indicates lower lipid content in HD EVs, likely compensated with a higher protein content. As the proteins have higher buoyant density relative to lipids (1.4-1.5 g/cm^3 versus ~1 g/cm^3),[172] this observation is consistent with the differences in the buoyant density of the two population. However, considering that refractive index relative to that of water is about 40% higher for proteins than lipids, the observation is not consistent with the higher scattering

recorded observed for the LD sample. It is in this context worthwhile to note that the slope of the data in figure 6.8 correlates with the effective refractive index of the EVs; the LD EVs exhibit a higher slope than HD EVs, indicating a higher effective refractive index for this population. It is therefore reasonable to assume that lumen of low density population contain more biological material than that of the HD population.

These findings made us suggest that the membrane of the high density EVs is permeable to the medium in the density gradient used to separate the two populations. If the solute of the gradient replaces the water inside of EVs, they will have a higher buoyant density than EVs with intact membranes, as the buoyant density of the latter is expected to be dominated by water. A permeable / damaged membrane may also be more prone material loss from the lumen, which would be consistent with the observed lower scattering intensity.

6.5 Paper V

Supported lipid bilayers (SLBs)[122,124,173] serve as an important model for cell membranes and a fundamental understanding of the mechanisms underpinning the formation process have been the subject of many theoretical[90,174–178] and experimental[179–183] investigations. In addition to its general importance, the interest in the subject in the context of this thesis was form when we started investigating the quality of the SLBs on the core of the waveguide, crucial in experiments aimed at performing 2D flow nanometry[38] (see **Chapter 7**). The results reported here were, however, performed on one of the most common substrates for SLB based studies, namely glass, and specifically borosilicate glass. The experiments were conducted using total internal reflection fluorescence microscopy (TIRF).[12] In this microscopy method (see Chapter 2) an evanescent wave, similar to that of the waveguide microscopy platform, is excited at an interface between two medium, usually glass and water, by shining the illuminating light at angle higher than the critical angle of the two medium. This illumination technique when combined with fluorescent microscopy, can deliver appreciable information about adsorbed fluorescent entities.[184–187] Having a small subpopulation (1 in 100) of the suspended vesicles fluorescently labeled,[150] we could follow the SLB formation process from early patch formation to full SLB coverage, with a contrast and a resolution high enough to discern the SLB edge boundary. This allowed us to study the SLB patch growth during the vesicle adsorption and rupture processes. Our analysis show that the patch growth rate, reflected in the SLB front velocity (Fig. 6.9), increases dramatically despite the fact that the surface density of adsorbed vesicles during the patch growth changes negligibly. When compared to the spread of supported lipid monolayers and bilayers on hydrophobic and hydrophilic surfaces from a stagnant lipid source, where the font velocity decreases with $\frac{1}{\sqrt{t}}$ time dependency,[88,188,189] this can be considered a significant finding. The observation of stagnant patches at early stages in the process also

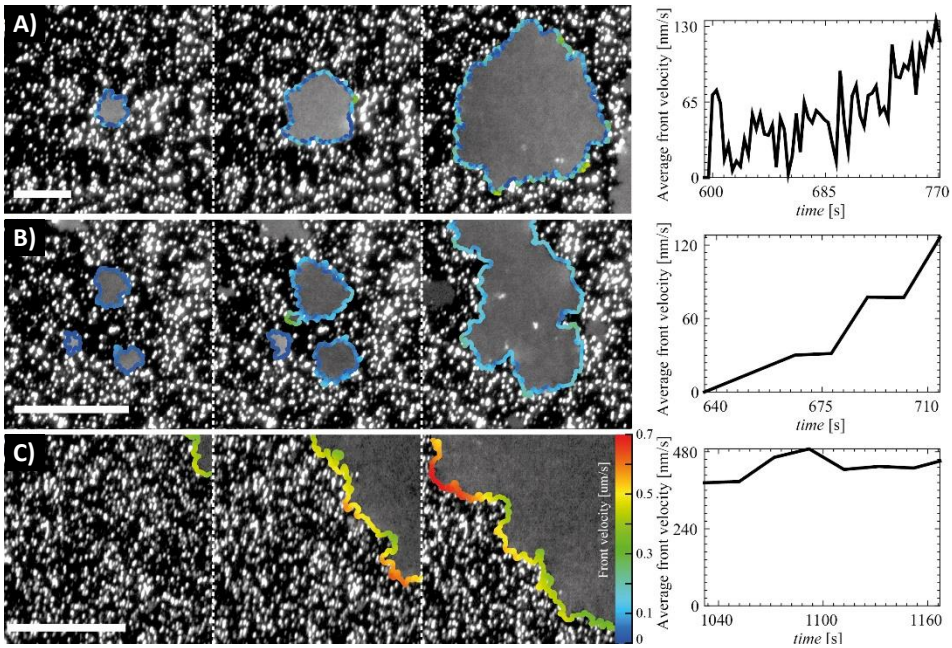

Figure 6.9. Typical patterns observed during the SLB-patch growth and the corresponding dependence of the average front velocity on time: (A) Single patch formation and expansion (snapshot interval 60 s). (B) Small patches merging into a bigger patch (snapshot interval 24 sec). (C) Propagating SLB front (snapshot interval 30 sec). Scale bars are 20 µm. The color of the lines showing the front indicates the local front velocity.

challenges previous observations, suggesting significance role of the direct adsorption of vesicles to the bilayer edge, in the SLB formation process.[190,191]

To theoretically address the rate of SLB growth, two extreme scenarios were examined: *local relaxation* and *full relaxation*, which respectively represent either no lipid rearrangement upon patch formation or instantaneous lipid rearrangement. Upon vesicle rupture into a rather circular SLB patch according to the local relaxation model, the lipid material overlapping with the existing SLB will be lost. In the full relaxation model, all lipids from ruptured vesicles will in contrast coalesce with the SLB patch induced their rupture rendering a larger, perfectly circular, patch. The full relaxation model, which could represent the vast majority of observation, also takes into account that if the lipid content of surface adsorbed vesicles around an SLB patch is larger than the occupied substrate area, there is an accelerated growth, while if the surface coverage is low, the model suggests a decaying growth rate, as also occasionally observed for early formed patches.

7 Additional results

Size is one of the most important standardization and classification parameters of biological nanoparticles (BNPs).[37,171] Dynamic light scattering (DLS) and nanoparticle tracking analysis (NTA) are two common techniques for size determination of suspended nanoparticles.[5,192–194] As detailed below, both methods deduce the hydrodynamic size of particles from measurements that reflect nanoparticle diffusivity in the solution. DLS is an ensemble measurement method that determines the diffusivity of the nanoparticles in the suspension from the temporal fluctuations of their scattered light. Due to the huge difference in scattering cross-section of large and small nanoparticles and due to the difficulty in discerning closely located distribution peaks in the ensemble measurement, DLS is not a suitable technique for characterizing polydisperse samples.[195] Despite this limitation, DLS offers an astonishing measurement limit, down to 1 nm in monodisperse samples.[4] NTA size estimation is instead based on a more explicit determination of the diffusivity of individual nanoparticles via tracking their Brownian motion in the solution, either in fluorescence or scattering mode. Unlike DLS, NTA performs better with polydisperse samples but, due to low signal intensity and fast diffusion of small nanoparticles out of the focal volume, its accuracy drops considerably for particles smaller than ⌀50 nm.[196]

Our group recently developed a new method for size determination of nanoparticles, named 2D flow nanometry (FNM), that offers a higher accuracy for polydisperse samples than NTA.[38] In FNM the hydrodynamic size of a particle is estimated from the analysis of its movement under a constant flow, while the particle, instead of freely moving in the solution, is tethered to 2D fluid supported lipid bilayer (Fig. 7.1A). In this way, the

nanoparticle motion becomes confined to a 2D lateral displacement and remains in focus throughout the measurement. NFM has been so far successfully demonstrated in fluorescence mode, where compared with NTA it has not only reduced the limit of detection but also increased the accuracy of the size determination. Although tethering required for FNM makes the method more complex that NTA, the fact that the particles remain in focus throughout the analysis makes it possible to determine both the size and the emitted intensity of the analyzed nanoparticles (see detailed description below). This, in turn, makes it possible to specifically target BNPs with certain receptors directly from a complex biological samples, and measure their size without any interference from other entities in the bulk of the sample; something that neither DLS nor NTA can offer.

A recurring theme in this thesis, has been to evaluate the scattering and fluorescence intensities of beads and BNP, and from such measurements draw conclusions about their physical properties, which sometimes are based on the size distributions measured with NTA or DLS. Although, these techniques determine the size distribution of the sample with a reasonable accuracy, the exact size of every individual nanoparticle in the microscopy experiments is not known. Hence, we have been restricted to correlate the measured signals (fluorescence or scattering intensity) from individual nanoparticles with their size distribution, or to use the modal value of the size and intensity distributions. Additionally, in **Paper IV** we show that the possibility to correlate fluorescence intensity with scattering intensity on individual particle level offers new physical insights. However, missing the size of individual particles, this information can be compared on the sample level only if all BNPs share similar structural properties (e.g. being shell-like or dense spheres). Having the size information of each individual BNP, one could correlate the size of BNP to its scattering and fluorescent intensity, and thus determining the refractive index, surface area, composition etc. on single BNP level. This could not only improve the accuracy of the BNP characterization, but also make it possible to differentiate between sub-populations within a complex sample.

In an attempt to achieve that goal, during this thesis work significant efforts were invested in constructing a device that makes the combination of the 2D flow-nanometry concept with the waveguide device possible. Since tethering of nanoparticles to a 2D fluid requires supported lipid bilayers of high quality, we characterized how supported lipid bilayer are formed upon vesicle adsorption and rupture process, certain aspects of which being summarized in **Paper V**. In the following section, we report on the preliminary results obtained so far, aimed at demonstrate the compatibility of 2D flow nanometry on a waveguide device fabricated on a transparent support, as detailed in **Paper III**. The transparent support makes the waveguide concept compatible with inverted microscopes and facilitates the incorporation of the microfluidics required to control the motion of tethered nanoparticle. In this chapter, first the physics behind 2D flow nanometry is introduced, and then our preliminary experimental advances on its realization using the “transparent” waveguide platform is presented. Although not

completed within the frame of this thesis work, it is our vision that the concept will further expand the device to a multidimensional characterization platform for biological nanoparticle and beyond.

7.1 Theory of 2D flow nanometry

The random movement of NPs in a viscous solution is known as Brownian motion, and the diffusion constant D of a spherical particle with radius r in a solutions with viscosity η at temperature T was derived by Albert Einstein as[7]

$$D = \frac{K_B T}{3\pi\eta d} \tag{7-1}$$

under the assumption that the mean free path of molecules of the solution is much smaller than the size of the NP,[197] and with a friction between the NP and the solution as described by Stoke.[7,197] The equation is therefore usually referred to as the Stoke-Einstein equation. The probability distribution of displacement of such particle has a Gaussian form[7,198]

$$p\left(x|_{x_0}, \Delta t\right) = \frac{1}{\sqrt{4\pi D\Delta t}} e^{-\frac{(x-x_0)^2}{4D\Delta t}} \tag{7-2}$$

Therefore, the mean square displacement (MSD) for the Brownian motion calculated along an arbitrary axis x is[7]

$$MSD(\Delta t) = \langle (x(\Delta t) - x_0)^2 \rangle = 2D\Delta t \tag{7-3}$$

The mean square displacement (MSD) of a particle tracked in intervals of Δt for N frames, can thus be deduced from its tracks for any $n\Delta t$ time durations[199],

$$MSD(n\Delta t) = \frac{1}{N-n} \sum_{i=1}^{N-n} \left(\vec{d}_{i+n} - \vec{d}_i\right)^2, \qquad n = 1, \dots, N-1 \tag{7-4}$$

where $\vec{d}_i$ is the position of the center of the NP at frame i. For a spherically symmetric particle diffusing in a isotropic medium, with displacement measured in m dimensions, the relation between MSD and diffusivity D can be expressed as[200]

$$MSD(n\Delta t) = 2mD\, n\Delta t \tag{7-5}$$

In the nanoparticle tracking analysis method, the MSD of individual freely diffusing NPs is calculated by evaluating their displacement within the focal plane at certain time intervals, and the size of the particle is deduced using equations 7-1 and 7-5 assuming a spherical nanoparticle. When a tracked particle gets away from the focal plane, the error in the position determination raises and eventually the particle will be lost as it escapes

the focal volume. This problem gets more dramatic for smaller NP which not only diffuse faster but also are much fainter scatterers. To increase the accuracy of size determination for smaller particles in NTA, one needs to have a more sensitive sensor, stronger lasers, higher acquisition rate with shorter acquisition times and better position determination algorithms. However, despite such improvements, as the particles freely diffusing in and out of the focal volume, one particle can be tracked many times and contribute with a higher weight to the estimated size distribution.

If the nanoparticle is instead bound to a fluid interface in its displacements, it can be kept in focus throughout the entire measurement, and under a flow one can also make sure the particle is not counted more than once. This can be achieved by tethering/linking the NP to a 2D fluid bound to the surface, like a supported lipid bilayer (SLB). In this case, the random diffusivity of the tethered NP is not only defined by its size, but also by the number of tethers it has to the 2D fluid. Therefore by increasing the number of tethers for fast diffusing NP one can slow them down, which can both improve the accuracy of the position determination, while maintaining the exposure time. In practice the number of tethers linking the NP to the 2D fluid may vary from one NP to the other, and as a results diffusion will no longer be a bijective function of radius. Therefore the previous approach described for size determination of suspended NPs cannot be directly applied in this case.

According the general Stokes-Einstein relation, the diffusion and mobility, μ, are related as,[38]

$$D = \mu\, K_B\, T \tag{7-6}$$

Further, the mobility of a NP can deduced from its terminal velocity, v_d, under a constant flow:

$$\mu = v_d / F_d \tag{7-7}$$

where F_d is the drag force exerted mainly at the NP anchoring point, resisting its movement in a laminar flow.

Inducing a constant laminar flow above the surface where the diffusing NP is tethered to the 2D fluid, the movement of the NP can be divided in two components (Fig. 7.1A); the movement along the flow that is mainly governed by the drag force for long distances, and the movement perpendicular to the flow due to random diffusion. Under such conditions, the diffusion constant and terminal drag velocity can be deduced from the two components of NP movement, and therefore the drag force can be estimated in a FNM experiment.

$$F_d = K_B\, T\, v_d / D \tag{7-8}$$

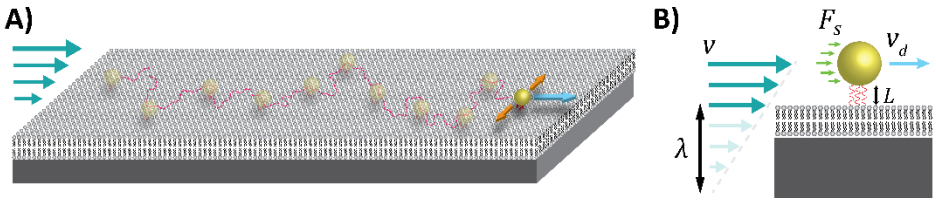

Figure 7.1. A) A nanoparticle (NP) tethered to a 2D fluid like a supported lipid bilayer (SLB) under a constant laminar flow, moving along the flow while diffusing. B) Laminar flow with a slip length of λ and velocity of v at its center of NP induces a sheering force, F_s, that causes the NP to move a long the flow at a terminal velocity of v_d. At this velocity the drag force F_d and the sheering force are equal.

where D and v_d are idenependently determined from the perpendicular random diffusion and the flow-induced terminal drag velocity, respectively. The drag force at the terminal velocity balances with the sheering force, F_s, applied from the fluid to the particle. The sheering force exerted on a small spherical particle of radius r under a laminar flow at a velocity v in a fluid with viscosity η can be calculated using Stokes' drag equation.[201]

$$F_s = F_d = 6\pi\eta r\, v \tag{7-9}$$

The velocity of a fluid close to a surface can be approximated with a linear profile. Having a slip length of λ and a tether length of L, the velocity at the center of the sphere linked to the bilayer is then,

$$v = v_0\,(r + \lambda + L) \tag{7-10}$$

where v_0 is the laminar flow velocity at the unit distance consider and linear profile. In this way, being able to determine the drag force, F_d, acting on each individual nanoparticle characterized in a 2D FNM experiment (Eq. 7-8), one can determine the size of each individual NP via:

$$F_d = A\eta v_0 r(r + \lambda + L) \tag{7-11}$$

where A is a constant that includes 6π and other geometrical factors relating to the shape of the NP and the possible inhomogeneous flow around it. A and λ can be deduced for a specific setup with calibration measurements using NPs of known size.

Given how easy it is to determine the size of freely diffusing NPs, this may appear as an unnecessarily complicated way to determine the size of a nanoparticle. However, in NTA, the NPs diffuse in and out of the focal plane, which makes a reliable determination of their scattering (or fluorescence) intensity under the same illumination condition almost impossible. Hence, in commercially available products, it is hardly possible to correlate the intensity measurements to the size at the single NP level. However, using 2D flow nanometry, the NPs remain in focus throughout the analysis, allowing the

Figure 7.2. Schematic representation of a fluorescently labeled lipid vesicle tethered using complementary double strand DNA pairs, α and β to a POPC supported lipid bilayer formed on the waveguide core layer.

magnitude of the signal used to determine the position of the NP, to be correlated to its estimated size.[38]

7.2 Preliminary experimental results

The aim of the experiment described in this section was to simultaneously visualize SLB-tethered fluorescent nanoparticles in both scattering and fluorescent mode while hydrodynamically propelled on an SLB formed on the core of a transparent waveguide chip merged with microfluidic channels as described in **Paper III**. A stack of black PDMS, glass and PDMS with thicknesses of 0.5, 1 and 3 mm, respectively, were aligned and bounded to each other using oxygen plasma, such that inlet and outlet holes matched the design of the microfluidics on the waveguide chip. To seal the microfluidic channels (WxH: 1000 x 40 μm^2), the stack was bounded to the black SU8 on top of the waveguide chip (see **Paper III**) with the black PDMS side facing the device. The PDMS-glass-PDMS stack fulfills several goals; the black PDMS restricts stray light reaching the measurement area, the thick PDMS works as an adapter between the tubing and the device, the glass prevents the thin black PDMS to collapse into the microfluidic channels, helps mounting the fragile waveguide device on the holder, and facilitates handling of the waveguide chip (Fig. 7.2).

A 488 nm laser was edge-coupled to the waveguide through a single mode, polarization maintaining optical fiber operated in TE mode. The light was collected using a Nikon Ti-E microscopes and an oil immersion 100X iris objective (CFI Plan Fluor 100X with iris, Nikon). To separate the scattering image from fluorescence, an image splitter (W-VIEW GEMINI, Hamamatsu Photonics K.K., Japan) was place between the camera and the microscope port. The image splitter was equipped with a 510 nm dichroic mirror (FT 510,

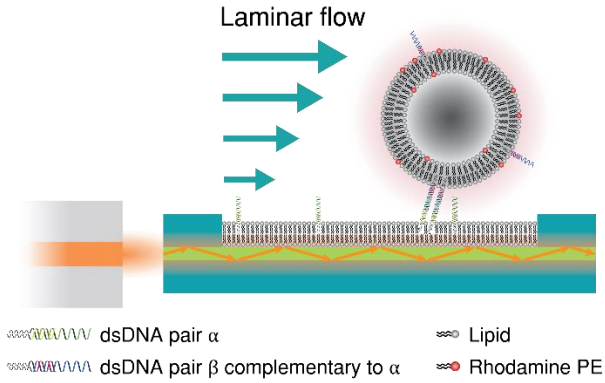

Figure 7.3. Schematic representation of a fluorescently labeled lipid vesicle tethered using complementary double strand DNA pairs, α and β to a POPC supported lipid bilayer formed on the waveguide core layer.

Carl Zeiss Microscopy, USA), a sharp band pass filter 488/4 nm (RET488/4x, Chroma Technology Corporation, USA) for scattering image and a 510 nm (BA510IF, Olympus Corporation, USA) long pass filter to maximize the fluorescence light collection. Using the image splitter, the scattering and fluorescence images were project next to each other on the on the camera sensor (Neo 5.5 sCMOS, Andor Technology Ltd, UK).

The aqueous solution was delivered to the waveguide through the microfluidic channels using a positive displacement piston pump, Cheminert® M6 (VICI AG International), in withdrawal mode, and Teflon tubing (OD 1/16" x ID 180 µm) with a total dead volume of 8 µL. After wetting the channels with MQ water and TE buffer (10 mM Tris, 1 mM EDTA, 125 mM NaCl, HCl pH 7.4), a supported lipid bilayer was formed on the waveguide core layer through the vesicle adsorption and rupture process using POPC vesicles mixed in a 100:1 ratio with tracer vesicles containing 1 mol% Rhod-PE fluorescent lipids (see **Paper V**) under a flow of 1 µL/min. The vesicle suspension was subsequently exchanged with buffer after which the bilayer was incubated with 50 nM solution of hybridized cholesterol-terminated double-strand DNA pairs (dsDNA) with 15 and 30-mers[b] (Eurogentec S.A., Belgium), at constant flow of 5 µL/min for at least 30 minutes. Self insertion of the double cholesterol anchor into the SLB ensures that the 15 free bases on the DNA construct are available for subsequent DNA hybridization reactions. In parallel with the DNA modification of the SLB, fluorescent lipid vesicles (POPC-Rhod PE [99:1 mol%], 67.3 ± 29.9 nm) were incubated in stagnant condition with a solution of a similar cholesterol-terminated dsDNA pair[c], with the difference that their 15 free bases

[b] α: 5'-TGGACATCAGAAATAAGGCACGACGGACCC-chol-3'
α': 5'-chol-CCCTCCGTCGTGCCT-3'
[c] β: 5'-TATTTCTGATGTCCAAGCCACGAGTTCCCC-chol-30
β': 5'-chol-CCCGAACTCGTGGCT-3'

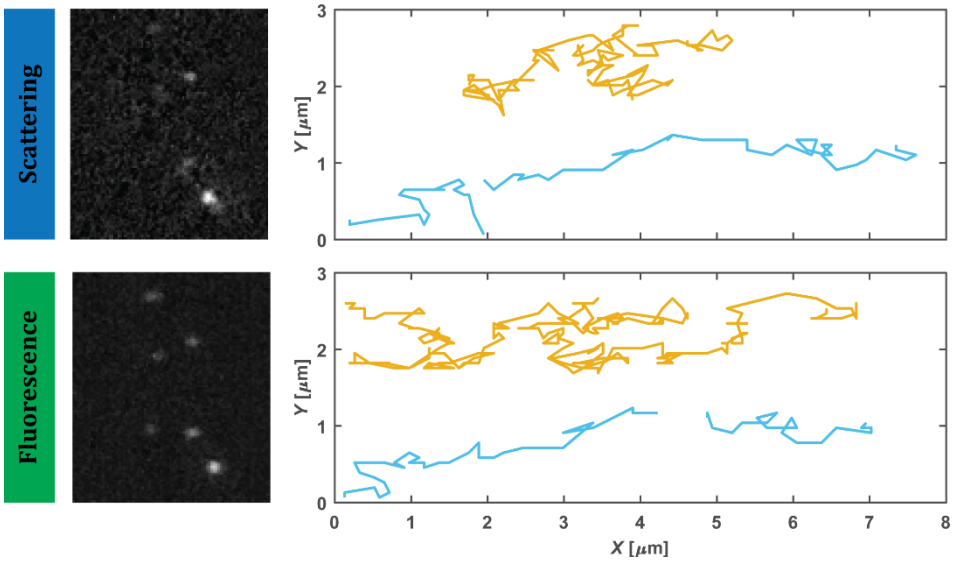

Figure 7.4. Flow nanometry snapshots and tracks of six POPC-Rhod PE (99:1 %M) vesicles (⌀67.3 ± 29.9 nm) bound to a POPC bilayer in scattering (top) and fluorescence (down) moving along X axis under 1 µL/min flow rate in a 1000 µm wide and 40 µm high microfluidic channel on the waveguide using 488 nm laser. Due to higher signal to noise in fluorescence for the specific vesicles used, the tracks are longer in fluorescence. To improve the clarity of the images, the background has been subtracted. The tracks should be corrected for the optical aberrations.

were complimentary to those on the DNA construct that was self-inserted into the SLB.[202] The incubation concentration of DNA was adjusted such that on average each vesicle is decorated with 10 dsDNA-pairs. After the incubation the tubes were rinsed with TE buffer, and the vesicle solution with hybridized dsNDA was pass over the bilayer, enabling DNA-hybridization based tethering of the vesicles to the SLB (Figure 7.3).

Figure 7.4 shows a snap shot of a few vesicles observed in scattering and fluorescence mode after background subtraction, along with the tracks of two of them at 200 ms exposure time at a liquid flow rate of 1 µL/min. Due to optical aberrations the tracks in scattering mode are somewhat stretched relative to those observed in fluorescence mode. To minimize the fluorescence bleaching, the illumination intensity was kept at a minimum, which has somewhat compromised the signal intensity and signal to noise value in the scattering images. As a results the tracks in fluorescence mode are longer and more accurate than in scattering. Since it will in principle be sufficient to determine the size form one of modes only, this is not a major concern; however, in future designs, this should be corrected for using calibration procedures applied on both imaging modes. Although the data quality is not yet sufficient to deduce the by tracking the vesicles detected in either fluorescence or scattering mode, these results are sufficient as a proof of principle for the possibility to correlate particle size not only with

fluorescence intensity,[38] but also scattering intensity. This will offer a unique opportunity to correlate the scattering intensity of each individual particle with their size as well as fluorescent signal, if properly labeled, allowing to extract information on the surface/volume density of the fluorescently labeled molecule on/in the BNPs and the density and refractive index of the BNPs on single particle level. The need of such information in the field of nanoparticle analytics was emphasized in **Paper V**, in which attempts were made to correlate the scattering intensity of EVs with the fluorescent intensity induced using a membrane-staining dye.

To reach this goal, it is clear form these results that there is a need of using a dye that is less prone to photo bleaching, and/or different lasers for the scattering and fluorescence measurement. It should then be possible to improve the data quality in both tracking modes and also improve the accuracy by which the emitted intensity from the particles can be quantified. It is also worthwhile to note that the polarizability and scattering cross-section of the relatively small (diameter 67 nm) lipid vesicles that were used in this initial test of the system is very small which why they are optically very faint when probed in scatter mode (see e.g. **Papers II** and **III**). Already similarly sized BNP such as extracellular vesicles and viruses, known to contain considerable amount of proteins and even genetic material, have higher polarizability and should thus be easier to track in scattering mode. With these improvements and applied on appropriate systems, it is my hope that the effort invested into this design can turn the device into a powerful multidimensional characterization platform.

8 Outlook

The main focus of this thesis has been the development of a competitive microscopy platform enabling for label-free analysis of biological nanoparticles. To reach that goal, I have spent many long hours in a white suit in a white lab, a.k.a. clearnroom, to develop and optimize the required nanofabrication processing to make a first working device. Then I moved to a dark lab, a.k.a microscopy lab, to characterize the device and demonstrate its capacity for various measurements. Now looking back at what I have accomplished and presented in this thesis, I would like to finish by reflecting on how the concepts presented here can be further developed.

8.1 Improving the image quality in scattering

Throughout this thesis work it has been the ambition to demonstrate the capabilities of the waveguide evanescent-field microscopy operating in combined fluorescence and label-free scattering modes to investigate biological nanoparticles. The waveguide device fabricated on silicon substrate (**Paper I**) is compatible with upright microscopes equipped with water immersion objectives and provide high-quality imaging with nominal numerical aperture of 1.1. One of the ambitions when modifying the fabrication protocol to be compatible also with glass substrates was not only to facilitate the microfluidic handling, but also to improve the efficiency of light collection. Due to the evanescent nature of the illumination, the volume fraction of a surface-bound scatterer that is positioned closest to the substrate, contributes more strongly to the scattering intensity. Further due to the higher permittivity of the core material relative to the

permittivity of both the medium and biological nanoparticles, the induced dipoles close the surface are expected to couple more strongly to the core layer relative to the medium. These phenomena should both contribute to a higher signal when the BNPs are imaged from the substrate side rather than the medium side, and thus motivated the efforts undertaken to fabricate the waveguide on glass substrates (**Paper III**).

Additionally, a waveguide device with a glass substrates opens up to the possibility to a wider selection of objectives and with numerical aperture (NA) values beyond 1.1, which is the NA limit for water immersion objectives provided by most vendors. The solid angle of 1.64π offered by high-end TIRF oil-immersion objectives (NA 1.49) offers about twice more efficient light collection compare to the 0.87π solid angle for NA 1.1 of the water immersion objectives. However, due to some optical aberration observed when using high NA objectives, we had to limit most of our experiments to oil immersion objectives with NA of about 0.9, which still required the black SU-8 layer on the back side of the device to attenuate the light coupled directly to the glass substrate form the optical fiber.

Some of these optical anomalies are intrinsic to the scattering process and the proximity of the imaged particles to the surface. Due to the coherent nature of scattering as described in **Chapter 2**, spatial features appear in the radiation pattern of a scatterer that experiences a plane-field illumination as the size of the scatterer increases, and as both the RGD approximation and the Mie theory predict, the lobes of forward scattering (in the direction of the incident light) is always stronger than the back scattering.[54] In the case of evanescent-field illumination[203] especially for a particle close to the substrate, these radiation patterns, as the field couples more strongly into the substrate relative to the medium, will tilt toward the substrate. This may induce an intrinsic distortion in the observed shape of the particle, as the collected scattering light from one side of the particles is more intense than the other side (Fig. 8.1). Due to the incoherent nature of fluorescence emission the radiation has a more symmetric pattern and therefore, such distortions are not pronounced (Fig. 8.1). Additionally, in the case of a symmetric waveguide design, as the one used in this work (Cyton-SOG-Cytop-Glass), at high scattering angles where light travels for longer distances within the core and cladding, the presence of multiple reflection between the SOG-Cytop and Cytop-Glass interface may result in more optical distortion, especially for large particles.

Although some of these distortions are intrinsic to the scattering process itself, an asymmetric waveguide design with the glass substrate as the lower cladding could possibly eliminate some sources of the distortion observed at higher numerical apertures. In contrast to the symmetric design, such an asymmetric waveguide would be compatible with TIRF microscopy, which makes a combined or simultaneous study using both techniques possible, and allows for a direct comparison of pros and cons of the two evanescent wave microscopy concepts.

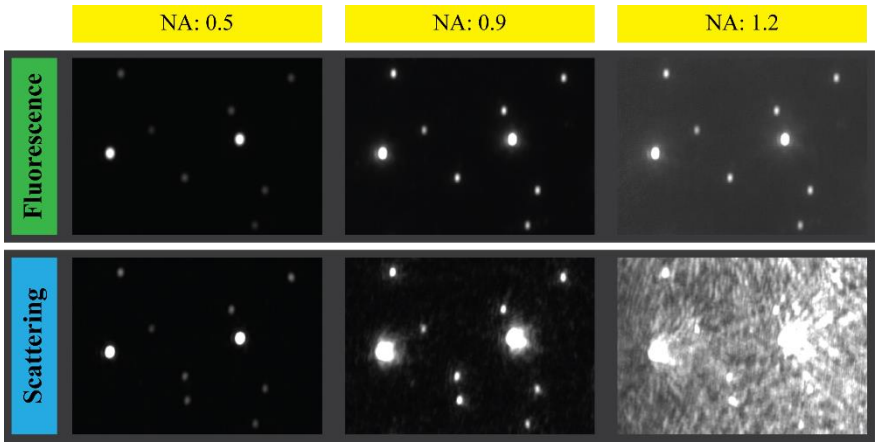

Figure 8.1. Scattering and fluorescence images of a few 100 nm and 200 nm fluorescent polystyrene beads (Fluoro-Max dyed red, ThermoFisher Scientific) captured at 3 different numerical apertures. The blue 488 nm laser propagate in the core from left to right. The intensity of both scattering and fluorescence increase with NA, however at high NA values the scattering image is greatly affected due to optical distortions. [The dynamic range of fluorescence images is 1/8th of that of the scattering.]

8.2 Scattering models and computer assisted simulations

In **Paper III** and **IV** we introduce two slightly different interpretations of Rayleigh-Gans-Debye (RGD) theory to represent the scattering intensities of biological nanoparticles. In both cases, the effect of the evanescent-field on the shape factor was neglected. In **Paper III**, we show a relatively good correlation between the experimental data and a simplified model, suggesting a rather small error relative to when the influence of the evanescent field in the shape factor is taken into account. However, it would be beneficial to compare the predictions of the simplified model with more accurate models, including not only the effect of the evanescent field on the scattering, but also the effect of the substrate and multiple reflection between the waveguide layers. Although such models would require computer simulations, they would allow not only to evaluate the accuracy of the predations and the limits of applicability of the proposed models, but also to optimize the waveguide design for different experimental conditions, to investigate the optical distortions and to evaluate the sensitivity limits of waveguide evanescent-field microscopy.

8.3 Flow nanometry

One of the most promising applications of the waveguide evanescent-field microscopy platform roots in its potential to characterize biological nanoparticles. As mention

earlier in the thesis, simultaneous determination of size as well as scattering and fluorescence intensity at the level of individual nanoparticles should provide the information needed to differentiate the contribution of different physical properties in the detected signals, including how these signals vary upon e.g. biomolecular binding or structural changes. By correlating the size of each analyzed NP with its scattering intensity, information about the effective refractive index should be possible to deduce. Further, by correlating the size and fluorescence intensity to each other, on can deduce information on the content of the label, and thus the compound that is labels. When such information is made available for each individual BNP, we foresee a unique opportunity to differentiate sub-populations of BNPs in complex biological samples.

As discussed in **Chapter 7**, I did not reach this goal within the frames of this thesis work, but the preliminary results suggest that we may not be far from realizing such dream. When the size of BNPs becomes smaller than ~100 nm, their scattering and fluorescence intensities drops with the ~6^{th} and 2^{nd} power of their radius, respectively, and at a certain size their signal-to-noise in scattering mode drops below that of fluorescence. Further, to obtain sufficient intensity in the scattering signal for smaller particles, the laser intensity must be increased. However, in our implementation, we so far used a single laser to both evaluating the scattering and the excite fluorophores. This imposed a compromise between high scattering intensity and rapid bleaching fluorophores. Using two different lasers and suitable dyes, one would be able to independently optimize the image quality in each imaging mode.

Another challenge faced in the 2D flow nanometry experiments was the efficiency by which the vesicles were tethered to the SLB. Further improvements of the tethering protocol and adapting alternative tethering techniques would not only contribute to a more successful implementation of the concept, but also broaden the applicability of the method beyond biological nanoparticles.

8.4 Modelling of supported lipid bilayer formation

In **Paper V**, we investigated how adsorption and rupture of vesicles on the glass surface leads to spontaneous formation of an SLB. The main finding of the study was the accelerated growth of later formed SLB patches, which differs from the conventional attenuated spreading speed of lipid monolayer/bilayer patches on hydrophobic/hydrophilic substrates, when emerging from a lipid source.[188,189,204] We made an attempt to represent the accelerated patch growth as free and rapid diffusivity of the lipids on the substrate. I am curious to explore if one can construct a model that also can take surface tensions between lipids, water and substrate into account. Including an energetically favorable wetting process,[188,189,204] such a model might be capable of representing the accelerated growth of the bilayer patches and explain the additional rare observations presented in the paper.

8.5 Nanofabrication

Nanofabrication has been one of the corner stones of this work. To fabricate a working waveguide lots of hours have been spent on the optimization of different processes and to find alternative solutions to address the challenges. Having the fabrication process of a working waveguide optimized, the fabrication is now very reproducible. However, when microfluidics are needed, the final step can still be very demanding. The fabrication process in such cases is concluded with sealing of the channels made in black SU-8 on top of the waveguide. Several bonding schemes have been evaluated, including, glass-SU8, SU8-SU8, and PDMS SU8. However, in this case, the challenge may not lay in the reproducibility of the bonding process but in the quality of the microscopy surface after bonding.

When working with a surface sensitive-microscopy technique like the one presented here, the entity under study should either be in contact or in the close vicinity of the microscopy surface. Different investigations require different surface qualities. Working with cell-membrane models like a supported lipid bilayer (SLB), the rate of success is greatly coupled to quality of the surface. The SLB quality, especially for the 2D flow nanometry experiments is very crucial. The bonding scheme evaluated so far, has had a high success rate with respect to bonding, but low chance of SLB formation, or vice versa, low bonding success rate but reproducibility in SLB formation. Finding a reliable bonding strategy that can grantee a good surface quality is crucial to the success of the device as multifaceted characterization platform.

Another useful added value to the waveguide device is hinted in **Paper IV**. The coupling efficiency of the optical fiber to the waveguide depends on the quality of the facet and the position of the fiber relative to the waveguide core. As a result, when evaluating the intensity data of different devices, it is beneficial to have a feedback on the coupling efficiency. In Paper IV we have used well defined polystyrene beads as both a reference for scattering of spherical particles and a normalization reference for the in-coupled light intensity in different experiments. Fabricating well defined-nanostructures on the waveguide core layer, could provide a built-in reference that can be used to access the coupling efficiency within an experiment or between different experiments.

8.6 Waveguides modified for other applications

Simulations in **Paper I** show how the penetration depth can be adjusted with the choice of the core material and its thickness. By reducing the core thickness and using a material with lower refractive index, the penetration depth can be increased above 1µm, which will allow for illumination of the entire volume of a shallow microfluidic channel made in the cladding of the waveguide. Such device can be used not only to determine the concentration NPs in bulk but could also, given a thin enough channel,

provide a platform for NTA-type measurements of NP size without having to deal with complications due to out of focus NPs. If fulfilled with sufficiently low background scattering, such a setup would allow for a similar correlation between the size, scattering and fluorescence intensity for individual nanoparticles as we try to achieve with flow nanometry (see **Chapter 7**), and perhaps even for sorting based on different features as they exit the channel. In this way, the concept may open up a new dimension in nanoparticle research that goes beyond pure characterization, as the function of different sub-populations of NPs can then be assessed in various biological assays and beyond.

Acknowledgments

I would like to express my gratitude to *Fredrik Höök* for his support during difficulties and his guidance, and supervision throughout the years. I have always admired his contagious enthusiasm for science, and the challenges he takes on.

Special thanks go to *Björn Agnarsson* for countless of reasons, including the responsibility he felt for my success, his supervision and support, long scientific discussions, patience, availability, advice and friendship.

I would like to acknowledge the help of my coauthors, specifically *Vladimir P. Zhdanov* for his patience in discussions and pedagogical approach to revising the manuscripts.

I would like to pay tribute to my comrades who graduated before me, *Déborah Rupert*, *Francesco Mazzota*, *Virginia Claudio*, Gülis Zengin, Hudson Pace and Olov Wahlsten, and those who will graduate after me, specially *Nadia Peerboom* and *Thomas Olsson*.

I would like to thank *Morteza Hassanzadeh* and *Ruggero Verre* for their friendship and support.

I would like to thank my great *officemates*, during these years, in particular the incumbents who were occasionally briefed about the latest status of my project in my long discussions with *Björn* in the office!

Special thanks go to my friends at *West Coast Jitterbugs* for the smiles and happy spirits! And good luck to those who are representing Göteborg in Savoy Cup!

I also would like to thank the current and former members of *biological physics*, *chemical physics* and *bionanophotonics* for sharing coffee breaks, cakes, chats, lunches, celebrations.

Finally, I need to specially thank *my wonderful parents* for their continuous motivation, and endless love and support, and my caring and loving siblings, *Zeinab*, *Hossein* and *Aboozar*.

Mokhtar Mapar, Göteborg, March 2018

Bibliography

[1] E. Hornung, *Akhenaten and the Religion of Light*. Cornell University Press, 1999.

[2] S. Nigosian, “Zoroastrian Teachings,” in *Zoroastrian Faith : Tradition and Modern Research*, MQUP, 1993, p. 167.

[3] M. KERKER, “Scattering by a Sphere,” in *The Scattering of Light and Other Electromagnetic Radiation*, vol. 16, Elsevier, 1969, pp. 27–96.

[4] M. Kaszuba, D. McKnight, M. T. Connah, F. K. McNeil-Watson, and U. Nobbmann, “Measuring sub nanometre sizes using dynamic light scattering,” *J. Nanoparticle Res.*, vol. 10, no. 5, pp. 823–829, May 2008.

[5] J. A. Gallego-Urrea, J. Tuoriniemi, and M. Hassellöv, “Applications of particle-tracking analysis to the determination of size distributions and concentrations of nanoparticles in environmental, biological and food samples,” *TrAC - Trends Anal. Chem.*, vol. 30, no. 3, pp. 473–483, 2011.

[6] G. Mie, “Beiträge zur Optik trüber Medien, speziell kolloidaler Metallösungen,” *Ann. Phys.*, vol. 330, no. 3, pp. 377–445, 1908.

[7] A. Einstein, “Über die von der molekularkinetischen Theorie der Wärme geforderte Bewegung von in ruhenden Flüssigkeiten suspendierten Teilchen,” *Ann. Phys.*, vol. 322, no. 8, pp. 549–560, 1905.

[8] W. J. Croft, *Under the Microscope: A Brief History of Microscopy*. World Scientific Publishing Co Pte Ltd, 2006.

[9] W. Moerner and L. Kador, “Optical detection and spectroscopy of single molecules in a solid,” *Phys. Rev. Lett.*, vol. 62, no. 21, pp. 2535–2538, 1989.

[10] S. W. Hell and J. Wichman, “Breaking the diffraction resolution limit by stimulated emission: stimulated-emission-depletion fluorescence microscopy,” *Opt. Lett.*, vol. 19, no. 11, pp. 780–782, 1994.

[11] E. Betzig *et al.*, “Imaging intracellular fluorescent proteins at nanometer resolution.,” *Science*, vol. 313, no. 5793, pp. 1642–5, Sep. 2006.

[12] D. Axelrod, T. P. Burghardt, and N. L. Thompson, “Total Internal Reflection Fluorescence,” *Annu. Rev. Biophys. Bioeng.*, vol. 13, no. 1, pp. 247–268, Jun. 1984.

[13] M. Tokunaga, K. Kitamura, K. Saito, A. H. Iwane, and T. Yanagida, “Single Molecule Imaging of Fluorophores and Enzymatic Reactions Achieved by Objective-Type Total Internal Reflection Fluorescence Microscopy,” *Biochem. Biophys. Res. Commun.*, vol. 235, no. 1, pp. 47–53, Jun. 1997.

[14] D. Axelrod, “Total Internal Reflection Fluorescence Microscopy in Cell Biology,” *Traffic*, vol. 2, no. 11, pp. 764–774, Nov. 2001.

[15] D. Axelrod, “Chapter 7 Total Internal Reflection Fluorescence Microscopy,” 2008, pp. 169–221.

[16] D. C. Prieve and N. a Frej, “Total internal reflection microscopy: a quantitative tool for the measurement of colloidal forces,” *Langmuir*, vol. 6, no. 9, pp. 396–403, 1990.

[17] P. von Olshausen and A. Rohrbach, “Coherent total internal reflection dark-field microscopy: label-free imaging beyond the diffraction limit.,” *Opt. Lett.*, vol. 38, no. 20, pp. 4066–9, 2013.

[18] M. Bally, A. Gunnarsson, L. Svensson, G. Larson, V. P. Zhdanov, and F. Höök, “Interaction of single viruslike particles with vesicles containing glycosphingolipids.,” *Phys. Rev. Lett.*, vol. 107, no. 18, p. 188103, Oct. 2011.

[19] A. Gunnarsson, P. Jönsson, R. Marie, J. O. Tegenfeldt, and F. Höök, “Single-molecule detection and mismatch discrimination of unlabeled DNA targets,” *Nano Lett.*, vol. 8, no. 1, pp. 183–188, 2008.

[20] S. R. Tabaei, M. Rabe, H. Zetterberg, V. P. Zhdanov, and F. Höök, “Single lipid vesicle assay for characterizing single-enzyme kinetics of phospholipid hydrolysis in a complex biological fluid,” *J. Am. Chem. Soc.*, vol. 135, no. 38, pp. 14151–14158, 2013.

[21] A. Leung, P. M. Shankar, and R. Mutharasan, “A review of fiber-optic biosensors,” *Sensors Actuators, B Chem.*, vol. 125, no. 2, pp. 688–703, 2007.

[22] X. Fan, I. M. White, S. I. Shopova, H. Zhu, J. D. Suter, and Y. Sun, “Sensitive optical biosensors for unlabeled targets: A review,” *Anal. Chim. Acta*, vol. 620, no. 1–2, pp. 8–26, Jul. 2008.

[23] U. Utzinger and R. R. Richards-Kortum, “Fiber optic probes for biomedical optical spectroscopy,” *J. Biomed. Opt.*, vol. 8, no. 1, p. 121, 2003.

[24] R. C. Jorgenson and S. S. Yee, “A fiber-optic chemical sensor based on surface plasmon resonance,” *Sensors Actuators B Chem.*, vol. 12, no. 3, pp. 213–220, 1993.

[25] S. W. James and R. P. Tatam, “Optical fibre long-period grating sensors: characteristics and application,” *Meas. …*, no. Ii, 2003.

[26] J. Escorihuela, M. Á. González-Martínez, J. L. López-Paz, R. Puchades, Á. Maquieira, and D. Gimenez-Romero, “Dual-Polarization Interferometry: A Novel Technique To Light up the Nanomolecular World,” *Chem. Rev.*, vol. 115, no. 1, pp. 265–294, Jan. 2015.

[27] A. Ganjoo *et al.*, “Planar chalcogenide glass waveguides for IR evanescent wave

sensors," *J. Non. Cryst. Solids*, vol. 352, no. 6–7, pp. 584–588, May 2006.

[28] J. Vörös *et al.*, "Optical grating coupler biosensors," *Biomaterials*, vol. 23, no. 17, pp. 3699–3710, Sep. 2002.

[29] A. Fernández Gavela, D. Grajales García, J. Ramirez, and L. Lechuga, "Last Advances in Silicon-Based Optical Biosensors," *Sensors*, vol. 16, no. 12, p. 285, Feb. 2016.

[30] M. C. Estevez, M. Alvarez, and L. M. Lechuga, "Integrated optical devices for lab-on-a-chip biosensing applications," *Laser Photon. Rev.*, vol. 6, no. 4, pp. 463–487, Jul. 2012.

[31] B. Agnarsson, S. Ingthorsson, T. Gudjonsson, and K. Leosson, "Evanescent-wave fluorescence microscopy using symmetric planar waveguides," *Opt. Express*, vol. 17, no. 7, p. 5075, 2009.

[32] D. J. Hill, C. W. Pinion, J. D. Christesen, and J. F. Cahoon, "Waveguide Scattering Microscopy for Dark-Field Imaging and Spectroscopy of Photonic Nanostructures," *ACS Photonics*, vol. 1, no. 8, pp. 725–731, Aug. 2014.

[33] A. Hassanzadeh, H. K. Ma, S. J. Dixon, and S. Mittler, "Visualization of the solubilization process of the plasma membrane of a living cell by waveguide evanescent field fluorescence microscopy," *J. Biomed. Opt.*, vol. 17, no. 7, p. 760251, Jul. 2012.

[34] H. M. Grandin, B. Städler, M. Textor, and J. Vörös, "Waveguide excitation fluorescence microscopy: A new tool for sensing and imaging the biointerface," *Biosens. Bioelectron.*, vol. 21, no. 8, pp. 1476–1482, 2006.

[35] Q. Nahar *et al.*, "Waveguide evanescent field scattering microscopy: bacterial biofilms and their sterilization response via UV irradiation," *J. Biophotonics*, vol. 7, no. 7, pp. 542–551, Jul. 2014.

[36] E. van der Pol, A. N. Boing, P. Harrison, A. Sturk, and R. Nieuwland, "Classification, Functions, and Clinical Relevance of Extracellular Vesicles," *Pharmacol. Rev.*, vol. 64, no. 3, pp. 676–705, 2012.

[37] E. VAN DER POL, A. G. HOEKSTRA, A. STURK, C. OTTO, T. G. VAN LEEUWEN, and R. NIEUWLAND, "Optical and non-optical methods for detection and characterization of microparticles and exosomes," *J. Thromb. Haemost.*, vol. 8, no. 12, pp. 2596–2607, Dec. 2010.

[38] S. Block, B. J. Fast, A. Lundgren, V. P. Zhdanov, and F. Höök, "Two-dimensional flow nanometry of biological nanoparticles for accurate determination of their size and emission intensity," *Nat. Commun.*, vol. 7, p. 12956, Sep. 2016.

[39] H. Zhang, S. Nie, C. M. Etson, R. M. Wang, and D. R. Walt, "Oil-sealed femtoliter fiber-optic arrays for single molecule analysis," *Lab Chip*, vol. 12, no. 12, p. 2229,

2012.

[40] H. Kogelnik, “Theory of Dielectric Waveguides,” 1975, pp. 13–81.

[41] R. G. Hunsperger, *Integrated Optics*. New York, NY: Springer New York, 2009.

[42] A. L. Mattheyses and D. Axelrod, “Direct measurement of the evanescent field profile produced by objective-based total internal reflection fluorescence,” *J. Biomed. Opt.*, vol. 11, no. 1, p. 14006, 2006.

[43] R. Fiolka, Y. Belyaev, H. Ewers, and A. Stemmer, “Even illumination in total internal reflection fluorescence microscopy using laser light,” *Microsc. Res. Tech.*, vol. 71, no. 1, pp. 45–50, Jan. 2008.

[44] C. GELL, M. BERNDT, J. ENDERLEIN, and S. DIEZ, “TIRF microscopy evanescent field calibration using tilted fluorescent microtubules,” *J. Microsc.*, vol. 234, no. 1, pp. 38–46, Apr. 2009.

[45] D. J. Griffiths and R. College, *Introduction to Electrodynamics*. Prentice Hall, 1999.

[46] R. B. Miles, W. R. Lempert, and J. N. Forkey, “Laser Rayleigh scattering,” *Meas. Sci. Technol.*, vol. 12, no. 5, pp. R33–R51, May 2001.

[47] C. F. Bohren and D. R. Huffman, “Angular Dependence of Scattering,” in *Absorption and Scattering of Light by Small Particles*, Weinheim, Germany: Wiley-VCH Verlag GmbH, 2007, pp. 381–428.

[48] V. A. Markel, “Introduction to the Maxwell Garnett approximation: tutorial,” *J. Opt. Soc. Am. A*, vol. 33, no. 7, p. 1244, Jul. 2016.

[49] J. D. Jackson, *Classical Electrodynamics*, 3rd ed. John Wiley & Sons, INC., 1998.

[50] R. Gans, “Strahlungsdiagramme ultramikroskopischer Teilchen,” *Ann. Phys.*, vol. 381, no. 1, pp. 29–38, 1925.

[51] H. C. Van De Hulst, *Light scattering by small particles*, vol. 1. 1981.

[52] M. KERKER, “Rayleigh–Debye Scattering,” in *The Scattering of Light and Other Electromagnetic Radiation*, Elsevier, 1969, pp. 414–486.

[53] G. Oster and D. P. Riley, “Scattering from isotropic colloidal and macro-molecular systems,” *Acta Crystallogr.*, vol. 5, no. 1, pp. 1–6, 1952.

[54] C. F. Bohren and D. R. Huffman, “Absorption and Scattering by a Sphere,” in *Absorption and Scattering of Light by Small Particles*, Wiley-VCH Verlag GmbH, 2007, pp. 82–129.

[55] A. L. Aden and M. Kerker, “Scattering of Electromagnetic Waves from 2 Concentric Spheres,” *J. Appl. Phys.*, vol. 22, no. 10, pp. 1242–1246, 1951.

[56] J. C. M. Garnett, “Colours in Metal Glasses, in Metallic Films, and in Metallic Solutions. II,” *Philos. Trans. R. Soc. A Math. Phys. Eng. Sci.*, vol. 205, no. 387–401, pp. 237–288, Jan. 1906.

[57] G. A. Niklasson, C. G. Granqvist, and O. Hunderi, “Effective medium models for the optical properties of inhomogeneous materials,” *Appl. Opt.*, vol. 20, no. 1, p. 26, Jan. 1981.

[58] U. K. Chettiar and N. Engheta, “Internal homogenization: effective permittivity of a coated sphere.,” *Opt. Express*, vol. 20, no. 21, pp. 22976–22986, 2012.

[59] R. Jansson and H. Arwin, “Selection of the physically correct solution in the n-media Bruggeman effective medium approximation,” *Opt. Commun.*, vol. 106, no. 4–6, pp. 133–138, Mar. 1994.

[60] S. Berthier and J. Lafait, “Effective medium theory: Mathematical determination of the physical solution for the dielectric constant,” *Opt. Commun.*, vol. 33, no. 3, pp. 303–306, 1980.

[61] R. Ruppin, “Evaluation of extended Maxwell-Garnett theories,” *Opt. Commun.*, vol. 182, no. 4, pp. 273–279, 2000.

[62] A. Lakhtakia and T. G. Mackay, “Size-dependent Bruggeman approach for dielectric–magnetic composite materials,” *AEU - Int. J. Electron. Commun.*, vol. 59, no. 6, pp. 348–351, Sep. 2005.

[63] W. R. Tinga, W. A. G. Voss, and D. F. Blossey, “Generalized approach to multiphase dielectric mixture theory,” *J. Appl. Phys.*, vol. 44, no. 9, pp. 3897–3902, Sep. 1973.

[64] J. R. Lakowicz, *Principles of Fluorescence Spectroscopy*. Boston, MA: Springer US, 2006.

[65] K. F. Tehrani, J. Xu, Y. Zhang, P. Shen, and P. Kner, “Adaptive optics stochastic optical reconstruction microscopy (AO-STORM) using a genetic algorithm,” *Opt. Express*, vol. 23, no. 10, p. 13677, 2015.

[66] J.-L. Viovy and L. Monnerie, “Fluorescence Anisotropy technique using Synchrotron Radiation as a powerful means for studying the orientation correlation functions of polymer chains,” in *Adv. Polym. Sci.*, vol. 67(Charact, 1985, pp. 99–122.

[67] B. R. Masters, “The Development of Fluorescence Microscopy,” in *Encyclopedia of Life Sciences*, Chichester, UK: John Wiley & Sons, Ltd, 2010, pp. 1–9.

[68] M. Renz, “Fluorescence microscopy-A historical and technical perspective,” *Cytom. Part A*, vol. 83, no. 9, pp. 767–779, Sep. 2013.

[69] M. Minsky, “Memoir on inventing the confocal scanning microscope,” *Scanning*, vol. 10, no. 4, pp. 128–138, 1988.

[70] P. Davidovits and M. D. Egger, “Scanning laser microscope.,” *Nature*, vol. 223, no. 5208, p. 831, Aug. 1969.

[71] D. Axelrod, “Cell-substrate contacts illuminated by total internal reflection fluorescence,” *J. Cell Biol.*, vol. 89, no. 1, pp. 141–145, Apr. 1981.

[72] S. W. Hell and J. Wichmann, “Breaking the diffraction resolution limit by stimulated emission: stimulated-emission-depletion fluorescence microscopy,” *Opt. Lett.*, vol. 19, no. 11, p. 780, Jun. 1994.

[73] T. A. Klar and S. W. Hell, “Subdiffraction resolution in far-field fluorescence microscopy,” *Opt. Lett.*, vol. 24, no. 14, p. 954, 1999.

[74] M. J. Rust, M. Bates, and X. Zhuang, “Sub-diffraction-limit imaging by stochastic optical reconstruction microscopy (STORM),” *Nat. Methods*, vol. 3, no. 10, pp. 793–796, Oct. 2006.

[75] T. Funatsu, Y. Harada, M. Tokunaga, K. Saito, and T. Yanagida, “Imaging of single fluorescent molecules and individual ATP turnovers by single myosin molecules in aqueous solution,” *Nature*, vol. 374, no. 6522, pp. 555–559, Apr. 1995.

[76] R. D. Vale, T. Funatsu, D. W. Pierce, L. Romberg, Y. Harada, and T. Yanagida, “Direct observation of single kinesin molecules moving along microtubules,” *Nature*, vol. 380, no. 6573. pp. 451–453, 1996.

[77] A. Yildiz, J. N. Forkey, S. A. McKinney, T. Ha, Y. E. Goldman, and P. R. Selvin, “Myosin V walks hand-over-hand: single fluorophore imaging with 1.5-nm localization.,” *Science*, vol. 300, no. 5628, pp. 2061–5, Jun. 2003.

[78] T. Ruckstuhl and S. Seeger, “Attoliter detection volumes by confocal total-internal-reflection fluorescence microscopy,” *Opt. Lett.*, vol. 29, no. 6, p. 569, Mar. 2004.

[79] T. J. Gould, J. R. Myers, and J. Bewersdorf, “Total internal reflection STED microscopy,” *Opt. Express*, vol. 19, no. 14, p. 13351, 2011.

[80] G. M. Cooper and R. E. Hausman, “The Cell: A Molecular Approach 2nd Edition,” *Sinauer Associates*. pp. 1–820, 2000.

[81] U. J. Meierhenrich, J. J. Filippi, C. Meinert, P. Vierling, and J. P. Dworkin, “On the origin of primitive cells: From nutrient intake to elongation of encapsulated nucleotides,” *Angew. Chemie - Int. Ed.*, vol. 49, no. 22, pp. 3738–3750, 2010.

[82] N. P. Kamat, S. Tobé, I. T. Hill, and J. W. Szostak, “Electrostatic Localization of RNA to Protocell Membranes by Cationic Hydrophobic Peptides,” *Angew. Chemie - Int. Ed.*, vol. 54, no. 40, pp. 11735–11739, 2015.

[83] S. J. Singer and G. L. Nicolson, “The Fluid Mosaic Model of the Structure of Cell Membranes,” *Science (80-.).*, vol. 175, no. 4023, pp. 720–731, Feb. 1972.

[84] J. P. Overington, B. Al-Lazikani, and A. L. Hopkins, “How many drug targets are there?,” *Nat. Rev. Drug Discov.*, vol. 5, no. 12, pp. 993–996, Dec. 2006.

[85] J. Liu, A. Stace-Naughton, X. Jiang, and C. J. Brinker, “Porous Nanoparticle Supported Lipid Bilayers (Protocells) as Delivery Vehicles,” *J. Am. Chem. Soc.*, vol. 131, no. 4, pp. 1354–1355, Feb. 2009.

[86] P. N. Durfee *et al.*, “Mesoporous Silica Nanoparticle-Supported Lipid Bilayers (Protocells) for Active Targeting and Delivery to Individual Leukemia Cells,” *ACS Nano*, vol. 10, no. 9, pp. 8325–8345, 2016.

[87] K. H. Biswas, J. A. Jackman, J. H. Park, J. T. Groves, and N.-J. Cho, “Interfacial Forces Dictate the Pathway of Phospholipid Vesicle Adsorption onto Silicon Dioxide Surfaces,” *Langmuir*, p. acs.langmuir.7b03799, 2018.

[88] I. Czolkos, A. Jesorka, and O. Orwar, “Molecular phospholipid films on solid supports,” *Soft Matter*, vol. 7, no. 10, p. 4562, 2011.

[89] I. Reviakine and A. Brisson, “Formation of Supported Phospholipid Bilayers from Unilamellar Vesicles Investigated by Atomic Force Microscopy,” *Langmuir*, vol. 16, no. 4, pp. 1806–1815, Feb. 2000.

[90] K. Dimitrievski and B. Kasemo, “Simulations of Lipid Vesicle Adsorption for Different Lipid Mixtures,” *Langmuir*, vol. 24, no. 8, pp. 4077–4091, Apr. 2008.

[91] P. Lenz, J. M. Johnson, Y.-H. M. Chan, and S. G. Boxer, “Tension-induced pore formation and leakage in adhering vesicles,” *Europhys. Lett.*, vol. 75, no. 4, pp. 659–665, Aug. 2006.

[92] S. Boxer, “Molecular transport and organization in supported lipid membranes,” *Curr. Opin. Chem. Biol.*, vol. 4, no. 6, pp. 704–709, Dec. 2000.

[93] R. P. Richter and A. R. Brisson, “Following the Formation of Supported Lipid Bilayers on Mica: A Study Combining AFM, QCM-D, and Ellipsometry,” *Biophys. J.*, vol. 88, no. 5, pp. 3422–3433, May 2005.

[94] A. Alessandrini and P. Facci, “Phase transitions in supported lipid bilayers studied by AFM,” *Soft Matter*, vol. 10, no. 37, pp. 7145–7164, 2014.

[95] M. Tkach and C. Théry, “Communication by Extracellular Vesicles: Where We Are and Where We Need to Go,” *Cell*, vol. 164, no. 6, pp. 1226–1232, Mar. 2016.

[96] G. van Meer, D. R. Voelker, and G. W. Feigenson, “Membrane lipids: where they are and how they behave,” *Nat. Rev. Mol. Cell Biol.*, vol. 9, no. 2, pp. 112–124, Feb. 2008.

[97] A. Ianoul, P. Burgos, Z. Lu, R. S. Taylor, and L. J. Johnston, “Phase Separation in Supported Phospholipid Bilayers Visualized by Near-Field Scanning Optical Microscopy in Aqueous Solution,” *Langmuir*, vol. 19, no. 22, pp. 9246–9254, Oct. 2003.

[98] L. J. Johnston, “Nanoscale imaging of domains in supported lipid membranes,” *Langmuir*, vol. 23, no. 11, pp. 5886–5895, 2007.

[99] A.-S. Cans *et al.*, “Artificial cells: Unique insights into exocytosis using liposomes and lipid nanotubes,” *Proc. Natl. Acad. Sci.*, vol. 100, no. 2, pp. 400–404, Jan. 2003.

[100] N. Stepanyants, G. D. M. Jeffries, O. Orwar, and A. Jesorka, “Radial Sizing of Lipid Nanotubes Using Membrane Displacement Analysis,” *Nano Lett.*, vol. 12, no. 3, pp. 1372–1378, Mar. 2012.

[101] O. Wahlsten, “Development of novel bioanalytical assays with single-molecule readout for biomarker detection and drug candidate characterization,” Chalmers University of Technology, 2017.

[102] S. F. Fenz and K. Sengupta, “Giant vesicles as cell models,” *Integr. Biol.*, vol. 4, no. 9, p. 982, 2012.

[103] B. C. Buddingh’ and J. C. M. van Hest, “Artificial Cells: Synthetic Compartments with Life-like Functionality and Adaptivity,” *Acc. Chem. Res.*, vol. 50, no. 4, pp. 769–777, Apr. 2017.

[104] Y. Elani, R. V. Law, and O. Ces, “Protein synthesis in artificial cells: using compartmentalisation for spatial organisation in vesicle bioreactors,” *Phys. Chem. Chem. Phys.*, vol. 17, no. 24, pp. 15534–15537, 2015.

[105] R. E. Lane, D. Korbie, W. Anderson, R. Vaidyanathan, and M. Trau, “Analysis of exosome purification methods using a model liposome system and tunable-resistive pulse sensing,” *Sci. Rep.*, vol. 5, no. 1, p. 7639, Jul. 2015.

[106] A. D. Bangham and R. W. Horne, “Negative staining of phospholipids and their structural modification by surface-active agents as observed in the electron microscope,” *J. Mol. Biol.*, vol. 8, no. 5, p. 660–IN10, Jan. 1964.

[107] C.-H. Huang, “Phosphatidylcholine vesicles. Formation and physical characteristics,” *Biochemistry*, vol. 8, no. 1, pp. 344–352, Jan. 1969.

[108] F. Olson, C. A. Hunt, F. C. Szoka, W. J. Vail, and D. Papahadjopoulos, “Preparation of liposomes of defined size distribution by extrusion through polycarbonate membranes,” *Biochim. Biophys. Acta - Biomembr.*, vol. 557, no. 1, pp. 9–23, Oct. 1979.

[109] E. Mayhew, R. Lazo, W. J. Vail, J. King, and A. M. Green, “Characterization of liposomes prepared using a microemulsifier,” *Biochim. Biophys. Acta - Biomembr.*, vol. 775, no. 2, pp. 169–174, Aug. 1984.

[110] B. Ruozi, G. Tosi, F. Forni, M. Fresta, and M. A. Vandelli, “Atomic force microscopy and photon correlation spectroscopy: Two techniques for rapid characterization of liposomes,” *Eur. J. Pharm. Sci.*, vol. 25, no. 1, pp. 81–89, May

2005.

[111] K. KODAMA, A. HASHIMOTO, Y. MORITA, K. TOMOCHIKA, and T. TSUCHIYA, “Preparation and Characterization of Everted Membrane Vesicles from Cells of Staphylococcus aureus.,” *Biol. Pharm. Bull.*, vol. 21, no. 1, pp. 5–9, 1998.

[112] S. Sarabipour, R. B. Chan, B. Zhou, G. Di Paolo, and K. Hristova, “Analytical characterization of plasma membrane-derived vesicles produced via osmotic and chemical vesiculation,” *Biochim. Biophys. Acta - Biomembr.*, vol. 1848, no. 7, pp. 1591–1598, Jul. 2015.

[113] V. P. Torchilin, “Recent advances with liposomes as pharmaceutical carriers,” *Nat. Rev. Drug Discov.*, vol. 4, no. 2, pp. 145–160, 2005.

[114] B. S. Pattni, V. V. Chupin, and V. P. Torchilin, “New Developments in Liposomal Drug Delivery,” *Chem. Rev.*, vol. 115, no. 19, pp. 10938–10966, 2015.

[115] L. K. Tamm and H. M. McConnell, “Supported phospholipid bilayers,” *Biophys. J.*, vol. 47, no. 1, pp. 105–113, Jan. 1985.

[116] E. Kalb, S. Frey, and L. K. Tamm, “Formation of supported planar bilayers by fusion of vesicles to supported phospholipid monolayers,” *Biochim. Biophys. Acta - Biomembr.*, vol. 1103, no. 2, pp. 307–316, Jan. 1992.

[117] A. O. Hohner, M. P. C. David, and J. O. Rädler, “Controlled solvent-exchange deposition of phospholipid membranes onto solid surfaces,” *Biointerphases*, vol. 5, no. 1, pp. 1–8, 2010.

[118] S. R. Tabaei, J.-H. Choi, G. Haw Zan, V. P. Zhdanov, and N.-J. Cho, “Solvent-Assisted Lipid Bilayer Formation on Silicon Dioxide and Gold,” *Langmuir*, vol. 30, no. 34, pp. 10363–10373, Sep. 2014.

[119] K. Sugihara, B. Jang, M. Schneider, J. Vörös, and T. Zambelli, “A universal method for planar lipid bilayer formation by freeze and thaw,” *Soft Matter*, vol. 8, no. 20, p. 5525, 2012.

[120] M. D. Mager and N. A. Melosh, “Lipid Bilayer Deposition and Patterning via Air Bubble Collapse,” *Langmuir*, vol. 23, no. 18, pp. 9369–9377, Aug. 2007.

[121] J. van Weerd, M. Karperien, and P. Jonkheijm, “Supported Lipid Bilayers for the Generation of Dynamic Cell-Material Interfaces,” *Adv. Healthc. Mater.*, vol. 4, no. 18, pp. 2743–2779, Dec. 2015.

[122] F. Roder *et al.*, “Reconstitution of Membrane Proteins into Polymer-Supported Membranes for Probing Diffusion and Interactions by Single Molecule Techniques,” *Anal. Chem.*, vol. 83, no. 17, pp. 6792–6799, Sep. 2011.

[123] A. Arslan Yildiz, U. H. Yildiz, B. Liedberg, and E. K. Sinner, “Biomimetic membrane platform: Fabrication, characterization and applications,” *Colloids Surfaces B Biointerfaces*, vol. 103, pp. 510–516, 2013.

[124] G. E. Rydell, A. B. Dahlin, F. Hook, and G. Larson, “QCM-D studies of human norovirus VLPs binding to glycosphingolipids in supported lipid bilayers reveal strain-specific characteristics,” *Glycobiology*, vol. 19, no. 11, pp. 1176–1184, Nov. 2009.

[125] F. Zhao *et al.*, “TiO2 nanoparticle interactions with supported lipid membranes – an example of removal of membrane patches,” *RSC Adv.*, vol. 6, no. 94, pp. 91102–91110, 2016.

[126] J. Knobloch, D. K. Suhendro, J. L. Zieleniecki, J. G. Shapter, and I. Köper, “Membrane–drug interactions studied using model membrane systems,” *Saudi J. Biol. Sci.*, vol. 22, no. 6, pp. 714–718, Nov. 2015.

[127] T. T. Nguyen and J. C. Conboy, “High-Throughput Screening of Drug–Lipid Membrane Interactions via Counter-Propagating Second Harmonic Generation Imaging,” *Anal. Chem.*, vol. 83, no. 15, pp. 5979–5988, Aug. 2011.

[128] I. Brigger, C. Dubernet, and P. Couvreur, “Nanoparticles in cancer therapy and diagnosis,” *Adv. Drug Deliv. Rev.*, vol. 54, no. 5, pp. 631–651, 2002.

[129] X. Gao, Y. Cui, R. M. Levenson, L. W. K. Chung, and S. Nie, “In vivo cancer targeting and imaging with semiconductor quantum dots.,” *Nat. Biotechnol.*, vol. 22, no. 8, pp. 969–976, 2004.

[130] L. J. Murray, M. Dincă, and J. R. Long, “Hydrogen storage in metal–organic frameworks,” *Chem. Soc. Rev.*, vol. 38, no. 5, p. 1294, 2009.

[131] G. M. Whitesides, “The origins and the future of microfluidics,” *Nature*, vol. 442, no. 7101, pp. 368–73, Jul. 2006.

[132] S. C. B. Mannsfeld *et al.*, “Highly sensitive flexible pressure sensors with microstructured rubber dielectric layers.,” *Nat. Mater.*, vol. 9, no. 10, pp. 859–64, 2010.

[133] N. V. Lavrik, M. J. Sepaniak, and P. G. Datskos, “Cantilever transducers as a platform for chemical and biological sensors,” *Rev. Sci. Instrum.*, vol. 75, no. 7, pp. 2229–2253, 2004.

[134] N. Barsan, D. Koziej, and U. Weimar, “Metal oxide-based gas sensor research: How to?,” *Sensors Actuators, B Chem.*, vol. 121, no. 1, pp. 18–35, 2007.

[135] N. Yazdi, F. Ayazi, and K. Najafi, “Micromachined inertial sensors,” *Proc. IEEE*, vol. 86, no. 8, pp. 1640–1658, 1998.

[136] K. A. Willets, R. Van Duyne, and R. P. Van Duyne, “Localized Surface Plasmon Resonance Spectroscopy and Sensing,” *Annu. Rev. Phys. Chem.*, vol. 58, no. 1, pp. 267–297, 2007.

[137] F. Meinardi *et al.*, “Highly efficient large-area colourless luminescent solar concentrators using heavy-metal-free colloidal quantum dots,” *Nat.*

Nanotechnol., no. August, 2015.

[138] S. Siahrostami *et al.*, "Enabling direct H2O2 production through rational electrocatalyst design.," *Nat. Mater.*, vol. 12, no. December, pp. 1137–43, 2013.

[139] J. N. Anker, W. P. Hall, O. Lyandres, N. C. Shah, J. Zhao, and R. P. Van Duyne, "Biosensing with plasmonic nanosensors.," *Nat. Mater.*, vol. 7, no. 6, pp. 442–453, 2008.

[140] M. P. Jonsson, A. B. Dahlin, L. Feuz, S. Petronis, and F. Höök, "Locally functionalized short-range ordered nanoplasmonic pores for bioanalytical sensing.," *Anal. Chem.*, vol. 82, no. 5, pp. 2087–94, Mar. 2010.

[141] B. Liedberg, C. Nylander, and I. Lunström, "Surface plasmon resonance for gas detection and biosensing," *Sensors and Actuators*, vol. 4, no. C, pp. 299–304, Jan. 1983.

[142] J. C. McDonald *et al.*, "Fabrication of microfluidic systems in poly(dimethylsiloxane).," *Electrophoresis*, vol. 21, no. 1, pp. 27–40, 2000.

[143] D. S. Kim, S. H. Lee, C. H. Ahn, J. Y. Lee, and T. H. Kwon, "Disposable integrated microfluidic biochip for blood typing by plastic microinjection moulding.," *Lab Chip*, vol. 6, no. 6, pp. 794–802, 2006.

[144] V. Srinivasan, V. K. Pamula, and R. B. Fair, "An integrated digital microfluidic lab-on-a-chip for clinical diagnostics on human physiological fluids.," *Lab Chip*, vol. 4, no. 4, pp. 310–5, Aug. 2004.

[145] P. Li, N. Lei, D. a. Sheadel, J. Xu, and W. Xue, "Integration of nanosensors into a sealed microchannel in a hybrid lab-on-a-chip device," *Sensors Actuators, B Chem.*, vol. 166–167, pp. 870–877, 2012.

[146] B. Agnarsson, J. Halldorsson, N. Arnfinnsdottir, S. Ingthorsson, T. Gudjonsson, and K. Leosson, "Fabrication of planar polymer waveguides for evanescent-wave sensing in aqueous environments," *Microelectron. Eng.*, vol. 87, no. 1, pp. 56–61, 2010.

[147] P. Degenaar *et al.*, "A Method for Micrometer Resolution Patterning of Primary Culture," vol. 376, pp. 367–376, 2001.

[148] Y. Grohens, J. Schultz, and R. E. Prud'homme, "PMMA conformational changes on g-alumina powder: influence of the polymer tacticity on the configuration of the adsorbed layer," *Int. J. Adhes. Adhes.*, vol. 17, no. 2, pp. 163–167, 1997.

[149] H. P. Pace, S. D. Sherrod, C. F. Monson, D. H. Russell, and P. S. Cremer, "Coupling supported lipid bilayer electrophoresis with matrix-assisted laser desorption/ionization-mass spectrometry imaging," *Anal. Chem.*, vol. 85, no. 12, pp. 6047–6052, 2013.

[150] H. Pace *et al.*, "Preserved Transmembrane Protein Mobility in Polymer-

Supported Lipid Bilayers Derived from Cell Membranes," *Anal. Chem.*, vol. 87, no. 18, pp. 9194–9203, Sep. 2015.

[151] W. O'Dell, "Template Matching." [Online]. Available: http://rsb.info.nih.gov/ij/plugins/template-matching.html.

[152] C. R. Taitt, G. P. Anderson, and F. S. Ligler, "Evanescent wave fluorescence biosensors: Advances of the last decade," *Biosens. Bioelectron.*, vol. 76, pp. 103–112, Feb. 2016.

[153] M. R. Foreman, J. D. Swaim, and F. Vollmer, "Whispering gallery mode sensors," *Adv. Opt. Photonics*, vol. 7, no. 2, p. 168, Jun. 2015.

[154] J. Homola, "Surface plasmon resonance sensors for detection of chemical and biological species," *Chem. Rev.*, vol. 108, no. 2, pp. 462–493, 2008.

[155] M. Rabe, S. R. Tabaei, H. Zetterberg, V. P. Zhdanov, and F. Höök, "Hydrolysis of a lipid membrane by single enzyme molecules: Accurate determination of kinetic parameters," *Angew. Chemie - Int. Ed.*, vol. 54, no. 3, pp. 1022–1026, 2015.

[156] D. Lee, K. P. Fong, M. R. King, L. F. Brass, and D. A. Hammer, "Differential dynamics of platelet contact and spreading," *Biophys. J.*, vol. 102, no. 3, pp. 472–482, 2012.

[157] B. György *et al.*, "Membrane vesicles, current state-of-the-art: emerging role of extracellular vesicles," *Cell. Mol. Life Sci.*, vol. 68, no. 16, pp. 2667–2688, Aug. 2011.

[158] A. Bobrie, M. Colombo, G. Raposo, and C. Théry, "Exosome Secretion: Molecular Mechanisms and Roles in Immune Responses," *Traffic*, vol. 12, no. 12, pp. 1659–1668, 2011.

[159] J. Rak and A. Guha, "Extracellular vesicles - vehicles that spread cancer genes," *BioEssays*, vol. 34, no. 6, pp. 489–497, 2012.

[160] S. A. Bellingham, B. B. Guo, B. M. Coleman, and A. F. Hill, "Exosomes: Vehicles for the Transfer of Toxic Proteins Associated with Neurodegenerative Diseases?," *Front. Physiol.*, vol. 3, no. May, pp. 1–12, 2012.

[161] H. Valadi, K. Ekström, A. Bossios, M. Sjöstrand, J. J. Lee, and J. O. Lötvall, "Exosome-mediated transfer of mRNAs and microRNAs is a novel mechanism of genetic exchange between cells," *Nat. Cell Biol.*, vol. 9, no. 6, pp. 654–659, Jun. 2007.

[162] N. Kosaka, H. Iguchi, Y. Yoshioka, F. Takeshita, Y. Matsuki, and T. Ochiya, "Secretory Mechanisms and Intercellular Transfer of MicroRNAs in Living Cells," *J. Biol. Chem.*, vol. 285, no. 23, pp. 17442–17452, Jun. 2010.

[163] S. Mathivanan, H. Ji, and R. J. Simpson, "Exosomes: Extracellular organelles

important in intercellular communication," *J. Proteomics*, vol. 73, no. 10, pp. 1907–1920, Sep. 2010.

[164] D. D. Taylor and C. Gercel-Taylor, "MicroRNA signatures of tumor-derived exosomes as diagnostic biomarkers of ovarian cancer," *Gynecol. Oncol.*, vol. 110, no. 1, pp. 13–21, Jul. 2008.

[165] G. Rabinowits, C. Gerçel-Taylor, J. M. Day, D. D. Taylor, and G. H. Kloecker, "Exosomal MicroRNA: A Diagnostic Marker for Lung Cancer," *Clin. Lung Cancer*, vol. 10, no. 1, pp. 42–46, Jan. 2009.

[166] N. Kosaka, H. Iguchi, and T. Ochiya, "Circulating microRNA in body fluid: A new potential biomarker for cancer diagnosis and prognosis," *Cancer Science*, vol. 101, no. 10. pp. 2087–2092, 07-Jul-2010.

[167] S. EL Andaloussi, I. Mäger, X. O. Breakefield, and M. J. A. Wood, "Extracellular vesicles: biology and emerging therapeutic opportunities.," *Nat. Rev. Drug Discov.*, vol. 12, no. 5, pp. 347–57, May 2013.

[168] Y. Lee, S. El Andaloussi, and M. J. A. Wood, "Exosomes and microvesicles: Extracellular vesicles for genetic information transfer and gene therapy," *Hum. Mol. Genet.*, vol. 21, no. R1, pp. 125–134, 2012.

[169] L. Zitvogel *et al.*, "Eradication of established murine tumors using a novel cell-free vaccine: dendritic cell derived exosomes," *Nat. Med.*, vol. 4, no. 5, pp. 594–600, May 1998.

[170] L. Alvarez-Erviti, Y. Seow, H. Yin, C. Betts, S. Lakhal, and M. J. A. Wood, "Delivery of siRNA to the mouse brain by systemic injection of targeted exosomes," *Nat. Biotechnol.*, vol. 29, no. 4, pp. 341–345, 2011.

[171] K. W. Witwer *et al.*, "Standardization of sample collection, isolation and analysis methods in extracellular vesicle research," *J. Extracell. Vesicles*, vol. 2, no. 1, p. 20360, Jan. 2013.

[172] H. Fischer, I. Polikarpov, and A. F. Craievich, "Average protein density is a molecular-weight-dependent function," *Protein Sci.*, vol. 13, no. 10, pp. 2825–2828, 2009.

[173] G. J. Hardy, R. Nayak, and S. Zauscher, "Model cell membranes: Techniques to form complex biomimetic supported lipid bilayers via vesicle fusion," *Curr. Opin. Colloid Interface Sci.*, vol. 18, no. 5, pp. 448–458, Oct. 2013.

[174] V. P. Zhdanov, C. A. Keller, K. Glasmästar, and B. Kasemo, "Simulation of adsorption kinetics of lipid vesicles," *J. Chem. Phys.*, vol. 112, no. 2, pp. 900–909, Jan. 2000.

[175] K. Dimitrievski, "Deformation of Adsorbed Lipid Vesicles as a Function of Vesicle Size," *Langmuir*, vol. 26, no. 5, pp. 3008–3011, Mar. 2010.

[176] H.-L. Wu, P. Chen, C. Chi, H.-K. Tsao, and Y.-J. Sheng, “Vesicle deposition on hydrophilic solid surfaces,” *Soft Matter*, vol. 9, no. 6, pp. 1908–1919, 2013.

[177] V. P. Zhdanov, “Mechanism of rupture of single adsorbed vesicles,” *Chem. Phys. Lett.*, vol. 641, pp. 20–22, Nov. 2015.

[178] M. Fuhrmans and M. Müller, “Mechanisms of Vesicle Spreading on Surfaces: Coarse-Grained Simulations,” *Langmuir*, vol. 29, no. 13, pp. 4335–4349, Apr. 2013.

[179] D. Stroumpoulis, A. Parra, and M. Tirrell, “A kinetic study of vesicle fusion on silicon dioxide surfaces by ellipsometry,” *AIChE J.*, vol. 52, no. 8, pp. 2931–2937, Aug. 2006.

[180] J. A. Jackman, Z. Zhao, V. P. Zhdanov, C. W. Frank, and N. Cho, “Vesicle Adhesion and Rupture on Silicon Oxide: Influence of Freeze–Thaw Pretreatment,” *Langmuir*, vol. 30, no. 8, pp. 2152–2160, Mar. 2014.

[181] J. Andrecka, K. M. Spillane, J. Ortega-Arroyo, and P. Kukura, “Direct Observation and Control of Supported Lipid Bilayer Formation with Interferometric Scattering Microscopy,” *ACS Nano*, vol. 7, no. 12, pp. 10662–10670, Dec. 2013.

[182] C. A. Keller, K. Glasmästar, V. P. Zhdanov, and B. Kasemo, “Formation of Supported Membranes from Vesicles,” *Phys. Rev. Lett.*, vol. 84, no. 23, pp. 5443–5446, Jun. 2000.

[183] J. M. Johnson, T. Ha, S. Chu, and S. G. Boxer, “Early Steps of Supported Bilayer Formation Probed by Single Vesicle Fluorescence Assays,” *Biophys. J.*, vol. 83, no. 6, pp. 3371–3379, Dec. 2002.

[184] T. Olsson, V. P. Zhdanov, and F. Höök, “Total internal reflection fluorescence microscopy for determination of size of individual immobilized vesicles: Theory and experiment,” *J. Appl. Phys.*, vol. 118, no. 6, p. 64702, 2015.

[185] M. Bally, K. Dimitrievski, G. Larson, V. P. Zhdanov, and F. Höök, “Interaction of virions with membrane glycolipids,” *Phys. Biol.*, vol. 9, no. 2, p. 26011, Apr. 2012.

[186] C. U. Chan and C. D. Ohl, “Total-internal-reflection-fluorescence microscopy for the study of nanobubble dynamics,” *Phys. Rev. Lett.*, vol. 109, no. 17, pp. 1–5, 2012.

[187] M. H. Hinrichs, A. Jalal, B. Brenner, E. Mandelkow, S. Kumar, and T. Scholz, “Tau Protein Diffuses along the Microtubule Lattice,” *J. Biol. Chem.*, vol. 287, no. 46, pp. 38559–38568, Nov. 2012.

[188] J. Raedler, H. Strey, and E. Sackmann, “Phenomenology and Kinetics of Lipid Bilayer Spreading on Hydrophilic Surfaces,” *Langmuir*, vol. 11, no. 11, pp. 4539–4548, Nov. 1995.

[189] J. Nissen, S. Gritsch, G. Wiegand, and J. O. Rädler, “Wetting of phospholipid

membranes on hydrophilic surfaces - Concepts towards self-healing membranes," *Eur. Phys. J. B*, vol. 10, no. 2, pp. 335–344, Aug. 1999.

[190] K. L. Weirich, J. N. Israelachvili, and D. K. Fygenson, "Bilayer Edges Catalyze Supported Lipid Bilayer Formation," *Biophys. J.*, vol. 98, no. 1, pp. 85–92, Jan. 2010.

[191] P. Plunkett, B. A. Camley, K. L. Weirich, J. Israelachvili, and P. J. Atzberger, "Simulation of edge facilitated adsorption and critical concentration induced rupture of vesicles at a surface," *Soft Matter*, vol. 9, no. 35, p. 8420, 2013.

[192] V. Filipe, A. Hawe, and W. Jiskoot, "Critical Evaluation of Nanoparticle Tracking Analysis (NTA) by NanoSight for the Measurement of Nanoparticles and Protein Aggregates," *Pharm. Res.*, vol. 27, no. 5, pp. 796–810, May 2010.

[193] R. C. Murdock, L. Braydich-Stolle, A. M. Schrand, J. J. Schlager, and S. M. Hussain, "Characterization of nanomaterial dispersion in solution prior to in vitro exposure using dynamic light scattering technique," *Toxicol. Sci.*, vol. 101, no. 2, pp. 239–253, 2008.

[194] C. Gardiner, Y. J. Ferreira, R. A. Dragovic, C. W. G. Redman, and I. L. Sargent, "Extracellular vesicle sizing and enumeration by nanoparticle tracking analysis," *J. Extracell. Vesicles*, vol. 2, no. 1, pp. 1–11, 2013.

[195] A. S. Lawrie, A. Albanyan, R. A. Cardigan, I. J. Mackie, and P. Harrison, "Microparticle sizing by dynamic light scattering in fresh-frozen plasma," *Vox Sang.*, vol. 96, no. 3, pp. 206–212, Apr. 2009.

[196] R. A. Dragovic *et al.*, "Sizing and phenotyping of cellular vesicles using Nanoparticle Tracking Analysis," *Nanomedicine Nanotechnology, Biol. Med.*, vol. 7, no. 6, pp. 780–788, Dec. 2011.

[197] G. E. Uhlenbeck and L. S. Ornstein, "On the theory of the Brownian motion," *Phys. Rev.*, vol. 36, no. 5, pp. 823–841, 1930.

[198] H. Qian, M. P. Sheetz, and E. L. Elson, "Single particle tracking. Analysis of diffusion and flow in two-dimensional systems," *Biophys. J.*, vol. 60, no. 4, pp. 910–921, Oct. 1991.

[199] X. Michalet, "Mean square displacement analysis of single-particle trajectories with localization error: Brownian motion in an isotropic medium," *Phys. Rev. E*, vol. 82, no. 4, p. 41914, Oct. 2010.

[200] E. A. Codling, M. J. Plank, and S. Benhamou, "Random walk models in biology," *J. R. Soc. Interface*, vol. 5, no. 25, pp. 813–834, Aug. 2008.

[201] R. von Mises and K. O. Friedrichs, *Fluid Dynamics*, vol. 5. New York, NY: Springer New York, 1971.

[202] I. Pfeiffer and F. Höök, "Bivalent Cholesterol-Based Coupling of Oligonucletides

to Lipid Membrane Assemblies," *J. Am. Chem. Soc.*, vol. 126, no. 33, pp. 10224–10225, Aug. 2004.

[203] A. Y. Bekshaev, K. Y. Bliokh, and F. Nori, "Mie scattering and optical forces from evanescent fields: A complex-angle approach," *Opt. Express*, vol. 21, no. 6, p. 7082, 2013.

[204] I. Czolkos, Y. Erkan, P. Dommersnes, A. Jesorka, and O. Orwar, "Controlled formation and mixing of two-dimensional fluids," *Nano Lett.*, vol. 7, no. 7, pp. 1980–1984, 2007.